

University of Montana

ScholarWorks at University of Montana

Graduate Student Theses, Dissertations, &
Professional Papers

Graduate School

2010

Structure and function of glutamate transporters

David Charles Holley

The University of Montana

Follow this and additional works at: <https://scholarworks.umt.edu/etd>

Let us know how access to this document benefits you.

Recommended Citation

Holley, David Charles, "Structure and function of glutamate transporters" (2010). *Graduate Student Theses, Dissertations, & Professional Papers*. 922.

<https://scholarworks.umt.edu/etd/922>

This Dissertation is brought to you for free and open access by the Graduate School at ScholarWorks at University of Montana. It has been accepted for inclusion in Graduate Student Theses, Dissertations, & Professional Papers by an authorized administrator of ScholarWorks at University of Montana. For more information, please contact scholarworks@mso.umt.edu.

STRUCTURE AND FUNCTION OF GLUTAMATE TRANSPORTERS

By

David Charles Holley

BS in Microbiology, University of Montana, Missoula, MT, 1999
BA in Economics, University of Virginia, Charlottesville, VA, 1990
BA in Philosophy, University of Virginia, Charlottesville, VA, 1990

Dissertation

presented in partial fulfillment of the requirements
for the degree of

Doctor of Philosophy
in Neuroscience

The University of Montana
Missoula, MT

Fall 2010

Approved by:

Perry Brown

Associate Provost for Graduate Education

Dr. Michael P. Kavanaugh, Chair
Department of Biomedical and Pharmaceutical Sciences

Dr. J.B. Alexander Ross
Department of Chemistry

Dr. Howard Beall
Department of Biomedical and Pharmaceutical Sciences

Dr. Nicholas Natale
Department of Biomedical and Pharmaceutical Sciences

Dr. Sean Esslinger
Department of Biomedical and Pharmaceutical Sciences

Holley, David, Ph.D., December 2010

Major
Neuroscience

A FUNCTIONAL DECONSTRUCTION OF PROTEINS USING COMPUTATIONAL ANALYSIS OF STRUCTURE

Chairperson: Michael P. Kavanaugh, Ph.D.

The work presented in this dissertation primarily entails determining specific structural and functional features involved with glutamate transport by the excitatory amino acid transporters (EAAT1-5). This research derives from a study of X-ray crystal structures of an homologous archaeal transporter. Broadly, using computational methods to probe EAAT homology models born from the archaeal structures, we describe novel Na⁺ and K⁺ coordination sites and present a model for sequential cation and substrate binding and unbinding during the transport cycle. A secondary focus of this dissertation was computational modeling of two other proteins: the HIV gp120 envelope protein (gp120) and NAD(P)H:Quinone Oxidoreductase 1 (NQO1). The study of gp120 involved a three-dimensional statistical analysis of amino acid substitutions that occur during early infection of clade A HIV, indicating that during early infection substitutions are non-random and co-locate in regions associated with receptor binding. The computational component of the study involving NQO1 used molecular docking of two lavendamycin analogues into the NQO1 active site. Here we showed that relative scores of docked poses of the analogues were consistent with *in vitro* evaluations. All the studies presented in this dissertation were collaborative efforts that linked *in silico* work with *in vitro* analysis.

ACKNOWLEDGMENTS

First, thanks must go to my friend and adviser, Mike Kavanaugh, who grounded my work through many thoughtful critiques and who was always a source of guidance, encouragement, patience, and most of all wit. I also owe a great debt of gratitude to the other members of my committee, Sean Esslinger, Sandy Ross, Howard Beall, and Nick Natale, who provided helpful direction and insights during my tenure here as a graduate student. There have been many other people who were instrumental to my intellectual development and continued sanity that I wish to thank- Greg Leary, Alicia Angell, Loretta Bolyard, Katie Hoffman, Weinan Sun, Dave Bonislowski, Fred Rhoderick, Sarj Patel, Todd Seib, Keith Parker, Ben Seaver, Shailesh Agarwal, John Gerdes, Leonid Kalachev, Jen Geist, Kate Stewart, and Mary Poss. Finally I would like to thank my friends and family- my partner James Randall, my parents Dave and Estelle, my sisters Karin and Brandon, and my friends Jonathan Proctor, Eric Paprocki, Bill Summers, Betsy Hands, Paul Hubbard, Wesley Parks, Larken, and Travis Elliot.

TABLE OF CONTENTS

Abstract	ii
Acknowledgments	iii
List of Figures	v
Chapter 1: Background and Significance	1
Chapter 2: Interactions of alkali cations with glutamate transporters	19
Chapter 3: A model for sequential binding in glutamate transporters	26
Chapter 4: Further computational work	47
Chapter 5: Discussion and future directions	82

LIST OF FIGURES AND TABLES

Chapter 1

Figure 1.	Alignment of Glt _{Ph} with homologous proteins.....	3
Figure 2.	Surface and ribbon representations of Glt _{Ph} structure (Boudker et al., 2007)	4
Figure 3.	Ribbon representation of aspartate-bound Glt _{Ph} with Na ⁺ depicted at TI ⁺ density sites 1 and 2	5
Figure 4.	Ribbon representations of wild type (WT) Glt _{Ph} subunit in the outward facing orientation and cross-linked Glt _{Ph} K55C/A364C in the inward facing state (Reyes et al., 2009).....	6
Figure 5.	Transport mechanism hemicycle of a single Glt _{Ph} subunit proposed by Reyes et al. (2009)	11
Figure 6.	Compilation of common cation coordination donor atoms and geometries found in Protein Data Bank structures.....	13

Chapter 2

Figure 1.	GltPh structure model based on Yernool et al. (2004)	20
Figure 2.	Identification of a novel sodium site in EAAT3	21
Figure 3.	Interactions of KC at site 4	23
Figure 4.	Potential binding pocket interactions facilitating coordinated substrate and Na ⁺ binding.....	23
Table 1.	Electrostatic calculations for NaC- and KC-binding sites in EAAT3	22
Table 2.	Substrate docking studies showing the effects of NaC on binding affinity in the EAAT3 homology models and the GltPh X-ray crystal structures	23

Chapter 3

Figure 1.	EAAT3 homology model showing thallium binding sites extracted from the Glt _{Ph} X-ray crystal structure and Na ⁺ coordination sites resolved from electrostatic mapping	28
Figure 2.	Sodium concentration dependence of tritiated glutamate uptake in EAAT3wt shows cooperation between sodium ions	29

Figure 3. Simultaneous fluorescence and current recording from oocytes injected with V417C EAAT3 or V417C-R447C EAAT3	30
Figure 4. Li ⁺ coordination is more susceptible than Na ⁺ to HP2 movement	32
Figure 5. Voltage-dependent interaction of lithium with hEAAT2	33
Figure 6. Electrostatic mapping of the HP2-loop closed form of EAAT3 predicts that the valence shell for K ⁺ coordination at site 5 includes glutamate (L-glu) at position 374	34
Figure 7. Recovery kinetics of EAAT3 in outside-out patches in response to paired glutamate pulses (10 mM) with K ⁺ or Na ⁺ in the (intracellular) pipette	35
Figure 8. Molecular dynamics simulations of Glt _{Ph} (5ns) show aspartate mobility when site 3 Na ⁺ is included	36
Figure 9. HP2 movement during a 10ns simulation in Glt _{Ph} is stabilized by Na ⁺ at site 2	36
Figure 10. Molecular dynamics simulations of the lipid embedded Glt _{Ph} system	37
Figure 11. Overview of the proposed transport model	40
Table 1. Electrostatic mapping of inward- and outward-facing models of EAAT3 and Glt _{Ph} structures	35

Chapter 4

Article A: Development of a homology model for clade A human immunodeficiency virus type 1 gp120 to localize temporal substitutions arising in recently infected women.

Figure a. NMR derived V3 loop extracted from the clade A gp120 homology model	48
Figure 1. Distribution of gp120 amino acid substitutions	50
Figure 2. Topological distribution of clade A-specific substitutions and temporal substitutions arising after infection with clade A HIV-1	52
Table 1. Summary of temporal substitutions	51

Article B: Novel lavendamycin analogues as antitumor agents: synthesis, in vitro cytotoxicity, structure–metabolism, and computational molecular modeling studies with NAD(P)H:quinone oxidoreductase 1.

Figure 1. Correlation of mean IC50 values obtained by the MTT and clonogenic assays	62
Figure 2. Superposition of docked poses	64
Figure 3. Depiction of docked poses for compound 37	65
Figure 4. Depiction of docked poses for compound 31	66
Table 1. Structures of lavendamycin analogues, reaction conditions and yields	58
Table 2. Structures of lavendamycin analogues.....	59
Table 3. Structures of quinoline-5,8-diones	59
Table 4. Electrochemical reduction potentialsa (DMSO) of lavendamycin analogues versus ferrocene	61
Table 5. Metabolism of lavendamycin analogues by recombinant human NQO1 monitored by spectrophotometric cytochrome c assay	62
Table 6. Cytotoxicity of lavendamycin analogues toward BE-WT (NQO1 deficient) and BE-NQ (NQO1-rich) human colon adenocarcinoma cell lines	63
Table 7. Number of poses of ligands 31 and 37 in each score group of CSCORE function	63

Article C: Unexpected behavior arising from the quaternary structure of glutamate transporters.

Figure b. Stick representations of inhibitors docked into an EAAT3 homology model	75
Figure 1. Surface representation of EAAT3 with docked pose of 2-FAA	79
Table a. Docking of 2-FAA, TBOA, and 3-Br-TBOA into an EAAT3 homology model show two possible binding orientations	74
Table 1. ChemScore evaluation of 2-FAA docked poses shows an increased affinity of EAAT3 homology model for the ‘upward’ orientation	79

Chapter 5

Figure 1. Cartoon depictions of outward-facing and inward-facing GltPh subunits colored by B-factors	83
--	----

Chapter 1: Background and significance

Introduction

Glutamate is the neurotransmitter responsible for conducting much of the excitatory signaling in the mammalian central nervous system (CNS) and is involved in synaptic plasticity necessary for learning and memory (Bortolotto et al., 1999; Curtis and Johnston 1974; Fonnum 1984). A crucial component of glutamatergic signaling in the CNS involves clearance of glutamate from the synaptic cleft by excitatory amino acid transporters (EAATs) (Diamond and Jahr, 1997). This dissertation focuses on discerning functionally critical aspects of EAAT structure through computational modeling.

Not surprisingly, much work toward understanding glutamate transport and EAAT structure and function had already been completed prior to work presented here. The following paragraphs will introduce the relevant research necessary to understand my own work, as well as provide a roadmap for the following chapters in my dissertation. First, I will introduce, in a general sense, functional characteristics of the EAATs in the CNS. Then I will consider the literature most relevant to my own research, and finally I will present an overview of my dissertation.

Glutamate uptake by the EAATs halts synaptic transmission and mediates toxicity stemming from overstimulation of surrounding neurons. Dysfunction of the EAATs has been well documented and is implicated in neurodegenerative diseases such as Alzheimer's disease and amyotrophic lateral sclerosis (ALS) and brain insults such as ischemia and epilepsy (Behrens et al., 2002; Carlsson and Carlsson, 1990; Choi, 1992; Ingram et al., 2000; Su et al., 2003; for reviews see Grewer and Rauen, 2005; Beart and O'Shea, 2007). There are five known mammalian subtypes of the transporters (EAAT1-5) each with distinct expression profiles within the CNS. Broadly, EAAT1 and EAAT2 are expressed on glial membranes throughout the CNS and are responsible for the majority of glutamate uptake, with EAAT1 predominant in the cerebellum and EAAT2 localizing primarily in the cortex and forebrain (Furuta et al., 1997). EAATs3-5 are expressed on neuronal membranes with EAAT3 widely expressed throughout the CNS, EAAT4 localizing to the cerebellum, and EAAT5 localizing to retinal neurons (Arriza et al., 1997; Fairman et al., 1995; Kania et al., 1995; for reviews see Bunch et al., 2009; Kanai and Hediger, 2004).

Transport by the EAATs is an active process, coupling the thermodynamically favorable transport of cations to power the transport of glutamate against its membrane concentration gradient. In the alternating access carrier model proposed by Yernool et al. (2004), two α -helical, hairpin loops (HP1 and HP2) gate the co-transport of glutamate with three Na^+ ions and one proton, and the subsequent antiport of one K^+ ion. This creates an electrogenic process transporting two net positive charges across the membrane. Additionally, the binding of Na^+ and glutamate activates an uncoupled chloride conductance that may help regulate neuronal excitatory response (Vandenberg et al., 2008; Veruki et al., 2006). Furthermore, in the absence of glutamate, Na^+ induces three separate currents: an uncoupled leak conductance carried by chloride ions (reviewed in chapter 2), a leak current carried by Na^+ , and a transient, capacitive current that can be blocked by addition of non-transportable inhibitors (Kanai et al. 1995; Melzer et al., 2003; Otis et al., 1997; Ryan et al., 2004; Wadiche and Kavanaugh, 1995; Wadiche and Kavanaugh, 1998).

The EAATs belong to the glutamate transporter family which contain structurally similar but functionally diverse transmembrane transport proteins including mammalian neutral amino acid transporters (ASCTs), bacterial C_4 -dicarboxylate transporters, and archaeal aspartate transporters (Slotboom et al., 1999a). In 2004 an X-ray crystal structure of an homologous archaeal aspartate transporter (Glt_{Ph}) was solved and to date five other Glt_{Ph} crystal structures have been published. These structures revealed details about the EAATs including their trimeric form in both inward and outward facing orientations, movement of HP2 which provides a mechanism for extracellular substrate access, and the positions of cation and substrate/inhibitor binding sites. Many aspects of glutamate transport, however, remain murky and without clarification of these details, the mechanism of transport cannot be accurately derived.

The Glt_{Ph} structure

The Glt_{Ph} transporters have approximately 35% sequence identity with the EAATs with a much higher conservation of residues implicated in substrate binding, ion binding, and anion conductance (figure 1a; Bendahan et al., 2000; Kavanaugh et al., 1997; Ryan et al., 2004), suggesting conservation of the basic architecture and transport mechanism. Therefore to better understand transport in the EAATs, it is helpful to be acquainted with structural details of the six homologous Glt_{Ph} X-ray crystal structures. The first structure, published in 2004, was of

lower resolution (approximately 3.2Å) and contained only an unresolved electron density near a region involved in substrate binding (figure 1c). Broadly, this structures contains three

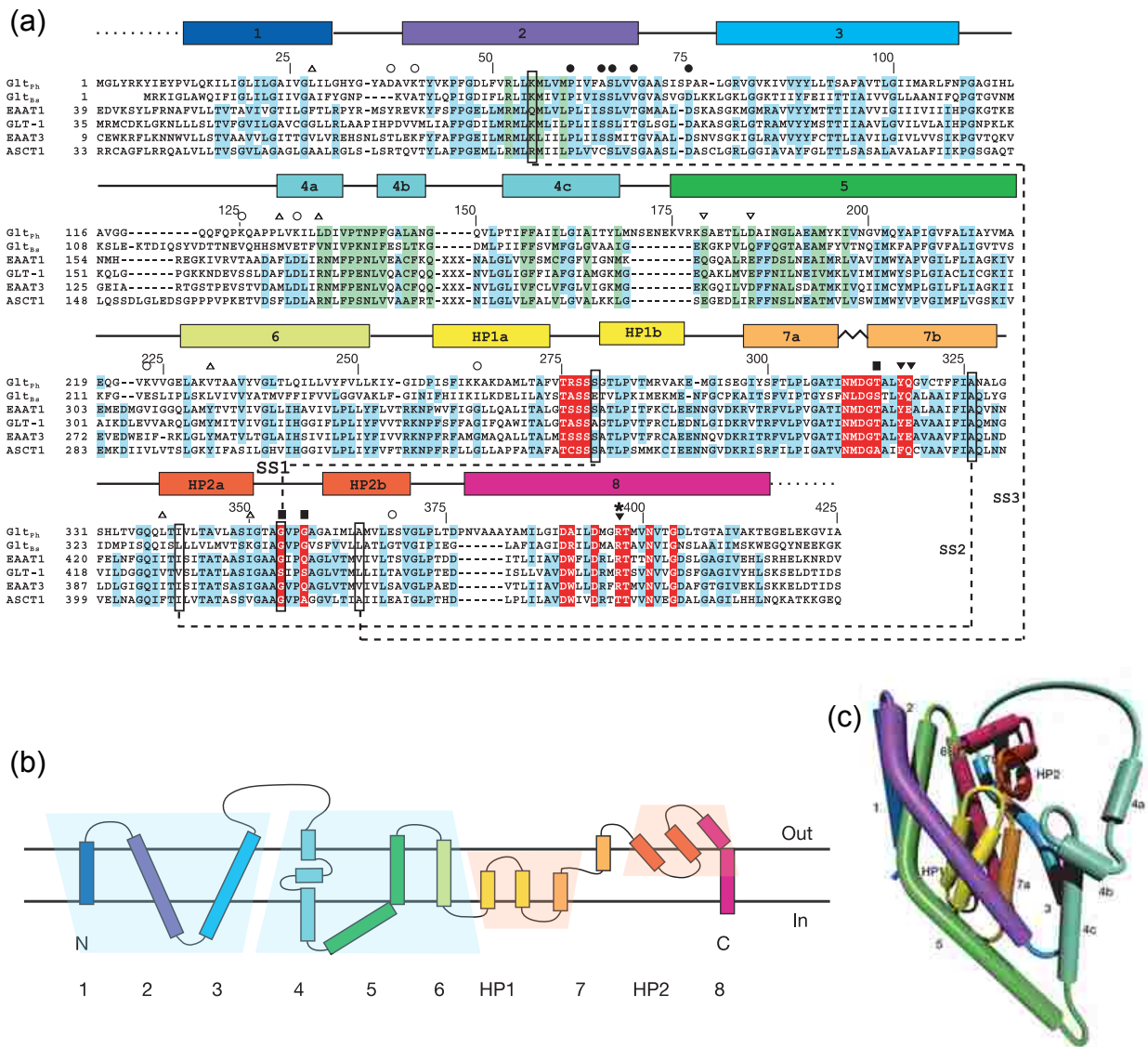


Figure 1. (a) Alignment of archaeal, EAAT, and SLC sequences show high sequence identity in regions in substrate binding and transport (red). Demarcations above the alignment identify residues involved in Na⁺ binding (squares), K⁺ binding (inverted triangles), chloride conductance (circles). Colored rectangles indicate transmembrane domains with different colors referencing the GltPh topology depicted in (b) (Yernool et al., 2004). (b) Schematic transmembrane topology of GltPh shows inverted structural repeats (trapezoids) (Yernool et al., 2004; Reyes et al., 2009). (c) Structure of single trimer subunit (Yernool et al., 2004).

identical subunits each with 8 transmembrane domains (TMs) and the two α -helical, re-entrant hairpin loops (HP1 and HP2) (figure 1b-c). The trimeric complex forms a bowl that penetrates approximately 30Å into the extracellular side of the cell membrane (figure 2a). Of the more recently published structures, two are bound with aspartate where HP2 is gated in a closed

conformation (more proximal to TM7 and TM8) and one is bound with 3-bromo-DL-*threo*- β -benzyloxyaspartate (3-br-TBOA) propping HP2 in a more open conformation that is proximal to the loop connecting transmembrane domains 3 and 4 (3-4 loop). Comparing the aspartate-bound and 3-br-TBOA-bound structures reveals conformational changes primarily in HP2 and the 3-4 loop, where HP2 moves as much as 10Ås and the 3-4 loop moves up to 3Ås (figure 2b).

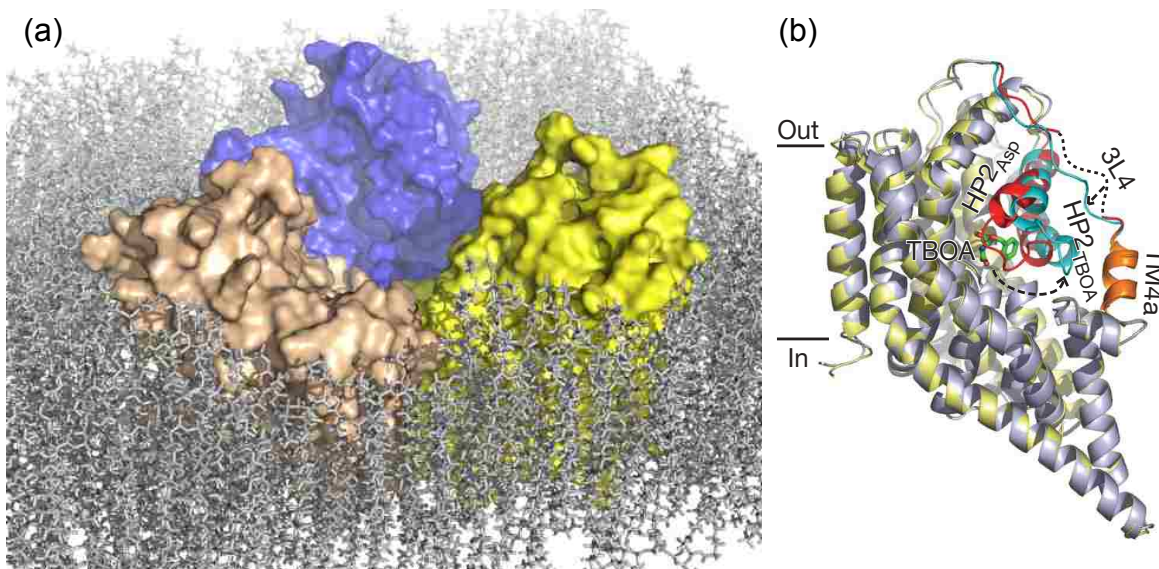


Figure 2. (a) Surface representation of Glt_{Ph} embedded in lipids (grey sticks) depicts the trimer bowl with subunits colored as wheat, blue, and yellow. (b) Overlay of the Glt_{Ph} HP2 open (cyan and gold ribbon) and occluded (red and grey ribbon) conformations. The overlay shows little divergence in the two structures except for the 3-4 loop (3L4) and HP2. HP2 conformational changes are highlighted in red (aspartate-bound, occluded conformation) and cyan (TBOA-bound, open conformation). Bound TBOA is depicted in stick representation (Boudker et al., 2007).

One of the outward-facing, aspartate-bound structures was resolved with two thallium ions that are posited by the authors as surrogates for Na⁺ ions (figure 3). These two bound ions reveal a partial substrate binding order; site 1 binds deep within the overall binding pocket before the amino acid substrate is bound, and site 2, which is available only when HP2 is in the closed conformation, binds after substrate is bound. Both of the resolved cations are coordinated in part by the highly conserved NMDG sub-domain that disrupts the TM7 α -helix (figure 3). Specifically, the thallium-laden, aspartate-bound crystal structure shows the distal oxygen of the conserved asparagine in the NMDG β -bridge sub-domain forming part of the coordination shell for thallium at site 1. This is somewhat consistent with functional studies that show that both the asparagine and aspartate of **NMDG** interact with Na⁺ (Borre and Kanner, 2001; Zerbiv et al., 1998; Tao et al., 2006). Likewise, the dipole moment formed by the

disruption of the TM7 α -helix stabilizes cation coordination at site 2 (figure 3). The influence of the NMDG motif extends also to amino acid binding by allowing tertiary constraints critical for the formation of the amino acid binding site and orientation of HP2 (Yernool et al., 2004; Boudker et al., 2007).

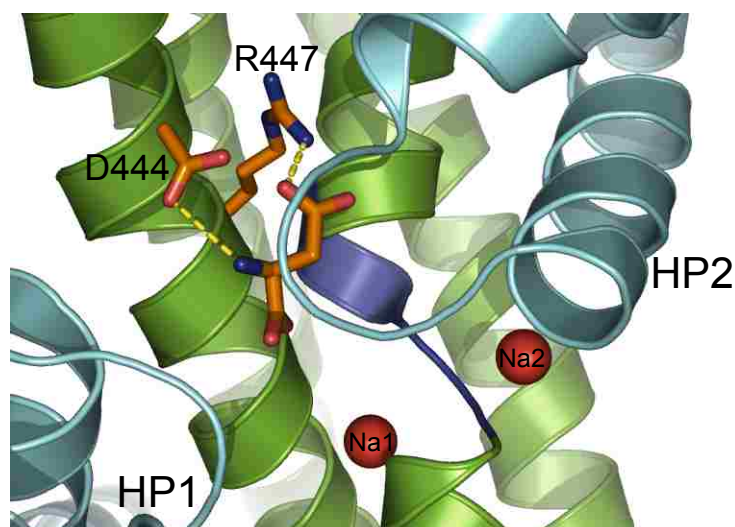


Figure 3. Ribbon representation of aspartate-bound Glt_{Ph} with Na⁺ depicted at TI⁺ density sites 1 and 2. Stick representations of bound aspartate and residues responsible for acidic amino acid recognition are represented as sticks and are labeled with the EAAT3 sequence. The blue colored portion of the ribbon indicates the conserved NMDG β -bridge region implicated in Na⁺ and amino acid substrate binding.

Very recently Reyes et al. (2009) capitalized on EAAT1 cysteine cross-linking data published in 2004 by Ryan et al. who showed that residues in TM2 are proximal to residues in HP2. The residues in question are 25Å apart in outward facing Glt_{Ph} structures yet are cross-link competent in the presence of substrate, indicating that the transporter samples conformations very different from the outward facing conformations. Reyes et al. (2009) cross-linked the analogous residues in Glt_{Ph} (cysteine point mutations K55C/A364C) to stabilize the alternately-oriented transporter for crystallization. The resulting structure revealed that trimer subunits contain two structurally rigid domains, one of which stays anchored in the membrane (the trimerization domain) while the other moves approximately 18Å across the membrane (the transport domain) (figure 4a,b). The domains are hinged at the TM2-3 and TM5-6 loops and during transport cause unwinding of α -helices in TM2, TM3, and TM5 and extension of the TM6 α -helix. The rigidity of the two domains is impressive showing a 0.6Å root mean square distance (r.m.s.d.) when the outward facing domains are superimposed with the inward facing structure. The authors also show that the substrate free form of Glt_{Ph} rapidly samples the

cross-link competent state, suggesting that cation and substrate binding/release, and not actual transport, are the thermodynamically linked steps. The resolution of the structure is somewhat low at 3.5–3.9 Ås, however the authors were able to resolve electron densities for bound aspartate and two sodium ions that coincided extremely well with the outward facing thallium and aspartate bound structure. This is less surprising, of course, when considering the outward facing structures were used as scaffolds for modeling the inward facing diffraction patterns (i.e. through molecular replacement techniques).

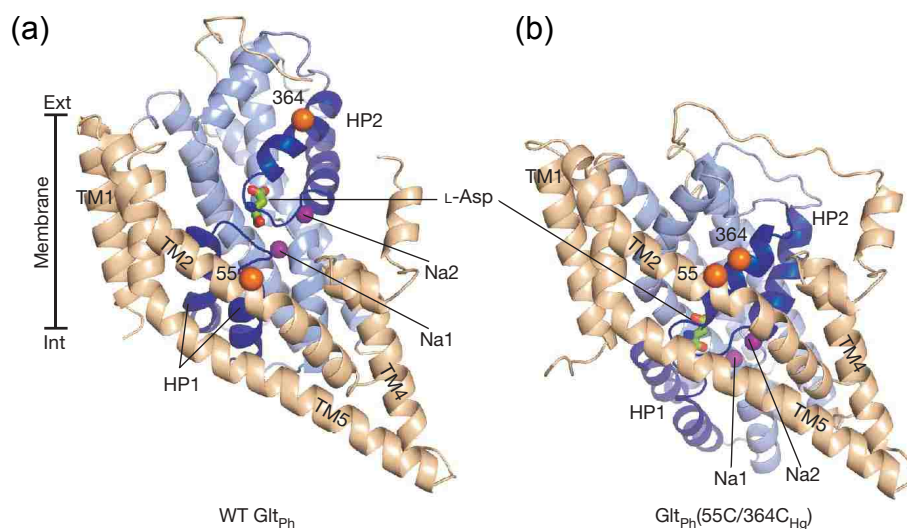


Figure 4. Ribbon representations of wild type (WT) Glt_{Ph} subunit in the outward facing orientation (a) and cross-linked Glt_{Ph} K55C/A364C in the inward facing state (b). The trimerization domain is colored coded wheat and the transport domain is color coded in blues with bound aspartate (sticks, labeled L-Asp) and Na⁺ sites (purple spheres) (Reyes et al., 2009).

An important but often overlooked segment of the Glt_{Ph} structure is the 3-4 loop. This loop bows out towards the center of the trimer bowl and acts as both a bracket for HP2 movement and an amphipathic region of interaction with the adjacent subunit. The higher resolution Glt_{Ph} structures excluded a portion of the 3-4 loop suggesting a degree of unstructured lability in both the 3-br-TBOA-bound and aspartate-bound models. TM4 in the Glt_{Ph} structures also contain a 40-50 amino acid deletion relative to EAAT sequences which is predicted to contain an ordered α -helix, β -sheet structure. This deletion poses serious constraints on the reliability of homology models for molecular dynamics simulations.

Another interesting aspect of the Glt_{Ph} structure is that it appears to be an assembly of two different inverted structural repeats (figure 1b; Crisman et al., 2009; Yernool et al., 2004;

Reyes et al., 2009). HP1 and the N-terminal half of TM7 can be inverted and superimposed onto HP2-loop and the N-terminal portion of TM8 with an r.m.s.d. of 2.5Ås while TM4-6 can be superimposed on TM1-3 with an r.m.s.d. of 6Ås in the outward facing orientation and 4.3Ås in the inward facing orientation. These structural repeats help to define the interface between the cytoplasmic and the extracellular portions of the trimerization domain (Reyes et al., 2009). More fundamentally and assuming the structural repeats are linked to gene duplication events, the repeats also indicate that structural conservation, if not sequence conservation, is maintained at a sub-domain level.

Similarities between EAATs and Glt_{Ph}

The first two results chapters of this dissertation rely on the homology between the EAATs and Glt_{Ph}. It is therefore important to consider similarities and differences between these transporters. First, on a broad scale, Glt_{Ph} is an archaeal transporter found in *Pyrococcus horikoshii* and is highly selective for aspartate over other amino acids (Boudker et al., 2007; Ryan et al., 2009). Similar to the EAATs, Glt_{Ph} transport is coupled to three Na⁺ ions but, unlike the EAATs, is not coupled to proton transport or K⁺ countertransport (Ryan et al., 2009; Groeneveld and Slotboom, 2010). The sequence identity between Glt_{Ph} and the EAATs is approximately 35% with higher identity in regions associated with substrate binding and anion conductance (Yernool et al., 2004; figure 1a). Discussed above but important to reiterate here is the deletion in TM4 in Glt_{Ph}. Again, this deletion restricts reliable homology modeling to regions with high sequence conservation and due to the potential for amplified error, excludes all but extremely short molecular dynamics simulations of orthologous EAAT systems.

With this in mind, the overall reliability of homology models based on seemingly diverse structures is questionable. However, the high sequence identity between the transporters in areas responsible for substrate binding and transport indicates regions of very high structural compatibility. Specifically, conservation of residues responsible for acidic amino acid binding in EAAT transmembrane 8 is conserved in Glt_{Ph} with two residues known to confer substrate specificity (R447 and D444 in EAAT3) directly interacting with bound aspartate in the Glt_{Ph} crystal structure in a manner consistent with the literature (figure 3; Bendahan et al., 2000; Boudker et al., 2007; Teichman and Kanner, 2007). Likewise, the NMDG sub-domain in TM7 is highly conserved throughout the glutamate transporter family and its involvement in Na⁺ and

substrate binding in the EAATs is supported by the Glt_{Ph} structures (Borre and Kanner, 2001; Boudker et al., 2007; Tao et al., 2006; Zerbiv et al., 1998). Other structural motifs such as the Glt_{Ph} HP1 and HP2 are also consistent with cross-linking and mutation data in the EAATs (Slotboom et al., 1999; Grunewald et al., 1998).

Architectural conservation without sequence conservation is also a relatively established paradigm. For example, the sequence identity for the lactose permease and the glycerol-3-phosphate antiporter (both are proteins in *Escherichia coli*) is considered random at approximately 15%. However, published X-ray crystal structures reveal the proteins as structurally almost identical with an r.m.s.d. of approximately 2.8Ås (Abramson et al., 2004). Although this is merely one example it shows that structural conservation can be maintained without sequence conservation. Thus, the consistency between structural facets of the EAATs revealed through electrophysical, mutation and cross-linking studies and the Glt_{Ph} X-ray crystal structures is well described (Yernool et al., 2004; Boudker et al., 2007; Reyes et al., 2010) and would indicate sufficient evidence for EAAT modeling based on published Glt_{Ph} sequence alignments (Yernool et al., 2004).

The substrate binding site

The Glt_{Ph} crystal structures provide insights into substrate binding interactions with much of the functional implications for these interactions derived from kinetic and mutation studies. Below I discuss key structural and functional features involving substrate recognition and translocation that will help delineate the substrate binding region.

The binding site incorporates several structural sub-domains. First, as previously touched-on, the structure of the substrate binding site is formed by the highly conserved β -bridge sequence that disrupts the TM7 α -helix (figure 3). This sequence has been implicated in Na⁺, K⁺, and glutamate binding and translocation (Yernool et al., 2004; Rosental et al., 2006; Tao et al., 2006) and performs at least two very distinct functions: 1. The β -bridge forms a platform for substrate binding possibly allowing sufficient room in the HP2 occluded conformation for glutamate binding and K⁺ countertransport, and 2. the β -bridge structure introduces into TM7 an α -helix dipole critical for site 2 Na⁺ coordination (Yernool et al., 2004; Reyes et al., 2009).

The second structural domain defining the substrate binding site is the amphipathic α -helix of TM8 which holds residues responsible for substrate identification. Specifically, Bendahan et al. (2000) demonstrated that an arginine residue (R447 in EAAT3) conserved throughout all glutamate transporters but neutralized in neutral amino acid transporters is responsible for acidic amino acid recognition. This residue, when mutated to cysteine, abolishes glutamate transport and instead allows transport of alanine and serine (Bendahan et al., 2000). Likewise Teichman and Kanner (2007) demonstrated that an aspartate residue (D444 in EAAT3) conserved in all homologous amino acid transporters (EAATs, ASCTs, and archaeal aspartate transporters) but neutralized in bacterial C₄-dicarboxylate transporters is responsible for recognition of amino acid substrates. Together these residues enforce EAAT substrate specificity (figure 3).

The third defining motif of the substrate binding arena are the hairpin loops (HP1 and HP2) that are the proposed gatekeepers to the intracellular and extracellular fluids (Boudker et al., 2007). As discussed above, the exact mechanism for HP1 gated access has yet to be determined though constraints on HP1 inhibit transport (Shlaifer and Kanner, 2007). The mechanism for HP2 gated access is much better understood. Boudker et al. (2007) demonstrated HP2 movement with two Glt_{Ph} crystal structures revealing HP2 in the occluded, closed conformation and HP2 swung open to accommodate inhibitor binding (figure 2b). Molecular dynamics simulations of Glt_{Ph} systems also show rapid movement of HP2 (Huang and Tajkhorshid, 2008).

Inhibitor specificity between EAAT subtypes is a more subtle affair. Specifically, EAAT2 has a different affinity profile for competitive inhibitors than other EAATs, though the EAAT2 amino acid sequence within the substrate binding arena is almost identical to EAAT1 and EAAT3 (figure 1a. Red highlighted regions are implicated in binding and transport. GLT-1 is alternative nomenclature for EAAT2). The exception to this sequence conservation lies within the hairpin region of HP2 which includes serine substitutions in EAAT2. Point mutations in EAAT1 substituting EAAT2 serine residues for the EAAT1 sequence show increased affinity for EAAT2 subtype specific inhibitors (Zhang and Kanner, 1999; Huang et al., 2009). Huang et al. (2009) propose that the specificity that these EAAT2 substitutions incur are indirect and reflect subtle divergence in the HP2 occluded conformation. Molecular dynamics simulations reported

here in chapter 3 support Huang's proposition showing small deviations in HP2 positioning disproportionately affect Li^+ coordination over Na^+ .

Mechanism of transport

Yernool et al. (2004) on analysis of their freshly minted X-ray structure proposed an alternating access model for transport with extracellular access gated by HP2 and intracellular access gated by HP1. Boudker et al. (2007) refined this model with crystal structures resolving the two Ti^+ binding sites and showing HP2 conformational changes. Specifically, the aspartate-bound Glt_{Ph} structure revealed Ti^+ densities at sites 1 and 2 while the TBOA-bound Glt_{Ph} structure includes only one Ti^+ density (site 1) and shows HP2 swung open to accommodate the bulky benzene ring of 3-br-TBOA. With these structures as a guide, Boudker et al. contend that substrate binds the transporter when HP2 is in the open conformation and after Na^+ is bound at site 1. This is followed by HP2 closure, binding of Na^+ at site 2, and subsequent release through a less well characterized HP1 movement. Kinetic studies show that K^+ countertransport resets the transporter for the next round of substrate binding and translocation (Bergles et al., 2002; Grewer et al., 2000; Otis et al., 1997; Wadiche and Kavanaugh, 1998). Molecular dynamics simulations (Huang and Tajkhorshid, 2008; Shrivastava et al., 2008) and studies involving fluorescently labeled HP2 (see chapter 3) support that HP2 gates access during substrate binding. HP1 movement in the outward facing structure however is tightly constrained by TM2 rendering the loop immobile. The recently solved inward facing structure resolves this issue through the conformational change of the transport domain from outward to inward facing orientations which releases HP1 from TM2 constraints (Reyes et al., 2009). This appears to validate the global conformational mechanism of the gated, alternating access model proposed by Yernool et al. in 2004 (figure 5). Chapters 2 and 3 of this dissertation expand on Yernool's model with evidence for a third Na^+ site as well as two K^+ sites that could form part of the K^+ countertransport pathway. We also show that sodium induces the HP2 open conformation possibly through uncharacterized Na^+ sites.

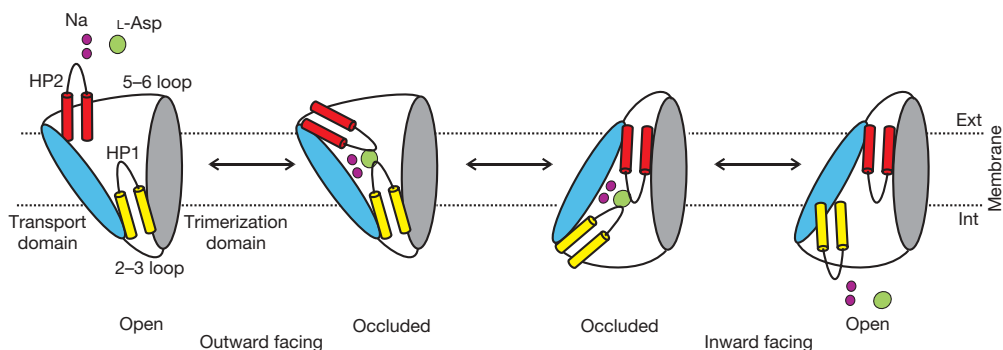


Figure 5. Transport mechanism hemicycle of a single Glt_{Ph} subunit proposed by Reyes et al. (2009). Starting from the left, the figure shows Glt_{Ph} in the outward facing conformation with HP2 (red) open followed by substrate/Na⁺ binding and HP2 closure and then translocation of the transport domain to the inward facing conformation. The final cartoon shows the uncharacterized hypothetical state with HP1 (yellow) gating substrate/Na⁺ release (Reyes et al., 2009).

Molecular dynamics and Glt_{Ph}

Computational molecular dynamics (MD) has traditionally allowed limited insights into the probable workings and movements within a molecular system. The far greater processor speeds of later generation computers coupled with more accurate and efficient algorithms that better estimate interactions at atomic and even quantum levels have greatly reduced the limitations of MD simulations. Even with these advances MD simulations of complicated systems (systems with 50,000 to 100,000 atoms) are still constrained by computational power and cumulative errors and rarely reach beyond 50 nanoseconds. This is, of course, a limited amount of time to derive movement within a protein. However, recent publications reporting on the molecular dynamics of Glt_{Ph} models show conformational changes during low nanosecond simulations (Huang and Tajkhorshid, 2008; Shrivastava et al., 2008), suggesting insights into the mechanics of EAAT transport are attainable.

To effectively mimic a transmembrane protein system the models must, not surprisingly, be embedded into a lipid bi-layer with water molecules added above and below the membrane to simulate an aqueous environment. Ions are added to both neutralize the system and to better imitate a functional reality. The most computationally expensive problem in MD simulations is calculating long- and short-range electrostatic interactions. For our purposes, electrostatic involvements are estimated using Ewald summations which sum short-range interactions (normally less than 4Ås) with real space resolution while simplifying long-range

interactions using Fourier transformations. Other variables such as pressure, energy, and heat capacities (thermodynamic properties of a system) and atomic positions and momentum (kinetic properties of a system) are calculated using statistical mechanics to estimate probable atomic positions and movement by applying experimentally derived thermodynamic properties.

Cation coordination

In chapters 2 and 3 of this dissertation we utilize an electrostatic mapping program called VALE (Nayal and Di Cera, 1993) that scans computational models of proteins for groupings of oxygen atoms to map potential cation coordination sites. These sites are scored through a fairly simple algorithm that incorporates empirically derived cation specific values with grid-based distances from oxygen atoms (see methods in chapter 2). This enabled us to predict novel cation sites for Na^+ and K^+ . In the following section I discuss structural aspects of cation binding sites with an emphasis on K^+ and Na^+ .

The membrane flux of Na^+ and K^+ complexed with the EAATs help fuel glutamate transport allowing up to a 10,000-fold concentration of glutamate (Schousboe and Divac, 1979). To deconstruct the mechanisms that allow this rather impressive driving force it is important to address how metal ions complex with proteins. A third of known macromolecules are metalloproteins (Castagnetto et al., 2002) with cations functioning to stabilize substrate protein interactions, drive catalysis and transport, and as allosteric modulators (Suelter, 1970; Page and Di Cera, 2006). Many macromolecules have evolved to take advantage of K^+ and Na^+ because of their availability in the environment. Determining how these specific cations coordinate with macromolecules requires kinetic and structural analysis. A review of metalloprotein crystal structures revealed that amino acid main chain carbonyl groups and side chain oxygens are the predominant donor groups for cation coordination, with rare coordination through the nitrogen lone pair of histidine's imidazole side chain (Harding, 2004). Figure 6 lists aspects of common bioactive metals showing K^+ and Na^+ prefer octahedral and trigonal bipyramidal geometries (Harding, 2002; <http://tanna.bch.ed.ac.uk>).

Metal	Na ⁺ sodium	K ⁺ potassium	Ca ²⁺ calcium	Mg ²⁺ magnesium
atomic number	11	19	20	12
Usual donor atoms	O main-chain O of asp, glu	O main-chain O of asp, glu	O main-chain O of asp, glu	O main-chain O of asp, glu
Other donor atoms	O of ser, thr O of asn, gln	O of ser, thr O of asn, gln	O of ser, thr O of asn, gln N of his	O of ser, thr O of asn, gln N of his
Usual coordination geometry	trigonal bipyramidal, square pyramidal, octahedral	trigonal bipyramidal, square pyramidal, octahedral	octahedral	octahedral
Typical metal-oxygen distance (Å)	2.35 - 2.45	2.75 - 2.85	2.45 - 2.45	2.05 - 2.15
Relative abundance in PDB	96	72	358	177

Figure 6. Compilation of common cation coordination donor atoms and geometries found in Protein Data Bank structures. 'O main-chain' stands for the protein main-chain carbonyl oxygen atom. Relative abundance in PDB is abundance of proteins containing the respective cation in the Protein Data Bank as of 2002. The table was adapted from Harding, 2002; Harding 2004; and <http://tanna.bch.ed.ac.uk>.

Structural studies have proven to be non-trivial especially when assigning electron densities to Na⁺ and K⁺ from X-ray scatter patterns. Na⁺, for example, has a small ionic radius (0.96Å) which is difficult to resolve in even high resolution structures (usually requiring resolutions of <1.6Å) (Harding, 2002). Na⁺ also has the same valence as a water molecule and can be difficult to differentiate from water (Nayal and Di Cera, 1996). Likewise K⁺ has a comparable ionic radius to water and can be similarly confused. Crystallographers circumvent this issue by using higher density surrogate cations. Boudker et al. (2007), for example, used thallium to gain a resolvable density in their GlT_{Ph} structures. They demonstrated the relevance of the Tl⁺ densities to Na⁺ binding through competition assays showing that the densities vanish when the crystals are soaked in salt buffers containing both cations. Cation promiscuity such as this cannot always be assumed and even subtle alterations can alter a site's capacity to complex with a specific cation. A good example of this is a glutamate to aspartate mutation in EAAT3 (E374D) which eradicates K⁺ countertransport (Kavanaugh et al., 1997).

Summary and overview of subsequent chapters

This initial chapter has provided a literature review and the necessary context for understanding chapters 2 and 3, which focus on EAAT structure and function. Chapter 4 explores the application and potential of computer modeling in different scenarios and chapter 5 considers avenues for future research. The following paragraphs provide an overview of the findings presented in chapters 2-4.

In chapter 2 we use electrostatic mapping of EAAT3 homology models and GltPh structures to determine novel cation coordination sites. We present three Na⁺ sites, two of which overlap the thallium densities resolved in the aspartate-bound structure reported by Boudker et al. (2007) and one new site capable of coordinating Na⁺ but not Tl⁺. We also describe a K⁺ site that overlaps the substrate binding site providing a possible mechanism for glutamate exclusion during the countertransport hemicycle. Together these sites suggest mechanisms for coupling the thermodynamically unfavorable transport of glutamate to the thermodynamically favorable transport of Na⁺ and antiport of K⁺.

In chapter 3 we integrate computational and electrophysical data to deconstruct cation and substrate binding order and release in the EAATs and present an incomplete but complex model showing sodium dependent HP2 movement precedes the HP2 occluded state. We also use electrostatic mapping combined with molecular dynamics simulations to investigate Na⁺ release from inward facing EAAT and GltPh models.

Chapter 4 of my dissertation shows how the application of computer modeling benefitted three collaborative studies, each involving different systems. The first study, published in 2004 (Poss et al., 2004) used comparative statistical analyses of homology models of variant Clade A HIV envelope proteins to help determine residues important during early infection. The second study (Hassani et al., 2005) evaluated novel lavendamycin analogues for their potential as anti-tumor agents. As part of the evaluation process, we used computational molecular docking of the analogue substrates into their targeted protein (NAD(P)H:quinone oxidoreductase (NQO1)) to help determine interactions that promote potency. The third study (Leary et al., submitted) used molecular docking to determine interactions between a potent EAAT1 and EAAT2 inhibitor (β -2-fluorenyl-aspartylamide, or 2-FAA) and found 2-FAA interactions differ from inhibitor interactions determined in the TBOA-bound GltPh crystal structure. Overall, the addition of a computational element to these investigations helped

validate and interpret *in vitro* work and led to a more refined understanding of the respective mechanisms of actions.

References

- Abramson J, Kaback HR, Iwata S (Structural comparison of lactose permease and the glycerol-3-phosphate antiporter: members of the major facilitator superfamily. *Current opinion in structural biology* 14:413-419.2004).
- Amara SG, Fontana AC (Excitatory amino acid transporters: keeping up with glutamate. *Neurochemistry international* 41:313-318.2002).
- Arriza JL, Eliasof S, Kavanaugh MP, Amara SG (Excitatory amino acid transporter 5, a retinal glutamate transporter coupled to a chloride conductance. *Proceedings of the National Academy of Sciences of the United States of America* 94:4155-4160.1997).
- Beart PM, O'Shea RD (Transporters for L-glutamate: an update on their molecular pharmacology and pathological involvement. *British journal of pharmacology* 150:5-17.2007).
- Behrens PF, Franz P, Woodman B, Lindenberg KS, Landwehrmeyer GB (Impaired glutamate transport and glutamate-glutamine cycling: downstream effects of the Huntington mutation. *Brain* 125:1908-1922.2002).
- Bendahan A, Armon A, Madani N, Kavanaugh MP, Kanner BI (Arginine 447 plays a pivotal role in substrate interactions in a neuronal glutamate transporter. *The Journal of biological chemistry* 275:37436-37442.2000).
- Bergles DE, Tzingounis AV, Jahr CE (Comparison of coupled and uncoupled currents during glutamate uptake by GLT-1 transporters. *J Neurosci* 22:10153-10162.2002).
- Borre L, Kanner BI (Coupled, but not uncoupled, fluxes in a neuronal glutamate transporter can be activated by lithium ions. *The Journal of biological chemistry* 276:40396-40401.2001).
- Bortolotto ZA, Clarke VR, Delany CM, Parry MC, Smolders I, Vignes M, Ho KH, Miu P, Brinton BT, Fantaske R, Ogden A, Gates M, Ornstein PL, Lodge D, Bleakman D, Collingridge GL (Kainate receptors are involved in synaptic plasticity. *Nature* 402:297-301.1999).
- Boudker O, Ryan RM, Yernool D, Shimamoto K, Gouaux E (Coupling substrate and ion binding to extracellular gate of a sodium-dependent aspartate transporter. *Nature* 445:387-393.2007).
- Bunch L, Erichsen MN, Jensen AA (Excitatory amino acid transporters as potential drug targets. *Expert opinion on therapeutic targets* 13:719-731.2009).
- Carlsson M, Carlsson A (Interactions between glutamatergic and monoaminergic systems within the basal ganglia--implications for schizophrenia and Parkinson's disease. *Trends in neurosciences* 13:272-276.1990).
- Castagnetto JM, Hennessy SW, Roberts VA, Getzoff ED, Tainer JA, Pique ME (MDB: the Metalloprotein Database and Browser at The Scripps Research Institute. *Nucleic acids research* 30:379-382.2002).
- Choi DW (Excitotoxic cell death. *Journal of neurobiology* 23:1261-1276.1992).
- Crisman TJ, Qu S, Kanner BI, Forrest LR (Inward-facing conformation of glutamate transporters as revealed by their inverted-topology structural repeats. *Proceedings of the National Academy of Sciences of the United States of America*.2009).

Curtis DR, Watkins JC (The excitation and depression of spinal neurones by structurally related amino acids. *Journal of neurochemistry* 6:117-141.1960).

Diamond JS, Jahr CE (Transporters buffer synaptically released glutamate on a submillisecond time scale. *J Neurosci* 17:4672-4687.1997).

Fairman WA, Vandenberg RJ, Arriza JL, Kavanaugh MP, Amara SG (An excitatory amino-acid transporter with properties of a ligand-gated chloride channel. *Nature* 375:599-603.1995).

Fonnum F (Glutamate: a neurotransmitter in mammalian brain. *Journal of neurochemistry* 42:1-11.1984).

Furuta A, Rothstein JD, Martin LJ (Glutamate transporter protein subtypes are expressed differentially during rat CNS development. *J Neurosci* 17:8363-8375.1997).

Gesemann M, Lesslauer A, Maurer CM, Schonhaler HB, Neuhauss SC (Phylogenetic analysis of the vertebrate excitatory/neutral amino acid transporter (SLC1/EAAT) family reveals lineage specific subfamilies. *BMC evolutionary biology* 10:117).

Grewer C, Rauen T (Electrogenic glutamate transporters in the CNS: molecular mechanism, pre-steady-state kinetics, and their impact on synaptic signaling. *The Journal of membrane biology* 203:1-20.2005).

Grewer C, Watzke N, Wiessner M, Rauen T (Glutamate translocation of the neuronal glutamate transporter EAAC1 occurs within milliseconds. *Proceedings of the National Academy of Sciences of the United States of America* 97:9706-9711.2000).

Groeneveld M, Slotboom DJ (Na(+):aspartate coupling stoichiometry in the glutamate transporter homologue Glt(Ph). *Biochemistry* 49:3511-3513).

Grunewald M, Bendahan A, Kanner BI (Biotinylation of single cysteine mutants of the glutamate transporter GLT-1 from rat brain reveals its unusual topology. *Neuron* 21:623-632.1998).

Harding MM (Geometry of metal-ligand interactions in proteins. *Acta crystallographica* 57:401-411.2001).

Harding MM (Metal-ligand geometry relevant to proteins and in proteins: sodium and potassium. *Acta crystallographica* 58:872-874.2002).

Harding MM (The architecture of metal coordination groups in proteins. *Acta crystallographica* 60:849-859.2004).

Hassani M, Cai W, Holley DC, Lineswala JP, Maharjan BR, Ebrahimian GR, Seradj H, Stocksdale MG, Mohammadi F, Marvin CC, Gerdes JM, Beall HD, Behforouz M (Novel lavendamycin analogues as antitumor agents: synthesis, in vitro cytotoxicity, structure-metabolism, and computational molecular modeling studies with NAD(P)H:quinone oxidoreductase 1. *Journal of medicinal chemistry* 48:7733-7749.2005).

Huang S, Ryan RM, Vandenberg RJ (The role of cation binding in determining substrate selectivity of glutamate transporters. *The Journal of biological chemistry* 284:4510-4515.2009).

Huang Z, Tajkhorshid E (Dynamics of the extracellular gate and ion-substrate coupling in the glutamate transporter. *Biophysical journal* 95:2292-2300.2008).

Ingram EM, Tessler S, Bowery NG, Emson PC (Glial glutamate transporter mRNAs in the genetically absence epilepsy rat from Strasbourg. *Brain research* 75:96-104.2000).

Kanai Y, Bhide PG, DiFiglia M, Hediger MA (Neuronal high-affinity glutamate transport in the rat central nervous system. *Neuroreport* 6:2357-2362.1995).

- Kanai Y, Hediger MA (The glutamate/neutral amino acid transporter family SLC1: molecular, physiological and pharmacological aspects. *Pflugers Arch* 447:469-479.2004).
- Kanai Y, Nussberger S, Romero MF, Boron WF, Hebert SC, Hediger MA (Electrogenic properties of the epithelial and neuronal high affinity glutamate transporter. *The Journal of biological chemistry* 270:16561-16568.1995).
- Kavanaugh MP, Bendahan A, Zerangue N, Zhang Y, Kanner BI (Mutation of an amino acid residue influencing potassium coupling in the glutamate transporter GLT-1 induces obligate exchange. *The Journal of biological chemistry* 272:1703-1708.1997).
- Nayal M, Di Cera E (Predicting Ca(2+)-binding sites in proteins. *Proceedings of the National Academy of Sciences of the United States of America* 91:817-821.1994).
- Nayal M, Di Cera E (Valence screening of water in protein crystals reveals potential Na⁺ binding sites. *Journal of molecular biology* 256:228-234.1996).
- Otis TS, Kavanaugh MP, Jahr CE (Postsynaptic glutamate transport at the climbing fiber-Purkinje cell synapse. *Science (New York, NY)* 277:1515-1518.1997).
- Page MJ, Di Cera E (Role of Na⁺ and K⁺ in enzyme function. *Physiological reviews* 86:1049-1092.2006).
- Poss M, Holley DC, Biek R, Cox H, Gerdes J (Development of a homology model for clade A human immunodeficiency virus type 1 gp120 to localize temporal substitutions arising in recently infected women. *The Journal of general virology* 85:1479-1484.2004).
- Reyes N, Ginter C, Boudker O (Transport mechanism of a bacterial homologue of glutamate transporters. *Nature* 462:880-885.2009).
- Rosental N, Bendahan A, Kanner BI (Multiple consequences of mutating two conserved beta-bridge forming residues in the translocation cycle of a neuronal glutamate transporter. *The Journal of biological chemistry* 281:27905-27915.2006).
- Ryan RM, Compton EL, Mindell JA (Functional characterization of a Na⁺-dependent aspartate transporter from *Pyrococcus horikoshii*. *The Journal of biological chemistry* 284:17540-17548.2009).
- Ryan RM, Mitrovic AD, Vandenberg RJ (The chloride permeation pathway of a glutamate transporter and its proximity to the glutamate translocation pathway. *The Journal of biological chemistry* 279:20742-20751.2004).
- Ryan RM, Vandenberg RJ (A channel in a transporter. *Clinical and experimental pharmacology & physiology* 32:1-6.2005).
- Schousboe A, Divac I (Difference in glutamate uptake in astrocytes cultured from different brain regions. *Brain Res* 177:407-409.1979).
- Shlaifer I, Kanner BI (Conformationally sensitive reactivity to permeant sulfhydryl reagents of cysteine residues engineered into helical hairpin 1 of the glutamate transporter GLT-1. *Molecular pharmacology* 71:1341-1348.2007).
- Shrivastava IH, Jiang J, Amara SG, Bahar I (Time-resolved mechanism of extracellular gate opening and substrate binding in a glutamate transporter. *The Journal of biological chemistry* 283:28680-28690.2008).
- Slotboom DJ, Konings WN, Lolkema JS (Structural features of the glutamate transporter family. *Microbiol Mol Biol Rev* 63:293-307.1999).
- Slotboom DJ, Sobczak I, Konings WN, Lolkema JS (A conserved serine-rich stretch in the glutamate transporter family forms a substrate-sensitive reentrant loop. *Proceedings of the National Academy of Sciences of the United States of America* 96:14282-14287.1999).

- Su ZZ, Leszczyniecka M, Kang DC, Sarkar D, Chao W, Volsky DJ, Fisher PB (Insights into glutamate transport regulation in human astrocytes: cloning of the promoter for excitatory amino acid transporter 2 (EAAT2). *Proceedings of the National Academy of Sciences of the United States of America* 100:1955-1960.2003).
- Sueller CH (Enzymes activated by monovalent cations. *Science (New York, NY)* 168:789-795.1970).
- Tao Z, Zhang Z, Grever C (Neutralization of the aspartic acid residue Asp-367, but not Asp-454, inhibits binding of Na⁺ to the glutamate-free form and cycling of the glutamate transporter EAAC1. *The Journal of biological chemistry* 281:10263-10272.2006).
- Teichman S, Kanner BI (Aspartate-444 is essential for productive substrate interactions in a neuronal glutamate transporter. *The Journal of general physiology* 129:527-539.2007).
- Vandenberg RJ, Huang S, Ryan RM (Slips, leaks and channels in glutamate transporters. *Channels (Austin, Tex)* 2:51-58.2008).
- Veruki ML, Morkve SH, Hartveit E (Activation of a presynaptic glutamate transporter regulates synaptic transmission through electrical signaling. *Nature neuroscience* 9:1388-1396.2006).
- Wadiche JI, Kavanaugh MP (Macroscopic and microscopic properties of a cloned glutamate transporter/chloride channel. *J Neurosci* 18:7650-7661.1998).
- Yernool D, Boudker O, Jin Y, Gouaux E (Structure of a glutamate transporter homologue from *Pyrococcus horikoshii*. *Nature* 431:811-818.2004).
- Zarbiv R, Grunewald M, Kavanaugh MP, Kanner BI (Cysteine scanning of the surroundings of an alkali-ion binding site of the glutamate transporter GLT-1 reveals a conformationally sensitive residue. *The Journal of biological chemistry* 273:14231-14237.1998).
- Zhang Y, Bendahan A, Zarbiv R, Kavanaugh MP, Kanner BI (Molecular determinant of ion selectivity of a (Na⁺ + K⁺)-coupled rat brain glutamate transporter. *Proceedings of the National Academy of Sciences of the United States of America* 95:751-755.1998).

Chapter 1: Interactions of alkali cations with glutamate transporters

David C. Holley and Michael P. Kavanaugh*

Center for Structural and Functional Neuroscience, University of Montana, Missoula, MT 59812, USA

The transport of glutamate is coupled to the co-transport of three Na⁺ ions and the countertransport of one K⁺ ion. In addition to this carrier-type exchange behaviour, glutamate transporters also behave as chloride channels. The chloride channel activity is strongly influenced by the cations that are involved in coupled flux, making glutamate transporters representative of the ambiguous interface between carriers and channels. In this paper, we review the interaction of alkali cations with glutamate transporters in terms of these diverse functions. We also present a model derived from electrostatic mapping of the predicted cation-binding sites in the X-ray crystal structure of the *Pyrococcus horikoshii* transporter Glt_{Ph} and in its human glutamate transporter homologue EAAT3. Two predicted Na⁺-binding sites were found to overlap precisely with the Tl⁺ densities observed in the aspartate-bound complex. A novel third site predicted to favourably bind Na⁺ (but not Tl⁺) is formed by interaction with the substrate and the occluding HP2 loop. A fourth predicted site in the apo state exhibits selectivity for K⁺ over both Na⁺ and Tl⁺. Notably, this K⁺ site partially overlaps the glutamate-binding site, and their binding is mutually exclusive. These results are consistent with kinetic and structural data and suggest a plausible mechanism for the flux coupling of glutamate with Na⁺ and K⁺ ions.

1. INTRODUCTION

In order to maintain chemical neurotransmission, prompt removal of neurotransmitter following synaptic release must occur. This is necessary for terminating the actions of the transmitter on the postsynaptic cell and for maintaining specificity of synaptic communication. In the case of glutamate, the principal excitatory neurotransmitter in the nervous system of vertebrates, it is also necessary to control extracellular transmitter levels in order to prevent excitotoxic damage from excessive receptor activity. This task is chiefly accomplished through reuptake mediated by excitatory amino acid transporters (EAAT1–5; SLC1A1–5) present in the plasma membranes of glia and neurons throughout the nervous system (Tzingounis & Wadiche 2007). A hallmark of glutamate uptake is co-transport with Na⁺ and H⁺ and countertransport of K⁺, indicative of a mixed co-transport-exchange carrier mechanism (Kanner & Sharon 1978). Another hallmark of the transporters is an intrinsic chloride conductance that is generally increased during transport in cells expressing exogenous or endogenous transporters (Fairman et al. 1995; Picaud et al. 1995; Wadiche et al. 1995; Billups et al. 1996; Wadiche & Kavanaugh 1998). A number of studies have addressed questions about the detailed mechanism of glutamate uptake and chloride channel gating, but questions still remain about fundamental features such as the binding order of transported

solute and the location of binding sites and permeation pathways (for reviews see Danbolt (2001), Grewer & Rauen (2005) and Tzingounis & Wadiche (2007)).

The solution of the crystal structure of Glt_{Ph}, a glutamate transporter homologue from *Pyrococcus horikoshii*, represents a critical advance towards a better understanding of the transport mechanism. The transporter has a trimeric architecture (Yernool et al. 2004). Each of the three subunits has eight transmembrane domains with two re-entrant helical hairpin loops (HP1 and HP2) that dip into the membrane from opposite sides (figure 1). Structural evidence suggests that each subunit in the trimer binds its amino acid substrate independently of the others (Yernool et al. 2004; Boudker et al. 2007). Functional evidence also supports the idea that each subunit operates as both a self-contained glutamate transporter and chloride channel (Grewer et al. 2005; Koch et al. 2007; Leary et al. 2007).

2. COMPUTATIONAL METHODS

Human EAAT3 sequence (GenBank; <http://www.ncbi.nlm.nih.gov>) and the EAAT3 R447C mutant sequence were aligned with the Protein Data Bank (PDB) sequences for the Glt_{Ph} homologue (2NWX and 2NWW; Yernool et al. 2004; Boudker et al. 2007). Homology models were built by threading the aligned EAAT3 sequences along their respective PDB coordinates using the SwissProt server (<http://swissmodel.expasy.org/SWISS-MODEL.html>). The resulting models were optimized through local energy minimizations of regions with steric and electrostatic interference

* Author for correspondence (michael.kavanaugh@umontana.edu).

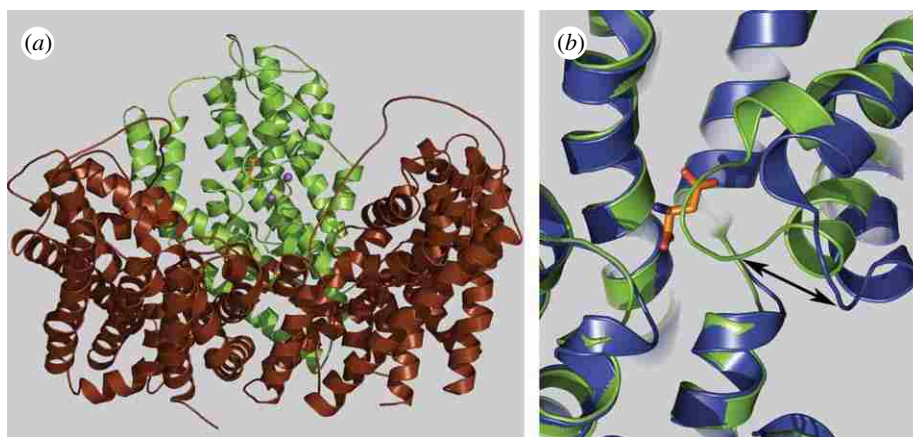


Figure 1. Glt_{Ph} structure model based on Yernool *et al.* (2004). (a) Three subunits form a bowl that penetrates the plasma membrane. One of the subunits is depicted with aspartate and two bound Tl⁺ (Boudker *et al.* 2007). (b) Single subunit overlays of the occluded (green) and open (blue) conformations with aspartate bound to the occluded form. The arrow highlights the HP2-loop conformational change between the open and occluded forms.

using the AMBER7 force field in the TRIPOS SYBYL7.3 platform. Valence shell mapping and calculations were performed using the FORTRAN program VALE (courtesy of Enrico Di Cera and Thierry Rose; Washington University, St Louis, MO) using a 3.4 Å probe radius and a grid size of 0.1 Å (Nayal & Di Cera 1994) on Glt_{Ph} and homology model PDB files. Only coordination sites within a 10 Å radius of the substrate α -carbon imported from the aspartate-bound crystal structure were considered as candidates for the Na⁺- and K⁺-binding sites. Calculations for each cation–oxygen pair are given by $\nu = (R/R_1)^{-N}$, where R is the distance of an oxygen atom to the cation; R_1 is the distance given valence = 1.0; and N is an empirically derived exponent specific to each cation (Nayal & Di Cera 1994, 1996; Page & Di Cera 2006). The values for R_1 and N were determined through the analysis of metal–oxide crystal structures and define an estimated ideal bond strength as $\nu = 1.0$. Although all pertinent regions of the 10 Å binding arena are likely to be water accessible, no water molecules were included in the valence mapping in order to reduce noise (Nayal & Di Cera 1994). Consistent with recent studies, we chose a valence cut-off of $\nu = 0.9$ for likely candidate-binding sites (Ogawa & Toyoshima 2002; Rakowski & Sagar 2003; Page & Di Cera 2006). The three-dimensional coordinates of valence maps that contain multiple, clustered valence sites within a 2 Å radius were included as a single site and we reported the highest estimated valence within each site. L-Glutamate was docked using GOLD (<http://www.ccdc.cam.ac.uk/>) into the EAAT3 and Glt_{Ph} models either containing Na⁺ or K⁺, as determined by valence mapping, or containing no cations. The top-ranked structures determined by CHEMScore (<http://www.ccdc.cam.ac.uk/>) were incorporated into the appropriate models and average rankings from three separate GOLD docking runs were reported. In order to evaluate estimations of absolute affinity of substrates in different models, ΔG scores were extracted from CHEMScore and reported as an average over the three docking runs. In order to optimize models, iterative valence mapping and docking runs were performed.

3. THERMODYNAMIC COUPLING OF GLUTAMATE AND CATION FLUXES

Influx of glutamate, Na⁺ and H⁺, and efflux of K⁺, during a transport cycle results in a net flow of positive charge into the cell that can be recorded with a voltage clamp circuit. A tight stoichiometric coupling is inferred from the effects of these cations' concentration gradients on the reversal potential of the pharmacologically isolated transport current. The transporter reversal potential (the equilibrium membrane potential at which there is no net transport) follows the predictions of the free energy equation for the coupled transport of one glutamate molecule with one proton and three Na⁺ ions and countertransport of one K⁺ ion during each uptake cycle (Zerangue & Kavanaugh 1996a; Levy *et al.* 1998). An overarching question concerns the mechanism of this tight coupling. The simplest type of theoretical kinetic scheme consistent with the data is an alternating access carrier model (Jardetzky 1966). The precise binding order of ions and glutamate is unresolved; the kinetic data suggest that one or two of the three Na⁺ ions bind before glutamate (Tzingounis & Wadiche 2007). The solution of two crystallized structural states of Glt_{Ph} has provided critical new information and suggests a possible structural mechanism for an alternating access transport scheme (Boudker *et al.* 2007). The trimer subunits contain eight transmembrane domains (TM1–8) and two α -helical, re-entrant hairpin loops (internal HP1 and external HP2). Gouaux and colleagues have suggested that these loops could function as gates, allowing alternating substrate access. In the aspartate-bound state, aspartate is occluded between the tips of the two re-entrant loops, and charge pairing between the bound aspartate and residues including a conserved arginine in TM8 of the transporter stabilizes the complex. Two anomalous densities can be resolved that are associated with the replacement of Na⁺ by Tl⁺ in the aspartate complex. By contrast, in crystals produced from transporter complexed with the bulky non-transported inhibitor D,L-threo- β -benzoylaspartic acid (TBOA), the external HP2 loop is swung outwards, approximately 10 Å, and one of the ion densities is disrupted. These data suggest

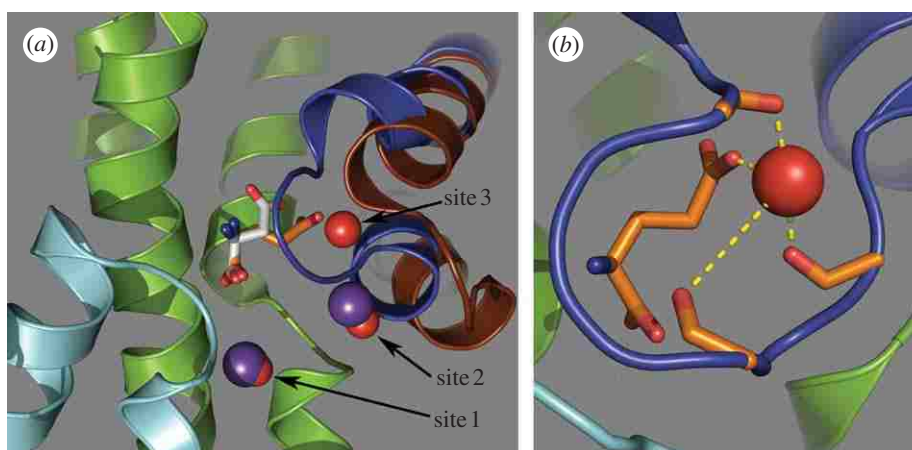


Figure 2. Identification of a novel sodium site in EAAT3. (a) Sodium sites 1–3 (red spheres) are depicted, showing the proximity of sites 1 and 3 to the crystal structure thallium sites (purple spheres) identified by Boudker *et al.* (2007). The site 2-bound ion interacts with the HP2 helix dipole and the γ -carboxyl group of docked glutamate (orange sticks). Overlaid with the docked glutamate molecule is the aspartate (white sticks) that was resolved in the crystal structure. The HP1 loop is depicted in cyan, with the occluding HP2 loop in dark blue. (b) Na^+ docked at site 3 is coordinated by α -carboxyl groups in the HP2 loop and by the γ -carboxylate of bound glutamate.

a possible docking trajectory and structural gating mechanism for the first hemicycle of an alternating access kinetic scheme (figure 1). A presumed third state, which would allow the substrate and the cations access to the cytoplasm, has thus far eluded crystallization.

4. THERMODYNAMICALLY UNCOUPLED CHLORIDE FLUX

In addition to the flux of stoichiometrically coupled ions, chloride flux also occurs through the transporters (for a review, see Tzingounis & Wadiche (2007)). This was first suggested by the presence of a chloride current associated with the activation of the native glutamate transporters in retinal neurons and glia (Eliasof & Werblin 1993; Picaud *et al.* 1995; Billups *et al.* 1996; Eliasof & Jahr 1996), and it has also been demonstrated to occur with EAATs exogenously expressed in different cell systems (Fairman *et al.* 1995). The channel is also found in neutral amino acid transporter members of the eukaryotic SLC1 family (Zerangue & Kavanaugh 1996b). At some synapses, the chloride conductance appears to play feedback roles in synaptic signalling, which are entirely distinct from the effects of uptake on glutamate dynamics (Veruki *et al.* 2006; Wersinger *et al.* 2006). The chloride channel itself seems to be intrinsic to the transporter, as the mutation of specific residues leads to discrete changes in anion channel properties (Ryan *et al.* 2004; Huang & Vandenberg 2007). The chloride channel function is also conserved in a reconstituted bacterial homologue, further supporting the idea of a channel in the transporter structure (Ryan & Mindell 2007). The net current activated by glutamate (reflecting both the stoichiometrically coupled and Cl^- currents) has a distinct reversal potential in each EAAT isoform, suggesting that each has a fixed and unique Cl^- current magnitude relative to the stoichiometrically coupled current. The relative magnitude of anion conductance : coupled current follows the sequence EAAT4 ~ EAAT5 > EAAT1 > EAAT3 > EAAT2. In each transporter, the anion conductance displays a

chaotropic selectivity sequence $\text{SCN}^- > \text{ClO}_4^- > \text{NO}_3^- > \text{I}^- > \text{Cl}^- > \text{F}^- \gg \text{gluconate}^-$. SCN^- is approximately 70-fold more permeant than Cl^- (Wadiche & Kavanaugh 1998). The glutamate-dependent anion conductance is strongly affected by the identity of the alkali cation co-transported with glutamate; Li^+ can substitute for Na^+ in some isoforms to support glutamate transport but is much less efficacious at activating the anion conductance (Borre & Kanner 2001). With Na^+ present, there is a tonic anion conductance in the absence of glutamate (Bergles & Jahr 1997; Tao *et al.* 2006).

Replacement of Cl^- with impermeant anions such as gluconate does not affect the transport of glutamate (Wadiche *et al.* 1995). Thus, Cl^- flux may be considered thermodynamically uncoupled from glutamate flux, and seems to involve a channel-like mechanism instead. Indeed, glutamate-dependent anion current fluctuations have been observed with endogenous and exogenous transporter expressions that are consistent with a stochastically gated channel that is kinetically related to the glutamate transport cycle (Picaud *et al.* 1995; Wadiche & Kavanaugh 1998). Kinetic analysis of the glutamate concentration dependence of transport and chloride conductance suggests that each subunit in the trimer harbours both a chloride channel and a glutamate transporter, and each subunit functions independently (Koch *et al.* 2007; Leary *et al.* 2007). Kinetic models may be able to unify the distinct channel and transport functions by representing a subset of the Markov states in the transport cycle as open-channel states (Greuer *et al.* 2000; Otis & Kavanaugh 2000; Bergles *et al.* 2002).

5. STRUCTURAL MODEL FOR FLUX COUPLING

An initial picture of the interaction of alkali cations with glutamate transporters has emerged from anomalous difference maps seen in Tl^+ -soaked Glt_{Ph} crystals (Boudker *et al.* 2007). Two densities were seen that were selectively diminished by Na^+ . One of these (site 2) was not seen in transporters complexed with TBOA, which also caused a large outward

Table 1. Electrostatic calculations for Na⁺- and K⁺-binding sites in EAAT3. (Sites 1–4 refer to potential cation-binding sites within 10 Å of the amino acid-binding site for the EAAT3 homology models and the Glt_{ph} X-ray crystal structures. The EAAT3 and Glt_{ph} models used for the valence calculations are in either the HP2-loop open or HP2-loop closed conformations and either the substrate-bound (glutamate or aspartate) or apo form.)

	site 1	site 2	site 3	site 4
EAAT3				
sodium				
EAAT3wt open apo	0.80	<0.3	0.72	0.84
EAAT3wt open L-glu	0.80	<0.3	0.72	<0.3
EAAT3wt closed apo	1.04	0.93	0.62	0.97
EAAT3wt occluded L-glu	1.04	0.93	0.91	<0.3
thallium				
EAAT3wt open apo	0.91	<0.3	<0.3	0.56
EAAT3wt closed apo	0.80	0.84	<0.3	0.94
EAAT3wt occluded L-glu	0.78	0.79	<0.3	<0.3
potassium				
EAAT3wt open apo	1.16	<0.3	<0.3	1.11
EAAT3wt open L-glu	1.16	<0.3	<0.3	<0.3
EAAT3wt closed apo	1.13	1.21	0.87	1.44
EAAT3wt occluded L-glu	1.13	1.21	<0.3	<0.3
caesium				
EAAT3wt open apo	1.03	<0.3	<0.3	0.90
EAAT3wt closed apo	0.71	0.83	<0.3	1.07
EAAT3wt occluded L-glu	0.71	0.83	<0.3	<0.3
Glt _{ph}				
sodium				
Glt _{ph} open apo	1.27	0.56	0.91	0.81
Glt _{ph} open L-asp	1.27	0.56	0.91	<0.3
Glt _{ph} occluded L-asp	1.05	1.05	0.61	<0.3
thallium				
Glt _{ph} open TBOA	1.09	0.46	<0.3	<0.3
Glt _{ph} occluded L-asp	1.07	1.08	<0.3	<0.3

displacement of the HP2 loop (figure 1). Because the crystal diffraction resolution was insufficient to localize Na⁺ ions interacting with Glt_{ph}, and owing to the possibility that the Tl⁺ sites might not accurately represent these sites, we used the electrostatic mapping algorithm VALE (Nayal & Di Cera 1994) to examine potential Na⁺-, K⁺- and Tl⁺-binding sites in the transporter. Electrostatic calculations with this algorithm have been successfully used to predict Na⁺- and K⁺-binding sites in proteins including the Na⁺, K⁺-ATPase (Nayal & Di Cera 1996; Ogawa & Toyoshima 2002; Rakowski & Sagar 2003).

The Glt_{ph} and EAAT3 models used for the valence calculations consist of four basic structures: the two loop conformers (HP1 open or closed) with or without the bound amino acid substrate (see figure 1 and §2). A total of four binding sites were identified corresponding to potential ion coordination sites above the 0.9 valence cut-off within a 10 Å radius of the substrate-binding site. In several of these ion-binding sites, the valence was dependent on the loop position and the presence or absence of glutamate or aspartate (table 1). For both the Glt_{ph} and the EAAT3 models, two sites (sites 1 and 2) are predicted, which correspond very well (less than 1.4 Å) to the Tl⁺ densities resolved in the occluded Glt_{ph} crystal structure determined by Boudker *et al.* (figure 2; table 1). The valence of site 1 is relatively independent of substrate binding and loop conformation, and is therefore likely to coordinate a sodium ion before glutamate is bound. By contrast, site 2 is coordinated by dipoles formed from α -helices

in the closed HP2 loop and TM7. This is consistent with the crystal structures, where one Tl⁺ density (site 1) was unaffected by the HP2-loop state, but the second density (site 2) was lost in the TBOA-bound open-loop state (Boudker *et al.* 2007).

Electrostatic mapping of EAAT3 also revealed a coordination shell for a novel site (site 3, figure 2) whose interaction with Na⁺ was favoured by bound glutamate. Na⁺ is predicted to be more stably coordinated in the occluded, substrate-bound state ($\nu=0.91$) than in either the open or closed apo states ($\nu=0.72$ or 0.62 , respectively; table 1). This glutamate effect arises from the contribution of a ligating oxygen to the site 3 coordination shell by the γ -carboxyl group of bound glutamate. Steric and van der Waals constraints between the bound ion and the occluding HP2 loop may also confer sodium selectivity at site 3, which shows poor predicted K⁺ and Tl⁺ valences ($\nu<0.3$). Site 3 thus represents a potential third Na⁺-selective binding site that could participate in cooperative binding of glutamate (figure 2). Valence modelling of Glt_{ph} predicts a tenuous coordination for Na⁺ in site 3 ($\nu=0.61$), but does not predict a viable coordination site for Tl⁺ at this site ($\nu<0.3$), which is consistent with the absence of Tl⁺ density at site 3 in Glt_{ph}. Electrostatic mapping also predicts a fourth cation-binding site in the transporter (figure 3). Site 4 exhibits a marked selectivity for K⁺ over Na⁺ (table 1; figure 3). This site also substantially overlaps the glutamate/aspartate-binding site. It includes a contribution from carboxyl groups of D444, a residue that is essential for

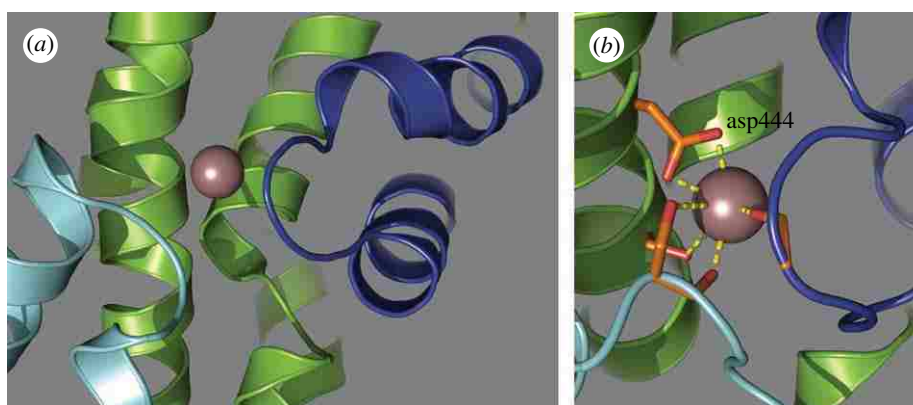


Figure 3. Interactions of K^+ at site 4. (a) Site 4 overlaps with the aspartate-binding site in the crystal structure of the aspartate-bound archaeal homologue. (b) Bound K^+ is predicted to interact directly with D444, a residue also involved in glutamate binding (Teichman & Kanner 2007).

Table 2. Substrate docking studies showing the effects of Na^+ on binding affinity in the EAAT3 homology models and the Glt_{Ph} X-ray crystal structures. (The HP2-loop occluded or open models were docked with L-glutamate and L-aspartate using the GOLD software program and the structures were scored using CHEMScore, where higher CHEMScore values reflect better fitness for docked poses. All models contained either no Na^+ ions or Na^+ ions at site 1 (Na1), sites 1 and 2 (Na1+Na2), sites 1 and 3 (Na1+Na3) or sites 1, 2 and 3 (Na1+Na2+Na3).)

	CHEMScore	ΔG (kJ mol ⁻¹)
EAAT3 L-glu no Na occluded	13.17	-17.08
EAAT3 L-glu Na1 occluded	14.36	-18.01
EAAT3 L-glu Na1 + Na2 occluded	14.11	-17.83
EAAT3 L-glu Na1 + Na3 occluded	17.61	-26.20
EAAT3 L-glu Na1 + Na2 + Na3 occluded	18.45	-27.00
Glt_{Ph} L-glu Na1 + Na2 occluded	14.74	-23.54
Glt_{Ph} L-glu Na1 + Na2 + Na3 occluded	18.42	-26.35
Glt_{Ph} L-asp Na1 + Na2 occluded	20.68	-24.00
Glt_{Ph} L-asp Na1 + Na2 + Na3 occluded	23.71	-28.00

glutamate binding (Teichman & Kanner 2007). Because K^+ binding to this site is predicted to be mutually exclusive with glutamate binding (tables 1 and 2), it is an interesting candidate for a K^+ countertransport site.

In order to further identify glutamate–cation interactions and to quantify the reciprocal effects of cations on glutamate affinity, we docked glutamate into the EAAT3 homology model using the GOLD docking program and estimated relative affinity using the CHEMScore scoring algorithm (Ferrara *et al.* 2004). We also extracted the ΔG component of the CHEMScore function in order to estimate the magnitude of energy change between the different conformational and cation-bound protein states. As expected from valence mapping, docking results indicate that Na^+ positioned at site 3 increases the estimated affinity of glutamate for the EAAT3-binding site, as reflected by both the CHEMScore and ΔG calculations (table 2).

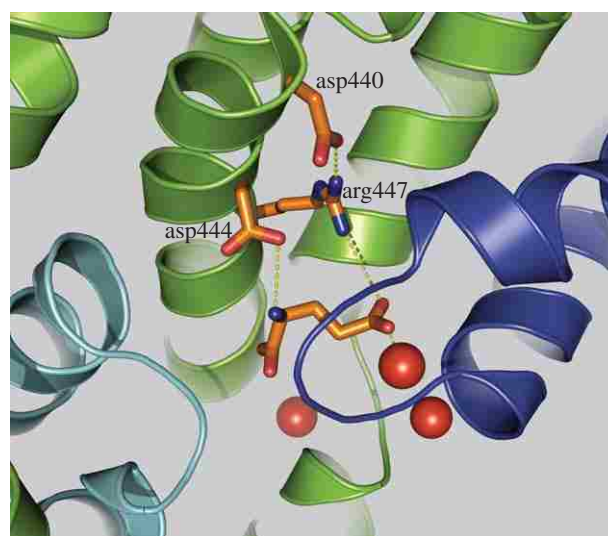


Figure 4. Potential binding pocket interactions facilitating coordinated substrate and Na^+ binding (see §6).

The docking results in conjunction with the valence estimates for site 3 in the glutamate-bound and apo forms suggest that Na^+ bound at site 3 stabilizes bound glutamate in the correct orientation by interacting with the glutamate γ -carboxyl group.

6. CONCLUSIONS

A combination of crystallographic, kinetic and electrostatic modelling data is beginning to provide a framework for understanding the mechanisms underlying the coupled fluxes of glutamate and alkali cations in glutamate transporters. Electrostatic modelling is consistent with crystallographic data, indicating that binding site 2 for Na^+ , coordinated by dipoles formed from the α -helices in the HP2 loop and TM7, is favoured by the transporter state in which the substrate is occluded. The highly conserved NMDG motif that disrupts the α -helix in TM7 facilitates dipole interactions with Na^+ and suggests a possible ubiquitous Na^+ ion-binding site across all homologous transporters. Boudker *et al.* suggest that Na^+ (Tl^+) binding to this site may act to lock the HP2 loop into the occluded conformation. Our data help to substantiate this idea as well as indicate that glutamate must be bound and occluded in order for the closed

HP2-loop conformation to be stable. This implies that Na⁺ binding at site 2 must occur concurrently with or following glutamate binding.

Analysis of the electrostatic mapping indicates a novel binding site for a third sodium ion that is not seen as a T1⁺ density in the Glt_{Ph} crystal structure. This is consistent with the poor valence predicted for T1⁺ at this site (table 1). Cooperative binding of Na⁺ and glutamate is a kinetic hallmark of the transporters. The γ -carboxyl group of glutamate is required for the stable coordination of Na⁺ at site 3, and occupancy of site 3 by Na⁺ has a reciprocal effect on glutamate affinity, suggesting a mechanism for this cooperativity. In a recent molecular dynamics study of Glt_{Ph}, interactions between bound glutamate carboxyl groups and Na⁺ were found to stabilize the complex in the binding pocket, consistent with this notion (Shrivastava *et al.* 2008).

Residue R447 in EAAT3 also interacts with the γ -carboxyl group of glutamate and is responsible for the recognition of acidic amino acid substrates (Bendahhan *et al.* 2000; Yernool *et al.* 2004). Neutralization of an aspartate residue (D440) proximal to R447 in TM8 reduces both glutamate and Na⁺ apparent affinities (Tao & Grewer 2007). The effect of this mutation on Na⁺ binding was exclusive to the glutamate-bound but not the apo form of the transporter. Our electrostatic mapping of Na⁺ at site 3 could explain these findings through an interaction of D440 with R447 that positions R447 for glutamate binding (figure 4). Thus, neutralization of D440 would disrupt the orientation of R447, which, in turn, would disrupt the interaction of the transporter with the glutamate γ -carboxyl group. The binding of Na⁺ at site 3 would be reciprocally affected by reducing the likelihood that glutamate is situated for Na⁺ coordination.

The properties of the Na⁺ coordination sites identified by electrostatic mapping suggest that site 1 may be occupied before glutamate binding, while the sites 2 and 3 involve coordinated interactions with bound glutamate and the HP2 loop. The K⁺-selective binding site predicted here is coordinated in part by D444, which has been shown to affect substrate affinity in EAAT3 (Teichman & Kanner 2007) and is part of the aspartate-binding site in the Glt_{Ph} crystal structure (Boudker *et al.* 2007). The interaction of K⁺ at this site excludes binding of amino acid substrates (table 1; figure 3), and thus could provide a simple potential mechanism for K⁺ countertransport, another hallmark of glutamate transporter function (Kanner & Sharon 1978).

This work was supported by grants from the NIH (NS033270, RR015583).

REFERENCES

- Bendahhan, A., Armon, A., Madani, N., Kavanaugh, M. P. & Kanner, B. I. 2000 Arginine 447 plays a pivotal role in substrate interactions in a neuronal glutamate transporter. *J. Biol. Chem.* **275**, 37 436–37 442. (doi:10.1074/jbc.M006536200)
- Bergles, D. E. & Jahr, C. E. 1997 Synaptic activation of glutamate transporters in hippocampal astrocytes. *Neuron* **19**, 1297–1308. (doi:10.1016/S0896-6273(00)80420-1)
- Bergles, D. E., Tzingounis, A. V. & Jahr, C. E. 2002 Comparison of coupled and uncoupled currents during glutamate uptake by GLT-1 transporters. *J. Neurosci.* **23**, 10 153–10 162.
- Billups, B., Rossi, D. & Attwell, D. 1996 Anion conductance behavior of the glutamate uptake carrier in salamander retinal glial cells. *J. Neurosci.* **16**, 6722–6731.
- Borre, L. & Kanner, B. I. 2001 Coupled, but not uncoupled, fluxes in a neuronal glutamate transporter can be activated by lithium ions. *J. Biol. Chem.* **276**, 40 396–40 401. (doi:10.1074/jbc.M104926200)
- Boudker, O., Ryan, R. M., Yernool, D., Shimamoto, K. & Gouaux, E. 2007 Coupling substrate and ion binding to extracellular gate of a sodium-dependent aspartate transporter. *Nature* **445**, 387–393. (doi:10.1038/nature05455)
- Danbolt, N. C. 2001 Glutamate uptake. *Prog. Neurobiol.* **65**, 1–105. (doi:10.1016/S0301-0082(00)00067-8)
- Eliasof, S. & Jahr, C. E. 1996 Retinal glial cell glutamate transporter is coupled to an anionic conductance. *Proc. Natl Acad. Sci. USA* **93**, 4153–4158. (doi:10.1073/pnas.93.9.4153)
- Eliasof, S. & Werblin, F. 1993 Characterization of the glutamate transporter in retinal cones of the tiger salamander. *J. Neurosci.* **13**, 402–411.
- Fairman, W. A., Vandenberg, R. J., Arriza, J. L., Kavanaugh, M. P. & Amara, S. G. 1995 An excitatory amino-acid transporter with properties of a ligand-gated chloride channel. *Nature* **375**, 599–603. (doi:10.1038/375599a0)
- Ferrara, P., Gohlke, H., Price, D. J., Klebe, G. & Brooks III, C. L. 2004 Assessing scoring functions for protein–ligand interactions. *J. Med. Chem.* **47**, 3032–3047. (doi:10.1021/jm030489h)
- Grewer, C. & Rauen, T. 2005 Electrogenic glutamate transporters in the CNS: molecular mechanism, pre-steady-state kinetics, and their impact on synaptic signaling. *J. Membr. Biol.* **203**, 1–20. (doi:10.1007/s00232-004-0731-6)
- Grewer, C., Watzke, N., Wiessner, M. & Rauen, T. 2000 Glutamate translocation of the neuronal glutamate transporter EAAC1 occurs within milliseconds. *Proc. Natl Acad. Sci. USA* **97**, 9706–9711. (doi:10.1073/pnas.160170397)
- Grewer, C., Balani, P., Weidenfeller, C., Bartusel, T., Tao, Z. & Rauen, T. 2005 Individual subunits of the glutamate transporter EAAC1 homotrimer function independently of each other. *Biochemistry* **35**, 11 913–11 923. (doi:10.1021/bi050987n)
- Huang, S. & Vandenberg, R. J. 2007 Mutations in transmembrane domains 5 and 7 of the human excitatory amino acid transporter 1 affect the substrate-activated anion channel. *Biochemistry* **46**, 9685–9692. (doi:10.1021/bi700647f)
- Jardetzky, O. 1966 Simple allosteric model for membrane pumps. *Nature* **211**, 969–970. (doi:10.1038/211969a0)
- Kanner, B. I. & Sharon, I. 1978 Active transport of glutamate by membrane vesicles isolated from rat brain. *Biochemistry* **17**, 3949–3953. (doi:10.1021/bi00612a011)
- Koch, H. P., Brown, R. L. & Larsson, H. P. 2007 The glutamate-activated anion conductance in excitatory amino acid transporters is gated independently by the individual subunits. *J. Neurosci.* **27**, 2943–2947. (doi:10.1523/JNEUROSCI.0118-07.2007)
- Leary, G. P., Stone, E. F., Holley, D. C. & Kavanaugh, M. P. 2007 The glutamate and chloride permeation pathways are colocalized in individual neuronal glutamate transporter subunits. *J. Neurosci.* **27**, 2938–2942. (doi:10.1523/JNEUROSCI.4851-06.2007)
- Levy, L. M., Warr, O. & Attwell, D. 1998 Stoichiometry of the glial glutamate transporter GLT-1 expressed inducibly

- in a Chinese hamster ovary cell line selected for low endogenous Na⁺-dependent glutamate uptake. *J. Neurosci.* **18**, 9620–9628.
- Nayal, M. & Di Cera, E. 1994 Predicting Ca²⁺-binding sites in proteins. *Proc. Natl Acad. Sci. USA* **91**, 817–821. (doi:10.1073/pnas.91.2.817)
- Nayal, M. & Di Cera, E. 1996 Valence screening of water in protein crystals reveals potential Na⁺ binding sites. *J. Mol. Biol.* **256**, 228–234. (doi:10.1006/jmbi.1996.0081)
- Ogawa, H. & Toyoshima, C. 2002 Homology modeling of the cation binding sites of Na⁺K⁺-ATPase. *Proc. Natl Acad. Sci. USA* **99**, 15 977–15 982. (doi:10.1073/pnas.2026 22299)
- Otis, T. S. & Kavanaugh, M. P. 2000 Isolation of current components and partial reaction cycles in the glial glutamate transporter EAAT2. *J. Neurosci.* **20**, 2749–2757.
- Page, M. J. & Di Cera, E. 2006 Role of Na⁺ and K⁺ in enzyme function. *Physiol. Rev.* **86**, 1049–1092. (doi:10.1152/physrev.00008.2006)
- Picaud, S. A., Larsson, H. P., Grant, G. B., Lecar, H. & Werblin, F. S. 1995 Glutamate-gated chloride channel with glutamate-transporter-like properties in cone photoreceptors of the tiger salamander. *J. Neurophysiol.* **74**, 1760–1771.
- Rakowski, R. F. & Sagar, S. 2003 Found: Na⁺ and K⁺ binding sites of the sodium pump. *News Physiol. Sci.* **18**, 164–168.
- Ryan, R. M. & Mindell, J. A. 2007 The uncoupled chloride conductance of a bacterial glutamate transporter homolog. *Nat. Struct. Mol. Biol.* **14**, 365–371. (doi:10.1038/nsmbl230)
- Ryan, R. M., Mitrovic, A. D. & Vandenberg, R. J. 2004 The chloride permeation pathway of a glutamate transporter and its proximity to the glutamate translocation pathway. *J. Biol. Chem.* **279**, 20 742–20 751. (doi:10.1074/jbc.M304433200)
- Shrivastava, I. H., Jiang, J., Amara, S. G. & Bahar, I. 2008 Time-resolved mechanism of extracellular gate opening and substrate binding in glutamate transporter. *J. Biol. Chem.* **283**, 28 680–28 690. (doi:10.1074/jbc.M80088 9200)
- Tao, Z. & Grewer, C. 2007 Cooperation of the conserved aspartate 439 and bound amino acid substrate is important for high-affinity Na⁺ binding to the glutamate transporter EAAC1. *J. Gen. Physiol.* **129**, 331–344. (doi:10.1085/jgp.200609678)
- Tao, Z., Zhang, Z. & Grewer, C. 2006 Neutralization of the aspartic acid residue Asp-367, but not Asp-454, inhibits binding of Na⁺ to the glutamate-free form and cycling of the glutamate transporter EAAC1. *J. Biol. Chem.* **281**, 10 263–10 272. (doi:10.1074/jbc.M510739200)
- Teichman, S. & Kanner, B. I. 2007 Aspartate-444 is essential for productive substrate interactions in a neuronal glutamate transporter. *J. Gen. Physiol.* **129**, 527–539. (doi:10.1085/jgp.200609707)
- Tzingounis, A. V. & Wadiche, J. I. 2007 Glutamate transporters: confining runaway excitation by shaping synaptic transmission. *Nat. Rev. Neurosci.* **8**, 935–947. (doi:10.1038/nrn2274)
- Veruki, M. L., Mørkve, S. H. & Hartveit, E. 2006 Activation of a presynaptic glutamate transporter regulates synaptic transmission through electrical signaling. *Nat. Neurosci.* **9**, 1388–1396. (doi:10.1038/nn1793)
- Wadiche, J. I. & Kavanaugh, M. P. 1998 Macroscopic and microscopic properties of a cloned glutamate transporter/chloride channel. *J. Neurosci.* **18**, 7650–7661.
- Wadiche, J. I., Amara, S. G. & Kavanaugh, M. P. 1995 Ion fluxes associated with excitatory amino acid transport. *Neuron* **15**, 721–728. (doi:10.1016/0896-6273(95)90159-0)
- Wersinger, E., Schwab, Y., Sahel, J. A., Rendon, A., Pow, D. V., Picaud, S. & Roux, M. J. 2006 The glutamate transporter EAAT5 works as a presynaptic receptor in mouse rod bipolar cells. *J. Physiol.* **577**, 221–234. (doi:10.1113/jphysiol.2006.118281)
- Yernool, D., Boudker, O., Jin, Y. & Gouaux, E. 2004 Structure of a glutamate transporter homologue from *Pyrococcus horikoshii*. *Nature* **431**, 811–818. (doi:10.1038/nature03018)
- Zerangue, N. & Kavanaugh, M. P. 1996a Flux coupling in a neuronal glutamate transporter. *Nature* **383**, 634–637. (doi:10.1038/383634a0)
- Zerangue, N. & Kavanaugh, M. P. 1996b ASCT-1 is a neutral amino acid exchanger with chloride channel activity. *J. Biol. Chem.* **271**, 27 991–27 994. (doi:10.1074/jbc.271.45.27991)

Chapter 2: A model for sequential binding in glutamate transporters

D.C. Holley, G.P. Leary, and M.P. Kavanaugh
Center for Structural and Functional Neuroscience, Departments of Biomedical and
Pharmaceutical Sciences, University of Montana, Missoula, MT

Abstract

Excitatory amino acid transporters (EAAT1-5) clear the synaptic cleft of glutamate after synaptic transmission through an electrogenic process, coupling thermodynamically unfavorable glutamate transport to thermodynamically favorable co-transport of a proton and 3Na^+ and the countertransport of 1K^+ . There are several X-ray crystal structures of an homologous archaeal transporter resolved in both outward (facing the cytosol) and inward (facing the extracellular fluid) conformations. The crystal structures poised in the outward-facing conformation show access to substrate binding is gated by a hairpin re-entrant loop (HP2) that is either oriented in open or occluded conformations (Boudker et al., 2007). Here we assemble physical and computational data into an incomplete but consistent and cohesive model for sequential transport. We deconstruct Na^+ cooperativity during the early transport hemi-cycle into two sodium dependent processes that contribute either to HP2 movement or substrate translocation. Specifically, we provide evidence that Na^+ cooperatively locks HP2 into an open conformation prior to glutamate binding and then into the occluded, closed conformation after glutamate is bound. Electrostatic mapping of the inward-facing model reveals decreased capacities at sites 2 and 3 for Na^+ coordination relative to the outward-facing model. This is partially borne out during molecular dynamics simulations of the inward-facing conformation of Glt_{Ph} that show Na^+ release from site 2. We also characterize a possible pathway for K^+ translocation that includes a novel site coordinated by a residue implicated in EAAT countertransport. Furthermore, we show that Na^+ can replace K^+ as the countertransported cation which is consistent with our previously published electrostatic evaluation of EAAT3 identifying a K^+ coordination site that also coordinates Na^+ (Holley and Kavanaugh 2009).

Introduction

Clearance of extracellular glutamate is mediated by excitatory amino acid transporters (EAAT1-5) and is critical to terminate synaptic transmission and preventing potentially toxic over-stimulation of nearby nerve cells (Levy et al., 1998; Pines and Kanner 1990). Transport of glutamate is electrogenic, driven by the co-transport of 3Na^+ and one proton and the countertransport of 1K^+ (Kavanaugh et al., 1997; Levy et al., 1998). Previous studies show that glutamate cannot bind until K^+ is released into the extracellular solution, suggesting a

conformational change that resets the transport cycle after K^+ unbinds (Kavanaugh et al., 1997; Mim et al., 2007).

The first X-ray crystal structure of an homologous archaeal transporter (Glt_{Ph}) revealed an outward-facing homotrimer forming an aqueous bowl penetrating the extracellular side of the plasma membrane (Yernool et al., 2004). The trimer subunits contain eight transmembrane domains (TM1-8) and two α -helical, re-entrant hairpin loops (HP1 and HP2) that are thought to gate transport. Several subsequent Glt_{Ph} structures have been published including a structure with bound inhibitor (DL-threo- β -benzoylaspartate or TBOA) locking HP2 in an open conformation and a structure with aspartate and two thallium ions with HP2 oriented in an occluded (closed) conformation (Boudker et al., 2007). The Tl^+ densities are thought to be surrogates for Na^+ coordination sites in Glt_{Ph} which is supported by the recently published inward-facing Glt_{Ph} structure reporting two Na^+ densities that correlate well with the Tl^+ densities in the outward-facing Glt_{Ph} (Reyes et al. 2009). The inward-facing structure also revealed that each trimer subunit is divided into two structurally rigid domains dubbed the trimerization and transport domains. According to Reyes et al., the trimerization domain anchors the subunit in the membrane, while the transport domain moves approximately 18Å across the membrane to deliver bound substrate. The domains are hinged at the TM2-3 loop and TM5-6 and transport to the cytoplasm unwinds α -helices in TM2, TM3, and TM5 and extends the TM6 α -helix. The anchored trimerization domain consists of transmembranes 1, 2, 4 and 5 and includes the 3-4 loop.

Recently we published an electrostatic evaluation of cation coordination sites in EAAT3 homology models. The evaluation revealed three stably coordinated cation sites within 10Å of the substrate binding site (figure 1). Two of the sites correspond well to the two Tl^+ sites resolved in the thallium-laden Glt_{Ph} crystal structure, while one novel cation site is coordinated by α -carboxyl groups near the bend in HP2 and by the γ -carboxyl group of docked glutamate (Holley and Kavanaugh, 2009; figure 1). Here we expand on our earlier work using computational and physical data to derive a model for sequential binding and release.

Results

Na⁺ cooperatively locks HP2 in an open conformation

Boudker et al. (2007) published crystal structures with HP2 resolved in two conformations; the TBOA-bound open conformation with Tl⁺ bound at site 1 and the aspartate-bound, occluded conformation with Tl⁺ bound at sites 1 and 2. We can infer from these structures only a partial binding order for transport: Na⁺ binds site 1 first, followed by amino acid substrate binding, and HP2 closure allowing Na⁺ to bind site 2 locking HP2 closed. Electrostatic mapping of EAAT3 and Glt_{Ph} models predicts that Na⁺ coordination site 1 is available for cation binding independent of bound amino acid substrate, while site 3 requires coordination by the distal carboxylate of bound substrate (Holley and Kavanaugh, 2009). To address binding order *in vitro* using the electrostatic maps of the EAAT3 models as a guide, we first examined whether substrate distal carboxyl groups contribute to cation coordination.

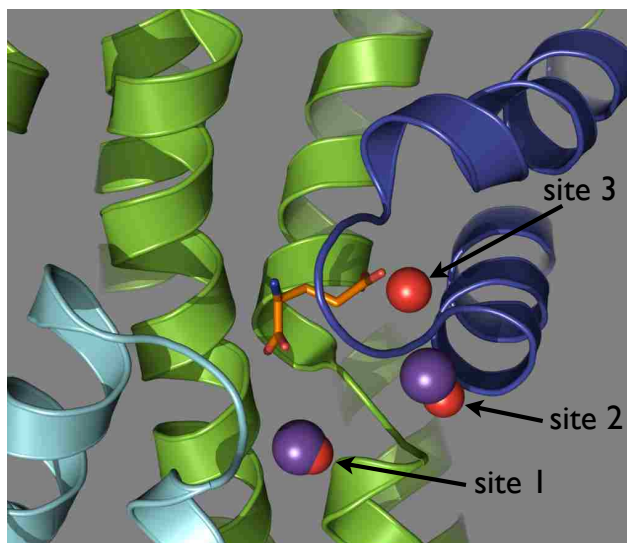


Figure 1. EAAT3 homology model showing thallium binding sites extracted from the Glt_{Ph} X-ray crystal structure (blue) and Na⁺ coordination sites resolved from electrostatic mapping (red). Docked glutamate (orange sticks) is depicted interacting with Na⁺ at site 3.

The γ -carboxyl group of glutamate that contributes to stable coordination of Na⁺ at site 3 also interacts with a highly conserved arginine residue (R447 in EAAT3) that is responsible for recognition of acidic amino acid substrates (Bendahane et al., 2000). We employed the R447C mutant for its unique capacity to transform EAAT3 into a neutral amino acid carrier to determine whether the substrate γ -carboxylate affects sodium cooperativity. Radiolabeled H³-alanine (H³-L-ala) or H³-glutamate (H³-L-glu) uptake in oocytes expressing EAAT3 R447C or

EAAT3 wild type (EAAT3wt) respectively was measured at different Na⁺ concentrations and fit with the Hill equation. We calculated that the EAAT3 R447C mutant has a Hill coefficient (derived from the Hill equation) of approximately $n_{\text{Na}} = 1.0$ for sodium ion cooperativity during transport, suggesting no cooperation between ions (figure 2b). This is in contrast to the Hill coefficient for Na⁺ in EAAT3wt which we calculated to approximately $n_{\text{Na}} = 2.3$, revealing cooperation between at least three sodium ions (figure 2a). These results indicate that R447 contributes to Na⁺ cooperativity during transport, possibly through interactions with the substrate distal carboxylate.

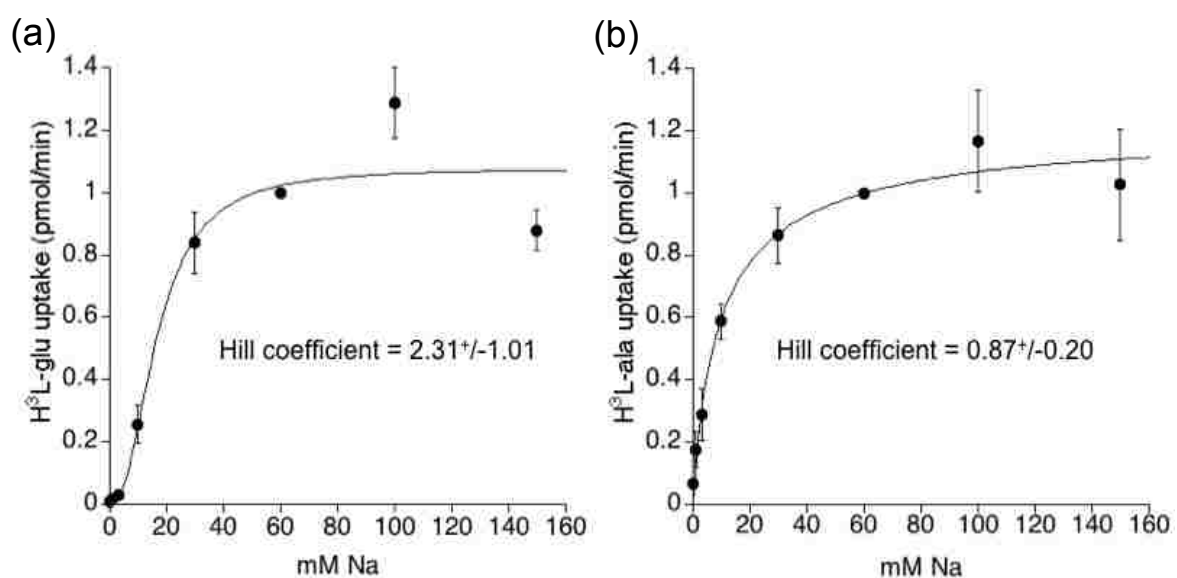


Figure 2. Sodium concentration dependence of tritiated glutamate uptake in EAAT3wt shows cooperation between sodium ions ($n_{\text{hill}} = 2.31$) (a) while the EAAT3 R447C mutant shows no cooperativity ($n_{\text{hill}} = 0.87$) (b). The Hill coefficients were derived from a least-squares fit of the Hill equation.

To quantify the number of sodium ions that bind before glutamate, we used voltage clamp fluorometry to measure steady-state fluorescence intensity changes in oocytes expressing labeled EAAT3 cysteine mutants. The EAAT3 V417C mutation is located near the tip of HP2 and was labeled with Alexa Fluor 488 C₅ maleimide (molecular probes). Voltage clamp measurements and radiolabeled uptake assays indicate that the modification of this cysteine point mutant with a thiol reactive probe allows glutamate binding and activation of the uncoupled anion conductance but prevents substrate transport, locking the transporter half cycle that includes Na⁺ and glutamate binding (data not shown; Seal et al., 2001). Transitioning from choline, which does not interact with the transporter (Wadiche et al., 1995), to Na⁺

changes both the conductance and fluorescence; this small current change is observed also in uninjected oocytes, but the fluorescence change is unique to EAAT3 V417C expressing oocytes and is directly a result of Na⁺ interacting with the transporter. The Hill coefficient derived from a Hill plot of the sodium dependence of fluorescence change from choline was calculated to $n_{Na} = 1.73$ with a $K_m = 39\text{mM}$ (figure 3). These results are consistent with at least two sodium ions binding the glutamate free transporter and cooperatively interacting for HP2 movement.

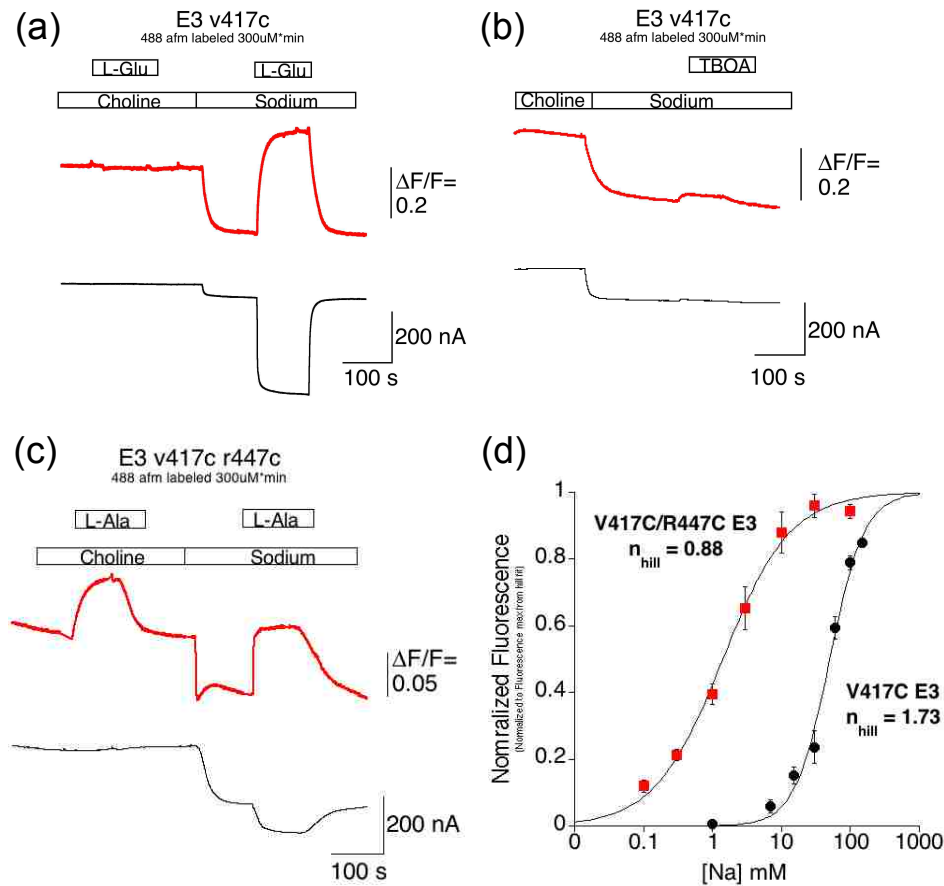


Figure 3. (a)-(c). Simultaneous fluorescence and current recording from oocytes injected with V417C EAAT3 or V417C-R447C EAAT3 and labeled with Alexa Fluor 488 C₅ maleimide (-60 mV). Recordings of Na⁺ alone report quenched fluorescence in all EAAT3 mutants (a)-(c), while co-application of Na⁺ and glutamate for V417C EAAT3 (a) or for Na⁺ and alanine for V417C-R447C EAAT3 (c) report increased fluorescence. Co-application of Na⁺ and TBOA report an intensity change similar to that of Na⁺ alone. (d). The Na⁺ dependence of the fluorescence intensity for V417C EAAT3 vanishes in V417C-R447C EAAT3 when the solution was changed from choline to the respective Na⁺ concentrations. Both curves fit well to the hill equation (V417C, $K_m = 39\text{ mM}$, $n_{hill} = 1.8$; V417C-R447C, $K_m = 1.4\text{ mM}$, $n_{hill} = 0.88$).

To corroborate the fluorometry data with the electrostatic mapping and uptake data, we designed the EAAT3 V417C R447C double mutant. Our results show that in the absence of

amino acid substrate sodium quenched fluorescence intensity and transitioning from choline to Na⁺ revealed no cooperativity associated with HP2 movement between sodium ions ($n_{Na} = 0.88$, figure 3D). This demonstrates that the R447C mutation disrupts cooperativity for HP2 movement in the substrate *free* transporter. These results conflict with the interpretation that sodium cooperativity during uptake in EAAT3 R447C (figure 2) is disrupted because H³-alanine does not have a contributing distal carboxyl group to contribute to site 3 Na⁺ coordination. However, because the fluorometry measures HP2 movement and not transport, we sought to clarify whether the fluorescence changes represent HP2 movement consistent with early transport conformations. We measured fluorescence intensity changes in EAAT3 V417C with sodium transitioning into a co-application of sodium and glutamate and found that sodium alters the change in fluorescence differently than glutamate and sodium together (figure 3a and 3C). This indicates that the measured HP2 movement associated with sodium alone differs from movement that precedes transport and could reflect the HP2 open state or an otherwise uncharacterized intermediate state.

To test whether the fluorescence changes associated with sodium alone are consistent with the HP2 open state, we again used EAAT3 V417C to measure fluorescence intensity changes associated with TBOA in a background of sodium. Our results report only a very slight fluorescence change transitioning from sodium alone to a co-application of sodium with a saturating concentration of TBOA (figure 3b) indicating that sodium orients HP2 into a conformation similar to the TBOA-bound state.

Li⁺ binding occurs after glutamate binds and is sensitive to HP2 orientations

Previous studies show that Li⁺ can replace Na⁺ and support transport in EAAT3 but not in EAAT2 (Grunewald and Kanner, 1995; Zhang and Kanner, 1999; Menaker et al., 2006; Huang et al., 2009). We combined electrostatic mapping with short molecular dynamics simulations of EAAT2 to determine Li⁺ sensitivity to subtle HP2 movements. The equation used to calculate partial valences for each metal ion-oxygen pair is $v = (R_i/R_0)^{-N}$ where R is the distance of an oxygen atom to the cation, R₁ is the distance given valence ($v = 1.0$), and N is an empirically derived exponent specific to each cation (Nayal and Di Cera, 1994; Nayal and Di Cera, 1996). A plot of this equation using the ion-specific values for Na⁺ and Li⁺ indicates that the bond strength for sodium-oxygen pairs is approximately twice that of Li⁺ for any given distance

(figure 4a). Electrostatic mapping of EAAT2 structures derived from short molecular dynamics simulations demonstrate that even slight movement in HP2 (an r.m.s.d. of 1.7Ås as measured from distances moved between coordinating oxygens in HP2 and TM7; figure 4b) can dramatically reduce cation coordination at site 2. Significantly, Li⁺ is more sensitive to HP2 perturbations than Na⁺ with a valence calculation of $v^{\text{Li}} = 0.66$ and $v^{\text{Na}} = 0.84$ (figure 4c). Lithium's greater sensitivity to HP2 movements supports the proposition that sequence differences unique to EAAT2 HP2 allow an alternative HP2 closed conformation that cannot sustain site 2 Li⁺ coordination (Huang et al., 2009).

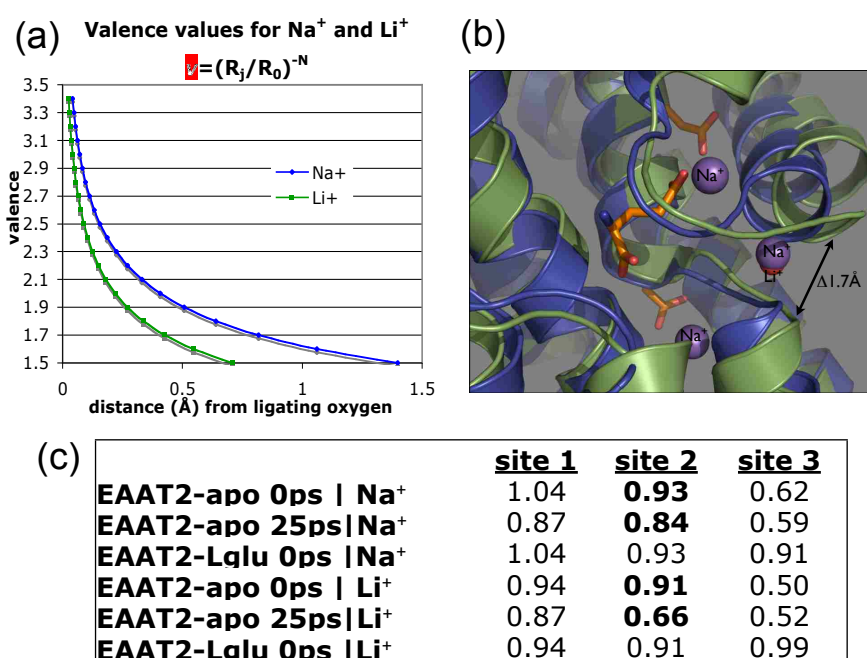


Figure 4. (a) A plot of distance dependence of valence calculations for Na⁺ and Li⁺ using the VALE algorithm shows that the bond strength between Li⁺ and a ligating oxygen at any given distance is half the strength of that of Na⁺. (b) Short molecular dynamics simulations of an EAAT2 homology model (blue ribbon) show similar placement of Li⁺ at site 2 (red sphere) relative to Na⁺ (blue spheres). (c) Electrostatic mapping of the EAAT2 homology model before molecular dynamics simulations and after a 25ps simulation show that movement in HP2 destabilizes Li⁺ coordination at site 2. The simulated movement of HP2 decreases the models capacity to coordinate Na⁺ by 10% and Li⁺ by 27%.

We applied glutamate in the presence of lithium to oocytes expressing EAAT2 to determine the Na⁺ selective site and found that glutamate did not induce steady-state transport currents (data not shown), but did block a transient capacitive current (Figure 5a, inset; Wadiche and Kavanaugh, unpublished observations). The block of the capacitive current was similar to the one blocked by the non-transportable inhibitor kainate in the presence of extracellular sodium (Figure 5a; Wadiche et al., 1995). The lithium transient current-voltage

plot obeyed a Boltzmann function with identical slope as sodium, but shifted towards hyperpolarized potentials, suggesting that Li^+ occupied the same or similar binding sites as Na^+ but with lower affinity (Figure 5b; Larsson et al., 2004). The ability of glutamate to block transient capacitive currents when Li^+ is the extracellular cation provides further evidence that the Na^+ selective site in EAAT2 binds after glutamate is bound, eliminating site 1 as a possible candidate for EAAT2 Na^+ selectivity. Integrating these data with the molecular dynamics simulations and valve data presented above suggests cation binding site 2 as the most likely candidate for Na^+ selectivity in EAAT2.

Two K^+ binding sites

The K^+ ion-binding site in EAAT3 is thought to involve E374 (Kavanaugh et al., 1997) which is approximately 9Ås from site 4 and within the valence shell of site 5 (figure 6a). We propose that these sites are at the tail end of a pathway for K^+ countertransport. As previously reported, the overlap of site 4 with the substrate binding region as well as its high valence value (figure 6b; Holley and Kavanaugh 2009) could explain constraints in the K^+ bound form

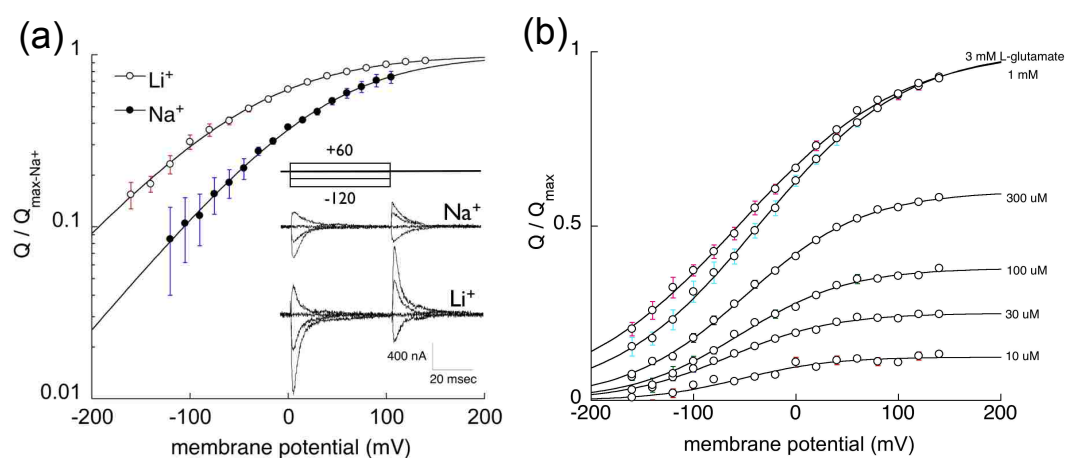


Figure 5. Voltage-dependent interaction of lithium with hEAAT2. (a) Subtraction of current-voltage records obtained in 100 mM lithium from records during 3 mM L-glutamate co-application in EAAT2-expressing oocytes reveals a transient current that decays completely with a time constant of 3.0 ± 0.2 msec for command pulses from a holding potential of +60 mV to 0 mV, ($n = 6$; inset). In sodium, the transient current blocked by 300 μM kainate decays with a time constant of 7.0 ± 0.6 msec ($n = 6$; inset). The voltage-dependencies of the charge movements blocked by these saturating agonist concentrations in sodium and lithium were fit to the Boltzmann function. In EAAT2-expressing oocytes, the lithium transient current blocked by a saturating concentration of glutamate (3 mM) was compared to the sodium transient current blocked by a saturating concentration of kainate (300 μM). Both currents were measured over a range of membrane potentials, and their voltage-dependencies were fit to a Boltzmann function. (b) The integrated charge blocked in EAAT2 by increasing concentrations of L-glutamate was fit to a Boltzmann function.

that permit glutamate exclusion during the countertransport hemi-cycle (Grunewald and Kanner, 1995; Mim et al., 2007). Valence mapping shows that when EAAT3 is mutated *in silico* from a glutamate at position 374 to aspartate, coordination of K⁺ is reduced at site 5 (figure 6b) from $v = 1.05$ in EAAT3wt to $v = 0.73$ in EAAT3 E374D. This agrees with the findings of Kavanaugh et al. (1997) that show that mutation corresponding to EAAT3 E374D cannot countertransport K⁺. Electrostatic mapping of the outward-facing, HP2 closed EAAT3 model indicate both site 4 and site 5 coordinate K⁺ more stably than Na⁺ (figure 6b). However the high valence calculations for Na⁺ at site 4 of the HP2 closed/apo form ($v^{\text{Na}} = 0.97$) indicate that K⁺ binding sites are capable of Na⁺ coordination. Experimental results from patch clamps drawn from oocytes expressing EAAT3 show the recovery kinetics of peak anion currents for intracellular Na⁺ and K⁺ (figure 7), demonstrating that sodium can function as the countertransported cation. This supports the promiscuity predicted by the valence calculations for site 4. Valence calculations also indicate that the inward-facing EAAT3 model cannot coordinate K⁺ at site 5, possibly due to increased constraints on HP2. This suggests that K⁺ binding is ordered starting with site 4 and moving to site 5 in the outward-facing conformation.

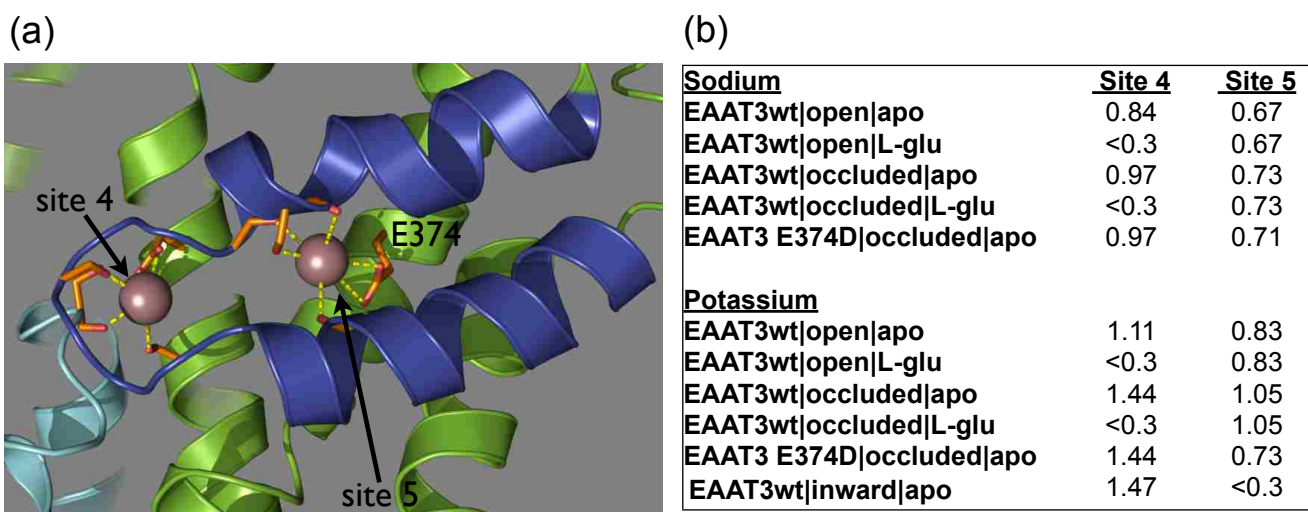


Figure 6. (a) Electrostatic mapping of the HP2-loop closed form of EAAT3 predicts that the valence shell for K⁺ coordination at site 5 includes glutamate (L-glu) at position 374. (b) Valence calculations of EAAT3 models show stable coordination of both Na⁺ and K⁺ at site 4 in the occluded (HP2 loop closed) apo model and stable coordination of K⁺ at site 5 also in the occluded form. Calculated electrostatic coordination capacity for K⁺ at site 5 in the EAAT3 E374D mutant is reduced relative to wild type EAAT3 ($v_{\text{wt}} = 1.05$ versus $v_{\text{E374D}} = 0.73$).

The transport and trimerization domains of Glt_{Ph} remain rigid during transport with a 0.6Å r.m.s.d. when the inward-facing domains are superimposed onto their respective outward-facing domains. Electrostatic mapping of inward-facing EAAT3 and Glt_{Ph} models nevertheless

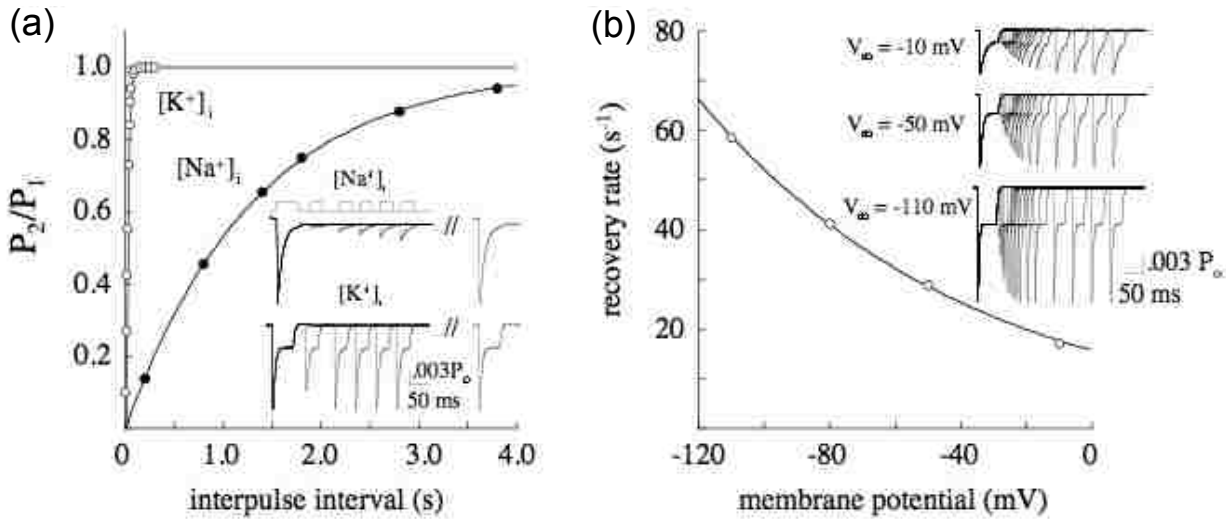


Figure 7. (a) Recovery kinetics of EAAT3 in outside-out patches in response to paired glutamate pulses (10 mM) with K⁺ or Na⁺ in the (intracellular) pipette. This result is consistent with the predicted K⁺/Na⁺ selectivity of hypothetical ion binding site 4 (Holley and Kavanaugh, 2009). The time constant for the recovery was obtained by fitting the data with a first order exponential (Na⁺: $\tau = 1.3 \pm 0.08$ sec; n=6; K⁺: $\tau = 24 \pm 3$ ms; n=15). Inset, peak transport current recovery with either intracellular Na⁺ or K⁺ ions using the same protocol (50 ms conditioning pulse followed by a 30 ms test pulse). (b) Recovery kinetics for outside-out patches in response to the paired glutamate pulses with Na⁺ in the (intracellular) pipette is also voltage dependent.

reveal decreased coordination for Na⁺ at sites 2 and 3 (table 3) compared to the outward-facing, occluded (HP2 closed) conformation. We used a series of molecular dynamics simulations of lipid-embedded Glt_{PH} systems to determine if this reduced coordination translates to a possible mechanism for release. Shrivastava et al. (2008) reported that short simulations (10ns) of the aspartate free, outward-facing Glt_{PH} system exhibit HP2 movement

	<u>Site 1</u>	<u>site 2</u>	<u>site 3</u>
Sodium			
EAAT3 open apo	0.80	<0.3	0.72
EAAT3 open L-glu	0.80	<0.3	0.72
EAAT3 occluded apo	1.04	0.93	0.62
EAAT3 occluded L-glu	1.04	0.93	0.91
EAAT3 inward L-glu	1.03	0.75	<0.3
Glt _{PH} inward L-asp	1.03	0.75	<0.3

Table 1. Electrostatic mapping of EAAT3 and Glt_{PH} structures show decreased coordination of Na⁺ at sites 2 and 3 in the inward-facing structure compared to their respective sites in the outward-facing, occluded (HP2 loop closed) conformation.

from the closed state to a more open conformation. Here we show Na⁺ positioned at site 2 is stably coordinated with an average r.m.s.d of 0.8Å during simulations of the outward-facing Glt_{PH} system. As predicted by Boudker et al. (2007), simulations that include Na⁺ bound at site 2 show no HP2 movement indicating that site 2 locks HP2 in the closed state (figure 9). Na⁺ positioned at site 3 is less stable with an r.m.s.d. of 1.3Å. Site 3 mobility is coordinated by the

distal carboxyl group of bound aspartate which disassociates from R447 interactions after associating more closely with the site 3 Na⁺ (figure 8).

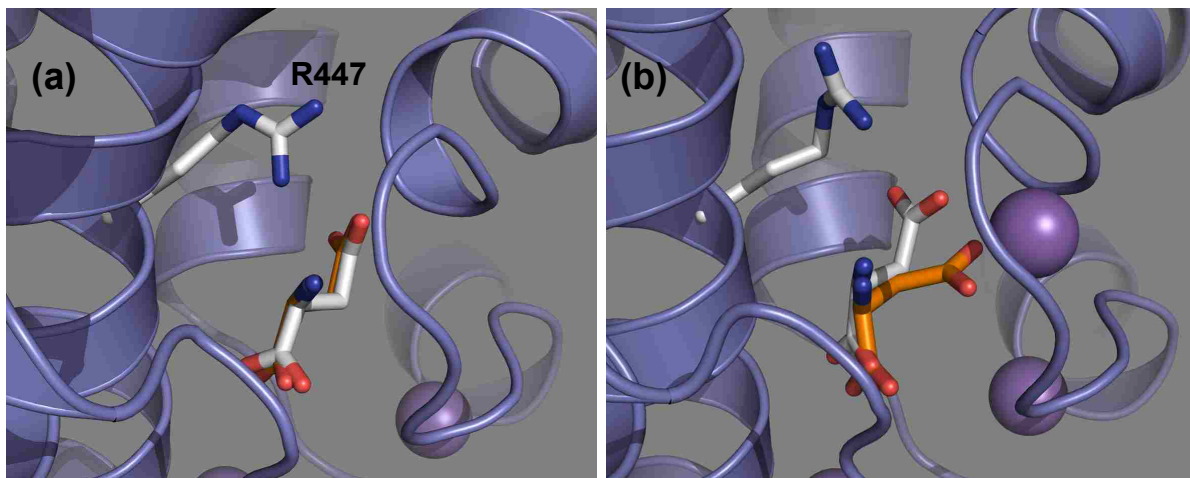


Figure 8. Molecular dynamics simulations of Glt_{Ph} (5ns) show aspartate mobility when site 3 Na⁺ is included. White sticks represent the initial time-point of the simulation and orange sticks indicate the position after the 5ns simulation.

Simulations of the aspartate bound inward-facing Glt_{Ph} system exhibit very similar Na⁺ site 3 mobility. More interesting however is that three trimer subunits during two simulations (10ns each) of the inward-facing system show release or partial release of Na⁺ bound at site 2 (figure 10). This agrees well with the electrostatic mapping of EAAT3 and Glt_{Ph} models as well as electrophysical evidence reporting that in EAAT3 at least one Na⁺ must unbind before glutamate dissociates into the cytoplasm (Otis and Jahr 1998) and suggests site 2 locks HP2 closed in the outward-facing conformation but is rapidly destabilized in the inward-facing conformation allowing for release.

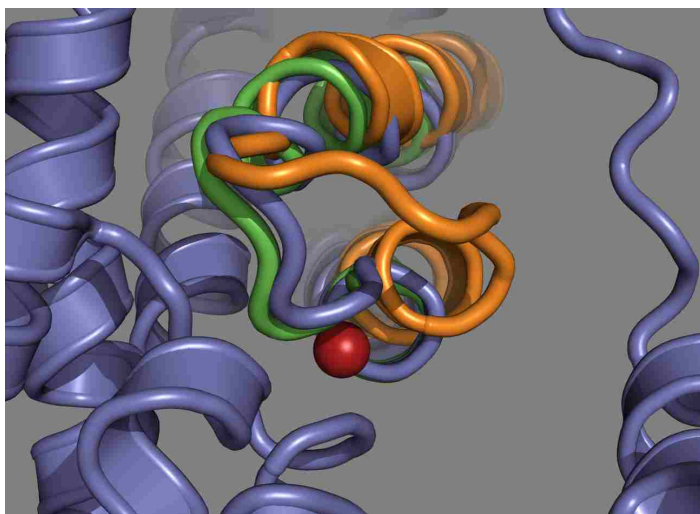


Figure 9. HP2 movement during a 10ns simulation in Glt_{Ph} is stabilized by Na⁺ at site 2. The blue ribbon represents the initial structure. The green ribbon shows HP2 movement after the 10ns simulation with Na⁺ bound at site 2 while the orange ribbon show HP2 movement when site 2 is vacant.

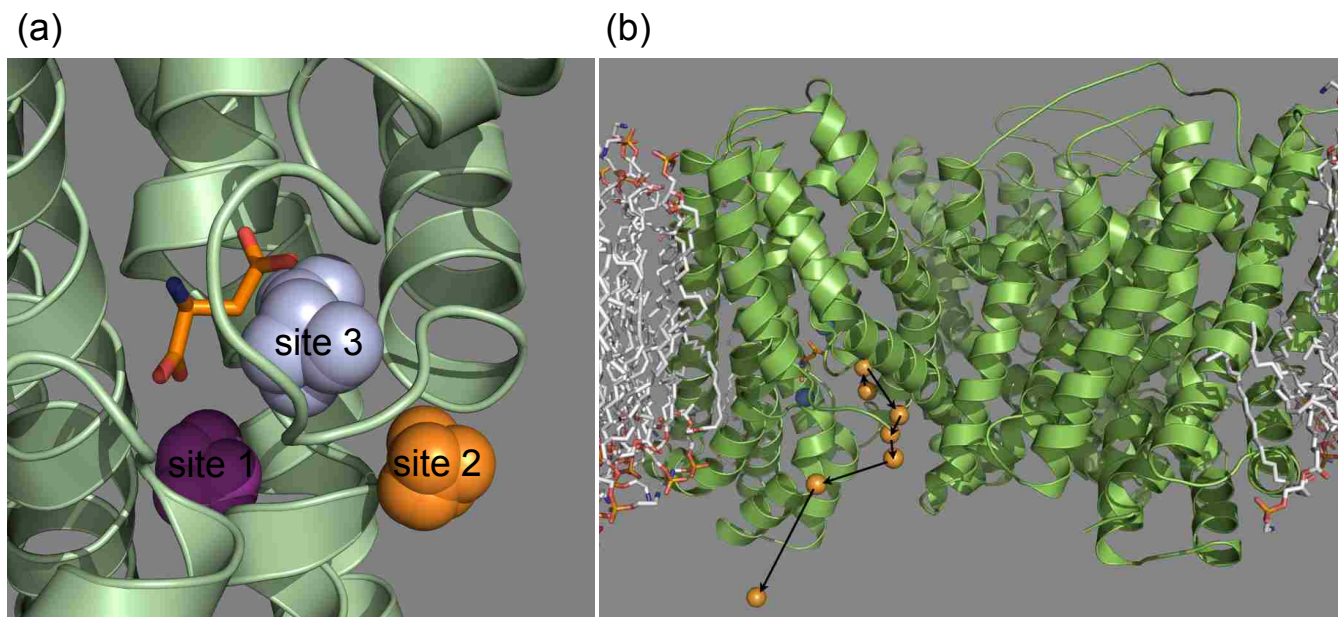


Figure 10. Molecular dynamics simulations of the lipid embedded Glt_{Ph} system. (a) 10ns simulation of the outward-facing Glt_{Ph} system shows coordination of Na⁺ at sites 1 (purple), 2 (orange), and 3 (gray). Bound aspartate (orange sticks) shown coordinating site 3 is from the earliest time-point of the simulation. (b) Example of a release pathway into the cytoplasm of Na⁺ initially bound at site 2 (orange ball) during a 10ns molecular dynamics simulation of the lipid embedded, inward-facing Glt_{Ph} system.

Discussion

We probe cation and substrate interactions with glutamate transporters to construct a partial model for sequential binding and unbinding (figure 11). We contend that substrate translocation requires first that Na⁺ bind site 1 and that Na⁺ cooperatively interacts with the transporter to lock HP2 into the open conformation. This is followed by glutamate binding and subsequent HP2 closure allowing coordination of Na⁺ at site 2 to lock HP2 in the occluded position. Site 3 is coordinated by α-carboxyl groups in HP2 and the distal carboxylate of bound substrate, suggesting that Na⁺ binds site 3 only after site 2 Na⁺ has stabilized HP2 in the occluded position. Molecular dynamics simulations of the lipid-embedded Glt_{Ph} homologue show that the bond formed between the site 3 Na⁺ and bound substrate destabilizes the R447 interactions with the substrate distal carboxylate permitting greater movement of bound substrate relative to simulations with no site 3 Na⁺ (figure 8). Furthermore, electrostatic mapping of the outward and inward-facing EAAT3 models indicate that the inward-facing conformation is less capable of coordinating Na⁺ at site 2 (table 1). This agrees well with

molecular dynamics simulations of the inward-facing Glt_{Ph} system showing rapid release (within 10ns) of Na⁺ from site 2 (figure 10b).

To determine whether Na⁺ bound at site 3 plays a role in coupled transport we employed the EAAT3 R447C mutant which transforms EAAT3 into a neutral amino acid obligate exchanger. Consistent with our model for functional coordination of Na⁺ at site 3, we found that by removing the possibility for Na⁺ coordination from the substrate distal carboxylate we eliminated cooperativity between sodium ions for transport (figure 2). Complementary voltage clamp fluorometry experiments indicate that at least two sodium ions cooperate for HP2 movement and that this cooperativity is extinguished in the R447C mutant. The cooperativity determined from fluorometry is measured in the absence of amino acid substrate, suggesting that either the change in cooperativity measured by fluorometry reflects the same change measured from the uptake assays and a functional mechanism for cooperativity would not involve coordination of Na⁺ at site 3, or that the fluorometry data measures sodium cooperativity for HP2 movement not transport and the measurements pertain to one or more as yet uncharacterized Na⁺ binding sites

To distinguish between these possibilities we again used oocytes expressing labeled EAAT3 V417C to determine whether fluorescence changes associated with sodium application are consistent with changes associated with sodium combined with glutamate. Our results demonstrate that transitioning from choline to sodium *quenches* fluorescence while transitioning into glutamate *enhances* fluorescence (figure 3a). To further probe the sodium-induced conformational state of HP2 using EAAT3 V417C we transitioned from choline to sodium alone to a co-application of sodium and TBOA resulting in little measured change in fluorescence (figure 3b). Although fluorometry measurements do not necessarily measure conformational movement, a simple interpretation of the fluorescence traces in figure 3 is that sodium causes HP2 to orient into an open conformation similar to that of TBOA-bound crystal structure, while glutamate induces the closed, occluded conformation. This agrees very well with a substrate depleted Glt_{Ph} structure, which Boudker et al. (2007) described as “essentially indistinguishable” from the TBOA-bound Glt_{Ph} structure.

These data suggest different positions of HP2 correlate to different steps during early binding and transport and could indicate that sodium cooperativity for HP2 movement does not reflect sodium cooperativity for transport. That is, the Hill coefficients derived from sodium

cooperativity for radiolabeled amino acid uptake in EAAT3wt and EAAT3 R447C (figure 2) directly relates to substrate translocation and the potential implications for cooperativity involving Na⁺ bound at site 3 are not necessarily undermined by the fluorometry data. A possible explanation involves a 41 amino acid deletion in TM4 of Glt_{Ph} relative to EAAT3. This deletion is very near to the portion of the 3-4 loop that interacts with HP2 in the TBOA-bound, open conformation (Boudker et al., 2007). Koch et al. (2007) demonstrate that fluorescently labeled cysteine mutations within this region report fluorescence changes in response to different concentrations of Na⁺ in the absence of glutamate. The authors argue that these Na⁺ dependent changes could be due to HP2 movement influenced by as yet unidentified Na⁺ binding sites within the TM4 deletion. The inward-facing Glt_{Ph} transport domain as described by Reyes et al. (2009) does not involve TM4 or the 3-4 loop and does require HP2 to be in the closed conformation. Excepting uncharacterized allosteric sites or TM4 interactions with the marginal availability of site 3 in the HP2 open conformation (table 1), Na⁺ sites involving the TM4 deletion would likely not be involved in transport and Na⁺ cooperativity for HP2 movement can reasonably be considered separate from translocated Na⁺ ions.

Unlike all other EAAT subtypes, Li⁺ cannot support transport in EAAT2. Consistent with previously published studies we show that EAAT2 is sensitive to Li⁺ only after amino acid substrate binding (figure 4; Zhang and Kanner 1999; Huang et al., 2009). To determine a likely candidate for the EAAT2 sodium selective (lithium sensitive) site we used short molecular dynamics simulations of a lipid embedded EAAT2 system in conjunction with electrostatic mapping. Our results demonstrate that Li⁺ coordination at site 2 is susceptible to slight HP2 movements (figure 4) suggesting that a small alteration of HP2 positioning in the occluded form of the transporter would affect cation binding. This is consistent with Huang et al. (2009) who implicated site 2 as the EAAT2 sodium selective site and who originally postulated that sodium selectivity could derive from a slightly altered HP2 occluded conformation. These results help define a possible mechanism for specificity during transport and may have implications for other subtype specificities such as the high affinity of EAAT2 for kainate.

Previously we used electrostatic mapping to determine a K⁺ coordination site that overlaps the amino acid binding site and has a high affinity for Na⁺ (Holley and Kavanaugh 2009). Here we expand this model to include a second K⁺ site (site 5, figure 6a) that directly interacts with EAAT3 E374 which is thought to be involved in K⁺ countertransport. Compatible

with Kavanaugh et al. (1997) who showed that K^+ countertransport was disrupted when a residue analogous to E374 was mutated to an aspartate, valence calculations indicate reduced K^+ coordination at site 5 for the EAAT3 E374D mutant (figure 6b). Also in agreement with our earlier findings indicating high Na^+ affinity at site 4, we show Na^+ can replace K^+ as the countertransported cation (figure 7a).

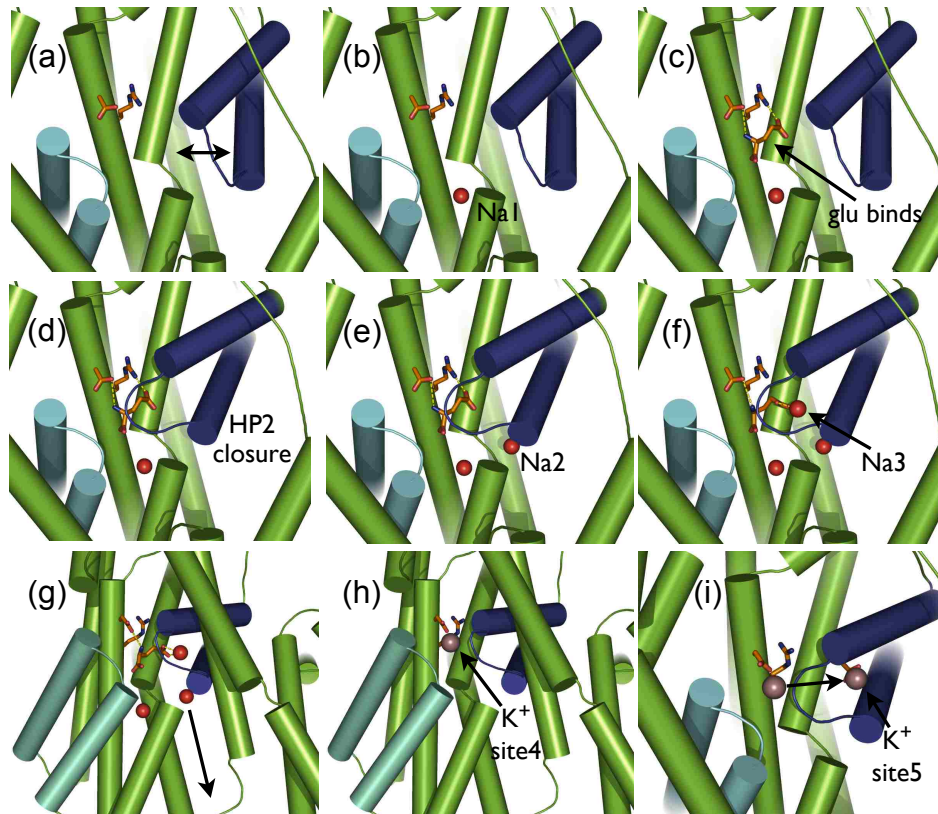


Figure 11. Overview of the proposed transport model with H^+ and anion conductance omitted. (a) In the absence of sodium, HP2 moves freely, possibly sampling positions between the open and closed conformations reported by Boudker et al. in 2007. Addition of sodium allows Na^+ ions to bind two sites (possibly including site 1) that cooperatively prop HP2 in a conformation similar to the open conformation. Concurrently, Na^+ binds site 1 (b) and then substrate binding (c). Subsequent HP2 closure (d) introduces site 2 availability for Na^+ coordination (e) which locks HP2 in the occluded conformation and allows Na^+ to bind site 3 (f). Interaction of site 3 Na^+ with substrate distal carboxylate destabilizes the bond between R447 and substrate (f) allowing for a possible initial mechanism of release in the inward-facing transporter conformation. After translocation of the Na^+ -glutamate complexed transport domain to the inward-facing conformation, Na^+ at site 2 is released. Substrate and Na^+ at sites 1 and 3 are released through an unknown mechanism. K^+ then binds site 4 interacting with D444. After translocation to the outward-facing orientation, K^+ moves from site 4 to site 5 and interacts with E374 (i).

Experimental Procedures

Homology modeling

Human EAAT3 sequence (obtained from GenBank, <http://www.ncbi.nlm.nih.gov>) and was aligned with the Protein Data Bank (PDB) sequences for the Gl_{TPh} archaeal homologue (2NWX, 2NWW and 3KBC) according to alignments published by Yernool et al. (2004). Homology models were built by threading the aligned EAAT2 and EAAT3 sequences along the Gl_{TPh} PDB coordinates using the SwissProt server (<http://swissmodel.expasy.org//SWISS-MODEL.html>). The resulting models were optimized through local energy minimizations of regions with high steric and electrostatic interference using the AMBER7 force field in the Tripos SYBYL8.0 platform.

Electrostatic mapping

Valence shell mapping and calculations were performed as described previously (Nayal and Di Cera, 1994; Nayal and Di Cera, 1996; Holley and Kavanaugh, 2009). Briefly, we mapped homology and X-ray crystal structure models using the VALE software program (courtesy of Enrico Di Cera and Thierry Rose; Washington University, St. Louis, MO) with a 3.4Å probe radius and a grid size of 0.1Å within 10Ås from the aspartate α -carbon imported from the 2NWX or the 3KBC crystal structure. In order to reduce noise, no water molecules were included in the valence mapping (Nayal and Di Cera, 1994). Consistent with recent studies, we chose a valence cutoff of $v \geq 0.9$ for likely candidate binding sites (Ogawa and Toyoshima, 2002; Rakowski and Sagar, 2003; Nayal and Di Cera, 1996). The three-dimensional coordinates of valence maps that contain multiple, clustered valence sites within a 2Å radius were included as a single site and we reported the highest estimated valence within each site. Root mean square deviation (r.m.s.d.) calculations were measured using the Visual Molecular Dynamics program (VMD, www.ks.uiuc.edu/Research/vmd/).

Molecular dynamics

We developed the simulation system by embedding the trimeric Gl_{TPh} crystal structure (Yernool et al., 2004; Ryan et al., 2010; Protein Data Bank accession codes 1XFH and 3KBC respectively) or the trimeric EAAT2 homology model in a POPE membrane using the VMD Membrane builder and solvating the system with explicit, all-atom TIP3P water molecules using VMD Solvate (Darden et al., 1993). This resulted in a system sizes of 150 X 150 X 77 Å³

with approximately 130,000 atoms for each simulation system. We added Na⁺ and Cl⁻ to a concentration of 200mM to neutralize the total charge of the system. Ions were added either randomly using VMD or were manually placed within coordination sites determined by electrostatic mapping (Holley and Kavanaugh, 2009).

All simulations were performed using NAMD 2.7 (Phillips et al., 2005) with a 1fs time step under periodic boundary conditions using the CHARMM27 forcefield (Mackerell et al., 1998). The system was equilibrated by first melting only lipids in a 300ps simulation at constant volume and constant temperature (NVT) at 303K using Langevin dynamics with a damping coefficient of 5ps⁻¹ to maintain constant temperature. A subsequent 500ps simulation was performed at constant pressure (1 atm) and constant temperature (303K) with molten solvent and lipids and fixed protein to ensure proper lipid packing. The full system was then equilibrated for another 500ps in the NPT ensemble with a constant pressure of 1 atm. Production runs were performed at 303K and 1 atm with non-bonded interactions cutoff at a distance of 12Å. Long-range electrostatic interactions were calculated using the particle mesh Ewald method (Darden et al., 1993).

Uptake-flux measurements

The human EAAT3 wild type and EAAT3 R447C cDNA subcloned into the PI28 oocyte expression vector were transcribed to cRNA using mMessage mMachine (Ambion). Approximately 50nL of the cRNA were injected into stage V-VI *Xenopus laevis* oocytes and radiolabeled uptake was assayed 3-5 days post injection as previously described by Zerangue and Kavanaugh (1996).

Expression and Voltage Clamp Fluorometry with *Xenopus laevis* oocytes

Cysteine point mutagenesis of V417C and V417C-R447C was performed with QuikChange Site-Directed Mutagenesis Kit (Stratagene). cRNA was microinjected in stage V-VI *Xenopus laevis* oocytes. EAAT3 mutant transporters were labeled with Alexa Fluor 488 C₅ maleimide (Molecular probes, A-10254). Alexa Fluor 488 C₅ maleimide was dissolved in DMSO at 10 mM and frozen in aliquots. Labeling was done with 10 μM dye in standard recording solutions for 30 minutes (saturation as determined by a labeling curve). Currents and fluorescence were recorded 3-5 days later as previously described (Larsson et al., 2004; Wadiche et al., 1995). Recording solution contained 96mM NaCl, 2mM KCl, 1mM MgCl₂, 1.8mM CaCl₂, and 5mM HEPES (pH7.4). In choline replacement experiments, 96mM choline

chloride was used for the NaCl. Microelectrodes were filled with 3M KCl and had resistances from 1 to 3 MΩ. Two electrode voltage clamp recordings were performed at 22°-25°C with a Geneclamp 500 interfaced to an IBM-compatible PC using a Digidata 1320 A/D controlled with the pCLAMP 6.0 program suite (Molecular Devices). The currents were low-pass filtered at 1 kHz and digitized at 5 kHz. Data were analyzed offline; modeling and fitting of substrate concentration-dependence of the currents was performed with Kaleidagraph software (v 4.04).

Electrophysiological recording

Recording solutions contained 100 mM NaCl, 1.8 mM CaCl₂, 1 mM MgCl₂, and 5 mM HEPES-Tris, pH 7.5. In experiments where sodium was varied or replaced, equimolar cation substitution with either lithium or choline was employed. Two-microelectrode voltage-clamp recording was performed with a Gene Clamp 500 amplifier interfaced to an IBM compatible PC-AT using a Digidata 1200 A/D controlled using the pCLAMP program suite (version 6.0.3; Axon Instruments, Foster City, CA). A MacLab/2e analog/digital converter (ADInstruments, Mountain View, CA) was used to generate continuous current records. Microelectrodes were filled with 3 M KCl solution and had resistances of less than 1.5 MΩ. For pre-steady-state current measurements, data were sampled at the lowest gain to avoid saturation of the amplifier response during the peak of the capacitance transient and signal-averaged 8 times before and after solution exchange. Currents were digitized at 1 kHz. The normalized mean concentration response of currents induced by L-glutamate was fitted by least squares to the Michaelis-Menten equation

$$I = I_{\max} [\text{Glu}] / ([\text{Glu}] + K_m)$$

K_m values are expressed as mean ± S.E. from fits to data from individual oocytes. The cation concentration dependence of response currents induced by L-glutamate was fitted by least squares to the Hill equation

$$I = I_{\max} [\text{Na}^+]^n / ([\text{Na}^+]^n + K_m^n)$$

where n is the cooperativity index. Transient currents were obtained by subtraction of current traces recorded in the presence of kainate (sodium) or glutamate (lithium) from control traces. For each oocyte, the capacitive charge movements were calculated by time integration of the subtracted current records using Clampfit 6.0. They were then plotted versus voltage and fitted to the Boltzmann function

$$Q_{\text{tot}} = 1 + \exp[e_0 z \delta (V_m - V_{0.5}) / kT] + Q_{\text{offset}}$$

where Q_{tot} is the total charge movement, $V_{0.5}$ is the midpoint of the charge movement, V_m is the membrane potential, $z\delta$ is the product of the valence of the charge and apparent fraction of the membrane electric field sensed by that charge, Q_{offset} is the offset that depended on the holding potential, e_0 is the fundamental charge, k is the Boltzmann constant, and T is the absolute temperature. For comparisons among oocytes, charge movements were offset vertically by Q_{offset} and normalized to the Q_{tot} in the same oocytes.

References

- Bendahan A, Armon A, Madani N, Kavanaugh MP, Kanner BI (2000) Arginine 447 plays a pivotal role in substrate interactions in a neuronal glutamate transporter. *J Biol Chem* 275:37436-37442.
- Borre L, Kanner BI (2001) Coupled, but not uncoupled, fluxes in a neuronal glutamate transporter can be activated by lithium ions. *J Biol Chem* 276:40396-40401.
- Borre L, Kavanaugh MP, Kanner BI (2002) Dynamic equilibrium between coupled and uncoupled modes of a neuronal glutamate transporter. *J Biol Chem* 277:13501-13507.
- Boudker O, Ryan RM, Yernool D, Shimamoto K, Gouaux E (2007) Coupling substrate and ion binding to extracellular gate of a sodium-dependent aspartate transporter. *Nature* 445:387-393.
- Darden TA, Pedersen LG (1993) Molecular modeling: an experimental tool. *Environ Health Perspect* 101:410-412.
- Grunewald M, Kanner B (1995) Conformational changes monitored on the glutamate transporter GLT-1 indicate the existence of two neurotransmitter-bound states. *J Biol Chem* 270:17017-17024.
- Holley DC, Kavanaugh MP (2009) Interactions of alkali cations with glutamate transporters. *Philos Trans R Soc Lond B Biol Sci* 364:155-161.
- Kavanaugh MP, Bendahan A, Zerangue N, Zhang Y, Kanner BI (1997) Mutation of an amino acid residue influencing potassium coupling in the glutamate transporter GLT-1 induces obligate exchange. *J Biol Chem* 272:1703-1708.
- Koch HP, Hubbard JM, Larsson H (2007) Voltage-independent Sodium-binding Events Reported by the 4B-4C Loop in the Human Glutamate Transporter Excitatory Amino Acid Transporter 3. *J. Biol. Chem.* 282:24547-24553.
- Larsson, HP, Tzingounis AV, et al. (2004) Fluorometric measurements of conformational changes in glutamate transporters. *Proc Natl Acad Sci U S A* 101: 3951–3956
- Levy LM, Warr O, Attwell D (1998) Stoichiometry of the glial glutamate transporter GLT-1 expressed inducibly in a Chinese hamster ovary cell line selected for low endogenous Na⁺-dependent glutamate uptake. *J Neurosci* 18:9620-9628.
- MacKerell AD, Bashford D, Bellott, Dunbrack RL, Evanseck JD, Field MJ, Fischer S, Gao J, Guo H, Ha S, Joseph-McCarthy D, Kuchnir L, Kuczera K, Lau FTK, Mattos C, Michnick S, Ngo T, Nguyen DT, Prodhom B, Reiher WE, Roux B, Schlenkrich M, Smith JC, Stote R, Straub J, Watanabe M, Wiorkiewicz-Kuczera J, Yin D, Karplus M (1998) All-Atom

- Empirical Potential for Molecular Modeling and Dynamics Studies of Proteins. *The Journal of Physical Chemistry B* 102:3586-3616.
- Menaker D, Bendahan A, Kanner BI (2006) The substrate specificity of a neuronal glutamate transporter is determined by the nature of the coupling ion. *J Neurochem* 99:20-28.
- Mim C, Tao Z, Grewer C (2007) Two conformational changes are associated with glutamate translocation by the glutamate transporter EAAC1. *Biochemistry* 46:9007-9018.
- Nayal M, Di Cera E (1994) Predicting Ca²⁺-binding sites in proteins. *Proc Natl Acad Sci USA* 91:817-21.
- Nayal M, Di Cera E (1996) Valence screening of water in protein crystals reveals potential Na⁺ binding sites. *J Mol Biol* 256:228-34.
- Otis TS, Jahr CE (1998) Anion currents and predicted glutamate flux through a neuronal glutamate transporter. *J Neurosci* 18:7099-7110.
- Phillips JC, Braun R, Wang W, Gumbart J, Tajkhorshid E, Villa E, Chipot C, Skeel RD, Kale L, Schulten K (2005) Scalable molecular dynamics with NAMD. *J Comput Chem* 26:1781-1802.
- Pines G, Kanner BI (1990) Counterflow of L-glutamate in plasma membrane vesicles and reconstituted preparations from rat brain. *Biochemistry* 29:11209-11214.
- Rosental N, Bendahan A, Kanner BI (2006) Multiple consequences of mutating two conserved beta-bridge forming residues in the translocation cycle of a neuronal glutamate transporter. *J Biol Chem* 281:27905-27915.
- Shachnai L, Shimamoto K, Kanner BI (2005) Sulfhydryl modification of cysteine mutants of a neuronal glutamate transporter reveals an inverse relationship between sodium dependent conformational changes and the glutamate-gated anion conductance. *Neuropharmacology* 49:862-871.
- Slotboom DJ, Lolkema JS, Konings WN (1996) Membrane topology of the C-terminal half of the neuronal, glial, and bacterial glutamate transporter family. *J Biol Chem* 271:31317-31321.
- Slotboom DJ, Konings WN, Lolkema JS (1999) Structural features of the glutamate transporter family. *Microbiol Mol Biol Rev* 63:293-307.
- Tanaka K, Watase K, Manabe T, Yamada K, Watanabe M, Takahashi K, Iwama H, Nishikawa T, Ichihara N, Kikuchi T, Okuyama S, Kawashima N, Hori S, Takimoto M, Wada K (1997) Epilepsy and exacerbation of brain injury in mice lacking the glutamate transporter GLT-1. *Science* 276:1699-1702.
- Tao Z, Grewer C (2007) Cooperation of the conserved aspartate 439 and bound amino acid substrate is important for high-affinity Na⁺ binding to the glutamate transporter EAAC1. *J Gen Physiol* 129:331-344.
- Tao Z, Zhang Z, Grewer C (2006) Neutralization of the aspartic acid residue Asp-367, but not Asp-454, inhibits binding of Na⁺ to the glutamate-free form and cycling of the glutamate transporter EAAC1. *J Biol Chem* 281:10263-10272.
- Teichman S, Kanner BI (2007) Aspartate-444 is essential for productive substrate interactions in a neuronal glutamate transporter. *J Gen Physiol* 129:527-539.
- Wadiche JI, Amara SG, Kavanaugh MP (1995) Ion fluxes associated with excitatory amino acid transport. *Neuron* 15:721-728.
- Watzke N, Bamberg E, Grewer C (2001) Early intermediates in the transport cycle of the neuronal excitatory amino acid carrier EAAC1. *J Gen Physiol* 117:547-562.

- Yernool D, Boudker O, Jin Y, Gouaux E (2004) Structure of a glutamate transporter homologue from *Pyrococcus horikoshii*. *Nature* 431:811-818.
- Zerangue N, Kavanaugh MP (1996) Interaction of L-cysteine with a human excitatory amino acid transporter. *J Physiol* 493 (Pt 2):419-423.
- Zhang Y, Kanner BI (1999) Two serine residues of the glutamate transporter GLT-1 are crucial for coupling the fluxes of sodium and the neurotransmitter. *Proc Natl Acad Sci U S A* 96:1710-1715.

Chapter 4: Further computational work

Although the particular focus of my dissertation has been understanding EAAT structure and function, the methods employed through computational modeling, obviously, may be applied in any protein structural analysis. This chapter of my dissertation presents a sampling of applications for computer modeling which have been applied with positive results. These applications also suggests the utility computational modeling holds for science generally.

Introduction: Development of a homology model for clade A human immunodeficiency virus type 1 gp120 to localize temporal substitutions arising in recently infected women

Mary Poss, David C. Holley, Roman Biek, Harold Cox and John Gerdes

There are nine different clades (genotypic subtypes) of HIV-1 (clades A, B, C, D, F, G, H, J, and K) with clade A most common in West and Central Africa and clade B most common in North America and Europe. Not surprisingly, most research has centered on clade B viruses though worldwide there are more clade A infections. The work leading to the computational modeling described below involved identifying and characterizing temporal sequence substitutions that become fixed in viral populations during early infection with clade A viruses. Specifically we were interested in sequence substitutions occurring in the gp120 HIV-1 envelope protein, which is a heavily glycosylated protein expressed on the viral surface and is responsible for binding and entering host cells (Dalglish et al., 1984; Kwong et al., 2000).

In 2000, Kwong et al. published a crystal structure derived from primary isolates of an HIV-1 clade B gp120 complexed to a neutralizing antibody and fragments of a host CD4 receptor. Our work characterizing the clade A-specific substitutions during early infection prompted us to evaluate the tertiary impact of these substitutions to devise possible structural implications. In the following paper we present an homology model based on the Kwong structure (2000) but also incorporating the structure of an NMR derived variable loop (V3 loop) (Catasti et al., 1995; Catasti et al., 1996). The orientation and overall structure of the incorporated V3 loop is remarkably consistent with a gp120 clade B crystal structure published in 2005 (Huang et al., 2005) showing less than 3.0Ås r.m.s.d from the V3 loop in the crystal structure (figure A). Our analysis of the clade A gp120 homology model showed structural compatibility with the clade B structure and that the clade A-specific substitutions arising during early infection are non-random and in certain cases co-locate in regions associated with receptor binding.

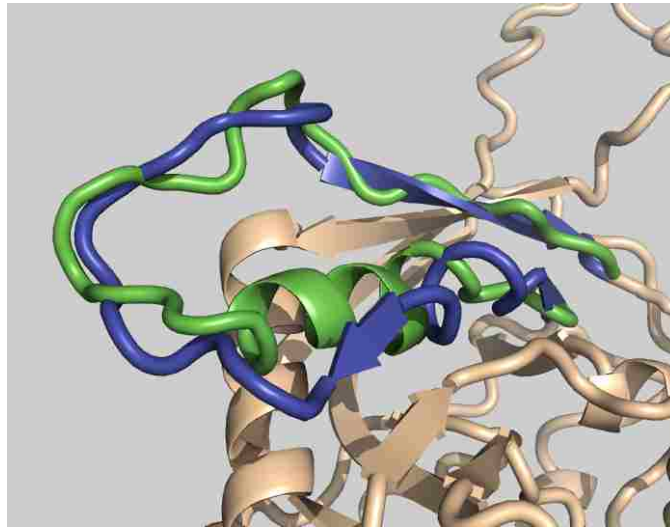


Figure A. NMR derived V3 loop (green) extracted from the clade A gp120 homology model shows similar orientation and structure to a V3 loop (blue) in a later published gp120 crystal structure.

References

- Catasti P, Bradbury EM, Gupta G (1996) Structure and polymorphism of HIV-1 third variable loops. *The Journal of biological chemistry* 271:8236-8242.
- Catasti P, Fontenot JD, Bradbury EM, Gupta G (1995) Local and global structural properties of the HIV-MN V3 loop. *The Journal of biological chemistry* 270:2224-2232.
- Dalgleish AG, Beverley PC, Clapham PR, Crawford DH, Greaves MF, Weiss RA (1984) The CD4 (T4) antigen is an essential component of the receptor for the AIDS retrovirus. *Nature* 312:763-767.
- Huang CC, Tang M, Zhang MY, Majeed S, Montabana E, Stanfield RL, Dimitrov DS, Korber B, Sodroski J, Wilson IA, Wyatt R, Kwong PD (2005) Structure of a V3-containing HIV-1 gp120 core. *Science (New York, NY)* 310:1025-1028.
- Kwong PD, Wyatt R, Sattentau QJ, Sodroski J, Hendrickson WA (2000) Oligomeric modeling and electrostatic analysis of the gp120 envelope glycoprotein of human immunodeficiency virus. *J Virol* 74:1961-1972.

Short Communication

Development of a homology model for clade A human immunodeficiency virus type 1 gp120 to localize temporal substitutions arising in recently infected women

Mary Poss,¹ David C. Holley,² Roman Biek,¹ Harold Cox³
and John Gerdes³

Correspondence

Mary Poss
mary.poss@umontana.edu

Division of Biological Sciences¹, Department of Pharmaceutical Sciences² and Department of Chemistry³, University of Montana, Missoula, MT 59812, USA

Received 13 January 2004
Accepted 23 February 2004

The virus population transmitted by a human immunodeficiency virus type 1 (HIV-1) infected individual undergoes restriction and subsequent diversification in the new host. However, in contrast to men, who have limited virus diversity at seroconversion, there is measurable diversity in viral envelope gene sequences in women infected with clade A HIV-1. In this study, virus sequence diversity in three unrelated, clade A infected women preceding and shortly after seroconversion was evaluated. It was demonstrated that there is measurable evolution of envelope gene sequences over this time interval. Furthermore, in each of the three individuals, amino acid substitutions arose at five or six positions in sequences derived at or shortly after seroconversion relative to sequences obtained from the seronegative sample. Presented here is a model of clade A gp120 to determine the location of substitutions that appeared as the virus population became established in three clade A HIV-1 infected women.

Transmission of human immunodeficiency virus type 1 (HIV-1) from an infected to a naïve host causes significant changes in the genetic make-up of the virus population. HIV-1-infected individuals may harbour up to 10% virus diversity in the viral envelope gene (*env*), depending on the length of infection, but only a subset of these variants initiate the new infection. The inoculum transmitted to a recipient contains diverse genotypes (Learn *et al.*, 2002) but in men the variant pool detected close to the time of seroconversion is essentially homogeneous in *env* (Wolfs *et al.*, 1992; Zhang *et al.*, 1993; Zhu *et al.*, 1993). In contrast, *env* diversity in clade A-infected women is 1–5% at seroconversion (Long *et al.*, 2000; Poss *et al.*, 1995). The factors responsible for different profiles of virus diversity in men and women near seroconversion are unknown.

Diversity in the HIV-1 glycoprotein, gp120, encoded by *env* can significantly impact viral fitness by altering cell tropism and neutralization sensitivity. Substitutions in clade B gp120 that affect receptor and co-receptor binding and antibody interactions have been determined by mutagenesis studies (Boussard *et al.*, 2002; Kwong *et al.*, 2002; Pantophlet *et al.*, 2003; Saphire *et al.*, 2001; Wyatt *et al.*, 1998; Zwick *et al.*, 2003). However, it is not known whether any key functional sites change as the virus establishes infection in a new host. Furthermore, despite the large number of clade A HIV-1-infected individuals worldwide, there has been no research on the structural biology of gp120 of non-clade

B viruses. To gain a better understanding of forces acting on gp120 of a colonizing virus population, we developed a homology model of clade A HIV-1 gp120 to locate substitutions that arose between pre- and post-seroconversion samples in each of three clade A-infected women for whom extensive analysis of HIV-1 diversity (Poss *et al.*, 1995), plasma viral load and post-seroconversion *env* evolution (Poss *et al.*, 1998), and viral phenotype (Painter *et al.*, 2003) have been described.

To determine if there was measurable evolution near the time of infection, we recovered full-length *env* sequences from pre-seroconversion plasma viral RNA samples from each individual and from samples obtained at 20 (Q23), 7 (Q45) or 10 and 49 weeks (Q47) from the pre-seroconversion sample (Poss *et al.*, 1995). The analysis employed a Markov Chain Monte Carlo (MCMC) framework and a general time reversible substitution model for the Bayesian estimation of evolutionary rates (Drummond *et al.*, 2002), incorporating a prior of time to most recent common ancestor estimated from a larger dataset of V1–2 and V3 sequences from these subjects (Poss *et al.*, 1998). The estimated evolutionary rate for Q23 sequences was 2.5% per site per year (95% confidence intervals 1.61–3.35) based on 16 plasma viral RNA sequences from two samples obtained 20 weeks apart. Rates of 0.28% (0.07–0.51) were derived for Q45 based on 17 plasma viral sequences obtained 7 weeks apart. Viral RNA sequences were not available for

Q47 at seroconversion and thus estimated rates of 0.13% (0.05–0.22) were based on eight viral RNA pre-seroconversion sequences, seven proviral DNA sequences obtained 10 weeks later at the time seroconversion was detected, and 10 proviral sequences obtained 7 months after seroconversion. In all cases, confidence intervals excluded zero indicating that measurable rates of evolution occurred in *env*. There was no correlation between plasma viral loads and evolutionary rates in these individuals.

Protein sequences from pre-seroconversion samples were compared to those obtained at or near seroconversion to determine if amino acid replacement occurred in the evolving virus population. Although intra-sample sequence diversity was high (Fig. 1), in all three subjects amino acids at several positions in sequences derived at or shortly after seroconversion were replaced when compared with the sequences detected at the time of infection (Table 1). Six substitutions were fixed in the seroconversion virus population of Q23. Four of these sites have been shown by mutagenesis studies of clade B gp120 to affect the binding of CD4 and one to affect binding of antibodies to the CD4-binding site (CD4BS) (Table 1). Using a null distribution of 66 positions in gp120 affecting CD4 binding (Kwong *et al.*, 1998; Pantophlet *et al.*, 2003; Rizzuto *et al.*, 1998), there was a significantly higher number of substitutions at sites affecting binding to the CD4-binding site than would be expected if substitutions were randomly distributed (Fisher's exact test, $P=0.009$). Substitution T430A is of particular interest because alanine mutagenesis of this site in clade B gp120 strongly increased binding of antibody IgG1b12 (b12) (Pantophlet *et al.*, 2003; Saphire *et al.*, 2001) but decreased binding of CD4 (Rizzuto *et al.*, 1998), suggesting that this substitution could affect the structure of the receptor-binding domain. Three out of five temporal substitutions from Q45 viruses involved sites that affected CD4 and b12 or CCR5 binding to clade B gp120, which is significantly more than would be expected by chance ($P=0.037$). Temporal changes in Q47 sequences did not involve sites that have been investigated for impact on receptor, co-receptor or antibody binding, although sites 278 and 364 are adjacent to residues that contact CD4 (Kwong *et al.*, 1998). None of the temporal substitutions in either Q23 or Q45 sequences affected potential *N*-linked glycosylation sites or involved V1, V2 or V3, and none occurred in the gp41 portion of the glycoprotein (data not shown). In contrast, temporal substitutions in Q47 sequences did involve one site in V1 and gp41 (data not shown) and did result in two new potential *N*-linked glycosylation sites (Table 1).

Of the temporal substitutions identified in these subjects, 50% or more fell outside variable regions. It is particularly noteworthy that none of the early temporal changes affected V3 because fixation of amino acids in V3 did occur over a 2 year period post-seroconversion in sequences obtained from these individuals (Poss *et al.*, 1998). Substitutions that arise in V3 often correlate with a phenotypic

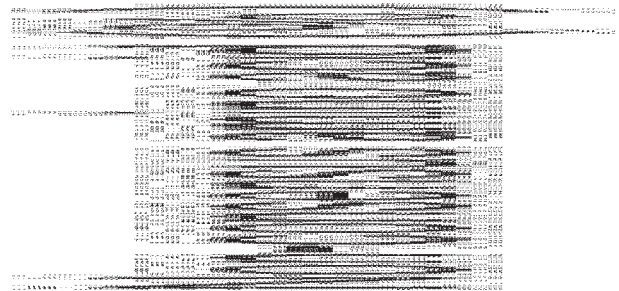


Fig. 1. Distribution of gp120 amino acid substitutions. A consensus sequence was determined for the pre-seroconversion sequences obtained from each of three clade A-infected women. The percentage of sequences that contained an amino acid that differed from the pre-seroconversion consensus at each position is shown for pre-seroconversion sequences (grey lines, 'I') and sequences obtained at or after seroconversion (dashed lines, 'Sc'). The secondary structure elements are relative to the HXBc2 crystal and include only the regions that appear in the crystal structure. The locations of the deleted V1–2 and V3 loops are indicated in the bottom panel by arrowheads. The numbers of sequences in each dataset are; Q23–8 and 8, Q45–9 and 8 and Q47–8 and 17 for pre-seroconversion and post-seroconversion samples, respectively.

change in the virus population (Scarlati *et al.*, 1997; Speck *et al.*, 1997). The fact that the V3 region in the viruses from these individuals does not evolve near the time of infection

Table 1. Summary of temporal substitutions

Subject	Position*	Amino acid infection† (%)	Amino acid post-SC‡ (%)	Secondary structure§	Predicted effect
Q23	T/K232	E (100)	G (100)	ε A	NR¶
Q23	K/Q337	S (100)	R (100)	α2	B6††
Q23	V430	T (100)	A (100)	β21	CD4 & b12††§§
Q23	N/K460	N (100)	D (100)	V5	CD4 & b12††
Q23	S/D461	D (100)	N (100)	V5	CD4 & b12††
Q23	N463	N (100)	F (100)	V5	CD4 & b12††
Q45	N92	E (56)	D (85)	β1	NR
Q45	W395	F (56)	W (85)	β18-V4	CD4 & b12††
Q45	T415	D (100)	T (62)	β19	NR
Q45	I424	V (100)	I (54)	β19-β20	CCR5 & CD4‡‡
Q45	S/D461	K (100)	E (77)	V5	CD4 & b12††
Q47	N241	H (75)	N (88)	β6-β7	NR
Q47	T278	L (88)	S (100)#	ε D	NR
Q47	S364	H (75)	P (100)	β14-β15	NR
Q47	?	S (88)	N (65)	V4-β19	NR
Q47	S/G411	D (88)	N (100)	V4-β19	NR
Q47	T415	I (88)	T (78)#	β19	NR

*Amino acid and position number is relative to HXBc2 (Kwong *et al.*, 1998). Where two amino acids are shown, the second is from primary isolate YU2 (Kwong *et al.*, 2000a).

†Amino acid in single letter nomenclature that was present in sequences obtained from viral RNA in plasma samples obtained before seroconversion (Poss *et al.*, 1995). The percentage shown in parentheses is the proportion of sequences that contain the amino acid shown.

‡Amino acid in single letter nomenclature that was present in sequences obtained from viral RNA (Q23) or RNA and proviral DNA (Q45 and Q47) at or shortly after seroconversion (Poss *et al.*, 1995). The percentage shown in parentheses is the proportion of sequences that contain the amino acid shown.

§Location of the substitution is referenced to the secondary structure determined from the HXBc2 crystal (Kwong *et al.*, 1998).

||Sites determined by mutagenesis to affect CD4BS antibody, receptor or co-receptor binding.

¶Mutagenesis at this site is not reported.

#Substitution creates a new potential N-linked glycosylation site.

††Pantophlet *et al.* (2003).

‡‡Rizzuto *et al.* (1998).

§§Saphire *et al.* (2001).

NR, not reported.

and seroconversion suggests that there may be selection against change in V3 as the virus population becomes established.

Despite the high prevalence of non-clade B HIV-1 infection globally, most structural, evolutionary and therapeutic research on HIV-1 is based on clade B viruses. Thus, it is not clear whether results obtained from clade B gp120 mutagenesis studies are applicable to clade A gp120. A crystal structure for clade B gp120 is available (Kwong *et al.*, 1998, 2000a) and provides the opportunity to determine the structural relatedness of gp120 from clades A and B. Using the clade B structure, we first identified substitutions specific to clade A gp120 from an alignment of consensus sequences of clade B and clade A (available at <http://hiv-web.lanl.gov/>), which are shown in red in

Fig. 2(A, B). Although clade A-specific substitutions are distributed throughout the sequence, there is a preponderance of differences in the 'silent face' of the gp120 outer domain in β sheet 12 and 13 and α helix 2, which flank the V3 loop (Fig. 2A). This α helix is known to be variable both within and between clades, which can lead to presentation of distinct antigenic surfaces to the immune system (Kwong *et al.*, 2000a). In the 3-D structure, substitutions characteristic of clade A occur at periodic intervals in the α helix and in a continuous stretch of the apposing β12 sheet to form a clade A-specific planar surface. In addition, there are several clade A changes within the CD4-binding pocket (Fig. 2B). Clade A HIV-1 gp120s, including all representatives discussed herein, contain a substitution at P369, which is flanked by conserved CD4 contact residues D368 and E370. Substitutions of P369 decrease the binding of

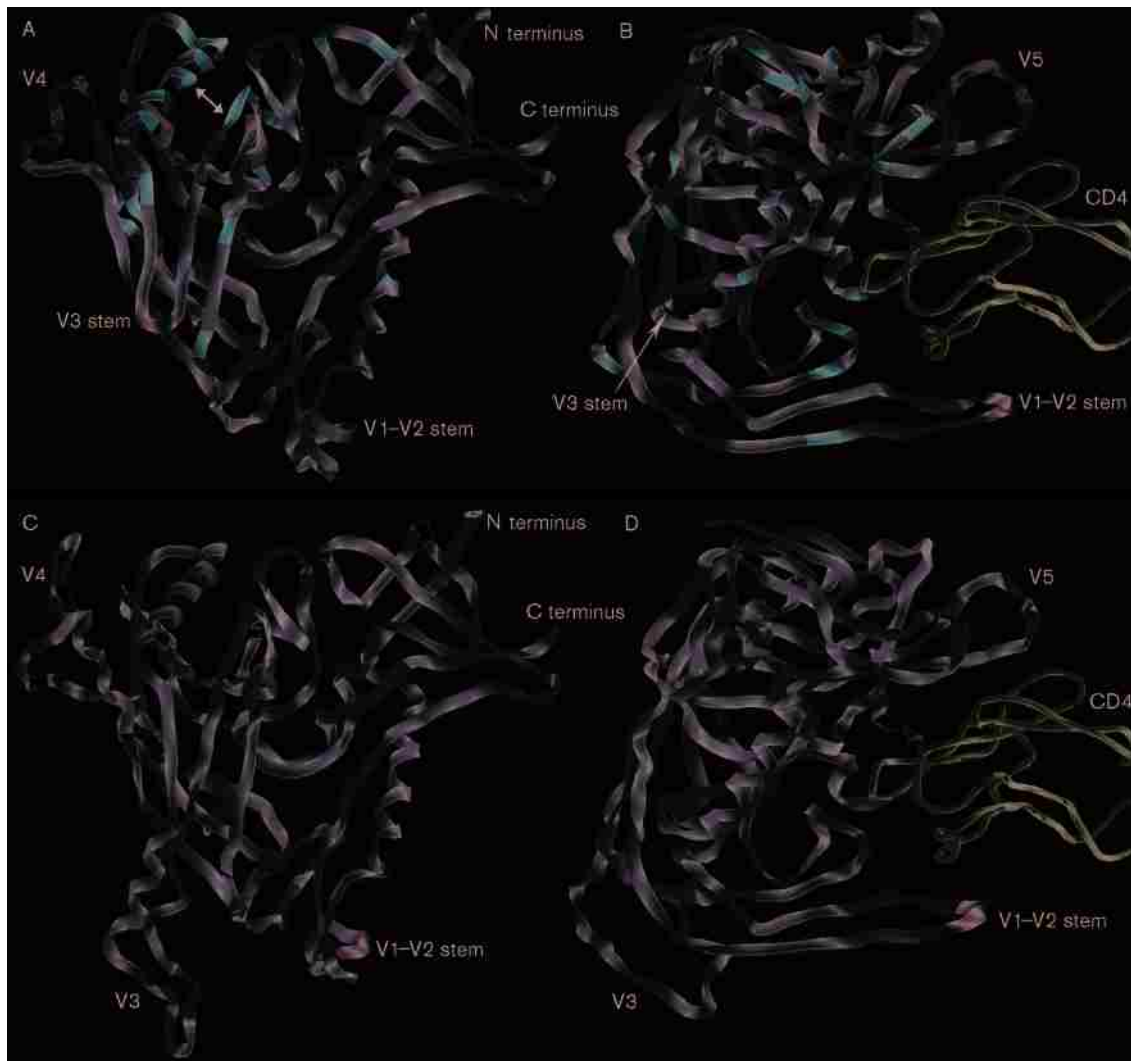


Fig. 2. Topological distribution of clade A-specific substitutions and temporal substitutions arising after infection with clade A HIV-1. (A, B) The structure of clade B gp120 (1G9N) is shown as a ribbon diagram with sites differing between consensus clade B and clade A gp120 depicted in red, the truncated V1–2 and V3 loops indicated in green and the V4 and V5 loops shown in cyan. The arrow in (A) indicates the planar face containing clade A-specific substitutions. Perspective in (A) is with the virus membrane upper right and cell membrane lower left (CD4 is not shown), and in (B) the molecule is rotated approximately 110° around the vertical axis to display the CD4-binding pocket and CD4, shown as a violet tube structure. (C, D) Homology model of clade A HIV-1 based on the sequence of Q47S6 is shown in the same orientation as the clade B structure in (A, B). Temporal substitutions that arose in Q23, Q45 and Q47 sequences are displayed in magenta, cyan and purple, respectively. The temporal substitutions that were shared between viruses are indicated with striping. The V3 loop has been added to the model and adjustments have been made to accommodate the longer clade A V4 loop.

CD4 binding site antibody, b12 (Saphire *et al.*, 2001), and are a feature of clade B neutralization escape mutants (Mo *et al.*, 1997). Clade A-specific substitutions are also present in the bridging sheet, which is involved in co-receptor binding (Kwong *et al.*, 1998). It is noteworthy that there are few clade differences in the inner domain of gp120, a region of contact with gp41 (Kwong *et al.*, 1998).

We developed a homology model of clade A gp120 based on the clade B structure, 1G9N (Kwong *et al.*, 2000a) to

determine the spatial distribution of temporal substitutions from three subjects. The prototype clade A model employed the gp120 sequence of Q23Sc4 (AY069928) because previous phylogenetic analysis demonstrated that Q23 viruses were basal in the clade A tree (Poss *et al.*, 1997), suggesting that they were suitable representatives of clade A gp120. The clade A homology model was built at the Molecular Computational Core Facility at the University of Montana, utilizing an Octane SGI (Silicon Graphics) workstation operated with software SYBYL 6.8 employing Biopolymer,

Composer and ProTable modules (Tripos). The Q23Sc4 sequence was threaded against the 1G9N scaffold using the Composer module, which considers residues that only align with the scaffold, thereby providing a preliminary homology model. The original 1G9N structure is devoid of the first three variable loops. For the homology model, the V1–V2 loop regions were not considered. However, the clade A V3 loop structure was fashioned by a protocol related to Kwong's method (Kwong *et al.*, 2000b) utilizing published NMR conformations of the gp120 clade B V3 loop region (Vranken *et al.*, 2001). Whereas there are clade-specific regions of gp120 (shown in Fig. 2A, B), the core clade A gp120 model structure was found to possess few abnormal ϕ , ψ and ω values (using ProTable; Lovell *et al.*, 2000) relative to those of the X-ray-derived core clade B gp120 structure, suggesting a noteworthy degree of core structural similarity between the protein representations. The clade A V4 loop is longer than that of the 1G9N crystal. Therefore, the additional amino acids were accommodated by clipping at the V4 N-terminal side, inserting the extra clade A amino acids, followed by adjusting select bond rotations at the loop C-terminal end to allow loop attachment to the core structure. To obtain a refined Q23Sc4 homology model (Fig. 2C, D), side chain clashes between the V3 and V4 loops were minimized, first by changing select bond torsions to provide ϕ , ψ and ω values consistent with established standards (Lovell *et al.*, 2000), followed by local V3 and V4 energetic minimizations (Tripos force field) to their respective nearest energy wells.

The sequence with the longest V4 region, Q47S6 (AY288084), was threaded against the Q23Sc4 homology structure to display the temporal substitution. Virus populations from each of the three individuals evolved a temporal substitution in the inner domain near the truncated N terminus of gp120 (Fig. 2C), a region that is proximal to the viral membrane and that also accommodated clade A-specific changes (Fig. 2A). The remainder of the inner domain did not change in the period following infection. Both Q45 and Q47 viruses had amino acid substitutions in V4 and the V4 stem, a region on the outer domain of the protein that does not contribute to virus neutralization. In both the Q23 and Q45 virus populations, temporal substitutions involved the bridging sheet and the V5 region (Fig. 2D), which forms an upper surface to the CD4-binding pocket and has been implicated by mutagenesis to affect gp120–receptor interaction (Table 1). One of the Q47 substitutions (H364P) also lies on the lateral surface of the binding pocket and is adjacent to key CD4 contact residues (Kwong *et al.*, 1998).

Our data demonstrate that in three independent infections there is measurable evolution in HIV-1 *env* preceding and following seroconversion. We provide the first model of clade A gp120 and demonstrate that it has significant structural similarity with the clade B glycoprotein and that substitutions arising as the virus population becomes established in three hosts are not randomly distributed in

the protein. Furthermore, in two of the three subjects there were significantly more changes at sites shown by mutagenesis of clade B gp120 to affect receptor or co-receptor binding than would be expected by chance. Further studies of the substitutions that arise soon after infection, will be valuable to understand selective forces acting on the infecting virus population and to inform efforts aimed at preventing establishment of new infections.

Acknowledgements

The authors thank Drs Joan Kreiss, Harold Martin, Jr and their collaborators at the Ganjoni Municipal Clinic and Coast Provincial General Hospital, Mombasa, Kenya for sample collection and Dr Julie Overbaugh for providing plasma samples. This research was supported in part by NIH AI44609. Partial support for D. C. H. and H. C. came from Montana NSF-EPSCoR, EPS-0091995 and for J. G. from NIH-NCRR, NIH P20 RR15583. Funding for the Molecular Computational Core Facility, Center for Structural and Functional Neuroscience, was derived from NIH P20 RR15583-01 and the NSF EPS-0091995.

References

- Boussard, C., Doyle, V. E., Mahmood, N., Klimkait, T., Pritchard, M. & Gilbert, I. H. (2002). Design, synthesis and evaluation of peptide libraries as potential anti-HIV compounds, via inhibition of gp120/cell membrane interactions, using the gp120/cd4/fab17 crystal structure. *Eur J Med Chem* **37**, 883–890.
- Drummond, A. J., Nicholls, G. K., Rodrigo, A. G. & Solomon, W. (2002). Estimating mutation parameters, population history and genealogy simultaneously from temporally spaced sequence data. *Genetics* **161**, 1307–1320.
- Kwong, P. D., Wyatt, R., Robinson, J., Sweet, R. W., Sodroski, J. & Hendrickson, W. A. (1998). Structure of an HIV gp120 envelope glycoprotein in complex with the CD4 receptor and a neutralizing human antibody. *Nature* **393**, 648–659.
- Kwong, P. D., Wyatt, R., Majeed, S., Robinson, J., Sweet, R. W., Sodroski, J. & Hendrickson, W. A. (2000a). Structures of HIV-1 gp120 envelope glycoproteins from laboratory-adapted and primary isolates. *Structure Fold Des* **8**, 1329–1339.
- Kwong, P. D., Wyatt, R., Sattentau, Q. J., Sodroski, J. & Hendrickson, W. A. (2000b). Oligomeric modeling and electrostatic analysis of the gp120 envelope glycoprotein of human immunodeficiency virus. *J Virol* **74**, 1961–1972.
- Kwong, P. D., Doyle, M. L., Casper, D. J. & 18 other authors (2002). HIV-1 evades antibody-mediated neutralization through conformational masking of receptor-binding sites. *Nature* **420**, 678–682.
- Learn, G. H., Muthui, D., Brodie, S. J., Zhu, T., Diem, K., Mullins, J. I. & Corey, L. (2002). Virus population homogenization following acute human immunodeficiency virus type 1 infection. *J Virol* **76**, 11953–11959.
- Long, E. M., Martin, H. L., Jr, Kreiss, J. K., Rainwater, S. M., Lavreys, L., Jackson, D. J., Rakwar, J., Mandaliya, K. & Overbaugh, J. (2000). Gender differences in HIV-1 diversity at time of infection. *Nat Med* **6**, 71–75.
- Lovell, S. C., Word, J. M., Richardson, J. S. & Richardson, D. C. (2000). The penultimate rotamer library. *Proteins* **40**, 389–408.
- Mo, H., Stamatatos, L., Ip, J. E., Barbas, C. F., Parren, P. W., Burton, D. R., Moore, J. P. & Ho, D. D. (1997). Human immunodeficiency virus type 1 mutants that escape neutralization by human monoclonal antibody IgG1b12. *J Virol* **71**, 6869–6874.

- Painter, S. L., Biek, R., Holley, D. C. & Poss, M. (2003). Envelope variants from women recently infected with clade A human immunodeficiency virus type 1 confer distinct phenotypes that are discerned by competition and neutralization experiments. *J Virol* **77**, 8448–8461.
- Pantophlet, R., Ollmann Saphire, E., Pognard, P., Parren, P. W., Wilson, I. A. & Burton, D. R. (2003). Fine mapping of the interaction of neutralizing and nonneutralizing monoclonal antibodies with the CD4 binding site of human immunodeficiency virus type 1 gp120. *J Virol* **77**, 642–658.
- Poss, M., Martin, H. L., Kreiss, J. K., Granville, L., Chohan, B., Nyange, P., Mandaliya, K. & Overbaugh, J. (1995). Diversity in virus populations from genital secretions and peripheral blood in women recently infected with human immunodeficiency virus type 1. *J Virol* **69**, 8118–8122.
- Poss, M., Gosink, J., Thomas, E., Kreiss, J. K., Ndinya-Achola, J., Mandaliya, K., Bwayo, J. & Overbaugh, J. (1997). Phylogenetic evaluation of Kenyan HIV-1 isolates. *AIDS Res Hum Retroviruses* **13**, 493–499.
- Poss, M., Rodrigo, A. G., Gosink, J. J., Learn, G. H., de Vange Panteleeff, D. D., Martin, H. L., Jr, Bwayo, J., Kreiss, J. K. & Overbaugh, J. (1998). Evolution of envelope sequences from the genital tract and peripheral blood of women infected with clade A human immunodeficiency virus type 1. *J Virol* **72**, 8240–8251.
- Rizzuto, C. D., Wyatt, R., Hernandez-Ramos, N., Sun, Y., Kwong, P. D., Hendrickson, W. A. & Sodroski, J. (1998). A conserved HIV gp120 glycoprotein structure involved in chemokine receptor binding. *Science* **280**, 1949–1953.
- Saphire, E. O., Parren, P. W., Pantophlet, R. & 7 other authors (2001). Crystal structure of a neutralizing human IGG against HIV-1: a template for vaccine design. *Science* **293**, 1155–1159.
- Scarlati, G., Tresoldi, E., Bjorndal, A. & 9 other authors (1997). *In vivo* evolution of HIV-1 co-receptor usage and sensitivity to chemokine-mediated suppression. *Nat Med* **3**, 1259–1265.
- Speck, R. F., Wehrly, K., Platt, E. J., Atchison, R. E., Charo, I. F., Kabat, D., Chesebro, B. & Goldsmith, M. A. (1997). Selective employment of chemokine receptors as human immunodeficiency virus type 1 coreceptors determined by individual amino acids within the envelope V3 loop. *J Virol* **71**, 7136–7139.
- Vranken, W. F., Fant, F., Budesinsky, M. & Borremans, F. A. (2001). Conformational model for the consensus V3 loop of the envelope protein gp120 of HIV-1 in a 20% trifluoroethanol/water solution. *Eur J Biochem* **268**, 2620–2628.
- Wolfs, T. F., Zwart, G., Bakker, M. & Goudsmit, J. (1992). HIV-1 genomic RNA diversification following sexual and parenteral virus transmission. *Virology* **189**, 103–110.
- Wyatt, R., Kwong, P. D., Desjardins, E., Sweet, R. W., Robinson, J., Hendrickson, W. A. & Sodroski, J. G. (1998). The antigenic structure of the HIV gp120 envelope glycoprotein. *Nature* **393**, 705–711.
- Zhang, L. Q., MacKenzie, P., Cleland, A., Holmes, E. C., Brown, A. J. & Simmonds, P. (1993). Selection for specific sequences in the external envelope protein of human immunodeficiency virus type 1 upon primary infection. *J Virol* **67**, 3345–3356.
- Zhu, T., Mo, H., Wang, N., Nam, D. S., Cao, Y., Koup, R. A. & Ho, D. D. (1993). Genotypic and phenotypic characterization of HIV-1 patients with primary infection. *Science* **261**, 1179–1181.
- Zwick, M. B., Kelleher, R., Jensen, R., Labrijn, A. F., Wang, M., Quinnan, G. V., Jr, Parren, P. W. & Burton, D. R. (2003). A novel human antibody against human immunodeficiency virus type 1 gp120 is V1, V2, and V3 loop dependent and helps delimit the epitope of the broadly neutralizing antibody immunoglobulin G1 b12. *J Virol* **77**, 6965–6978.

Introduction: Novel Lavendamycin Analogues as Antitumor Agents: Synthesis, *In Vitro* Cytotoxicity, Structure–Metabolism, and Computational Molecular Modeling Studies with NAD(P)H:Quinone Oxidoreductase 1

Mary Hassani, Wen Cai, David C. Holley, Jayana P. Lineswala, Babu R. Maharjan, G. Reza Ebrahimian, Hassan Seradj, Mark G. Stocksdale, Farahnaz Mohammadi, Christopher C. Marvin, John M. Gerdes, Howard D. Beall, and Mohammad Behforouz

NAD(P)H:quinone oxidoreductase (NQO1) is over-expressed in many tumor cell types and facilitates the activation of cytotoxic agents through a two electron reduction process involving a bound FAD co-factor. Lavendamycin has broad antitumor activity (Boger et al., 1987) but is too toxic for use in chemotherapy. The following study by Hassani et al. (2005) evaluates novel lavendamycin derivatives for selective antitumor activity through interactions with NQO1.

The computational component of this study was included to determine and differentiate interactions between NQO1 and two of the lavendamycin analogues. We used the protein data bank coordinates of an FAD- and substrate-bound NQO1 crystal structure as the target protein for computational molecular docking of the two selected lavendamycin analogues. The analogues had been gauged *in vitro* as either a very poor substrate (compound **31**) or as a good substrate (compound **37**) for NQO1 bioactivation. This allowed for a comparative analysis of docked poses to identify substrate interactions that promote or hinder binding and bio-reduction in NQO1.

The findings from the docking study were consistent with the *in vitro* evaluations showing that docked poses of the poor substrate (**31**) scored lower than docked poses of the good substrate (**37**) (table 7). Furthermore, high ranked poses of compound **37** oriented very similar to the analogous substrate (compound **65**) included in the NQO1 crystal structure with aromatic rings of compound **37** stacking over rings of the FAD (figures 2c, 2d and 3a). In comparison, none of the poses of compound **31** oriented similar to compound **65**. Likewise, analysis of the interactions between NQO1 and top ranked poses of compound **37** revealed hydrogen-bonding between compound **37** and NQO1 residues that are involved in the electron reduction process necessary for substrate bioactivation (figure 3b and 3c). These interactions were not detected in any of the compound **31** poses. High-ranked docked poses of compound **37** also show hydrogen-bonding between a substituent group of compound **37** (CH₂OH group at position R³) and key NQO1 residues that could possibly confer substrate selectivity (figures

3b and 3c). Overall, the docking exercise demonstrated that poses of compound **37** were oriented more consistent with known interactions between NQO1 and analogous substrates than any of the compound **31** docked poses.

References

Boger DL, Yasuda M, Mitscher LA, Drake SD, Kitos PA, Thompson SC (1987) Streptonigrin and lavendamycin partial structures. Probes for the minimum, potent pharmacophore of streptonigrin, lavendamycin, and synthetic quinoline-5,8-diones. *J of Med Chem* 30:1918-1928.

Novel Lavendamycin Analogues as Antitumor Agents: Synthesis, in Vitro Cytotoxicity, Structure–Metabolism, and Computational Molecular Modeling Studies with NAD(P)H:Quinone Oxidoreductase 1

Mary Hassani,[†] Wen Cai,[‡] David C. Holley,[§] Jayana P. Lineswala,[‡] Babu R. Maharjan,[‡] G. Reza Ebrahimian,[‡] Hassan Seradj,[‡] Mark G. Stocksdales,[‡] Farahnaz Mohammadi,[‡] Christopher C. Marvin,[‡] John M. Gerdes,[§] Howard D. Beall,^{*,†} and Mohammad Behforouz^{*,‡}

Department of Chemistry, Ball State University, Muncie, Indiana 47306, Center for Environmental Health Sciences, Department of Biomedical and Pharmaceutical Sciences, The University of Montana, Missoula, Montana 59812, and Molecular Computational Core Facility, Center for Structural and Functional Neuroscience and Department of Chemistry, The University of Montana, Missoula, Montana 59812

Received August 2, 2005

Novel lavendamycin analogues with various substituents were synthesized and evaluated as potential NAD(P)H:quinone oxidoreductase (NQO1)-directed antitumor agents. Pictet–Spengler condensation of quinoline- or quinoline-5,8-dione aldehydes with tryptamine or tryptophans yielded the lavendamycins. Metabolism studies with recombinant human NQO1 revealed that addition of NH₂ and CH₂OH groups at the quinolinedione-7-position and indolopyridine-2'-position had the greatest positive impact on substrate specificity. The best and poorest substrates were **37** (2'-CH₂OH-7-NH₂ derivative) and **31** (2'-CONH₂-7-NHCOC₃H_{7-n} derivative) with reduction rates of 263 ± 30 and 0.1 ± 0.1 μmol/min/mg NQO1, respectively. Cytotoxicity toward human colon adenocarcinoma cells was determined for the lavendamycins. The best substrates for NQO1 were also the most selectively toxic to the NQO1-rich BE-NQ cells compared to NQO1-deficient BE-WT cells with **37** as the most selective. Molecular docking supported a model in which the best substrates were capable of efficient hydrogen-bonding interactions with key residues of the active site along with hydride ion reception.

Introduction

The goal of current cancer drug discovery is to design cytotoxic compounds that selectively interact with molecular targets ideally unique to tumor cells with minimal toxicity to normal cells.^{1–3} One approach to achieve selective toxicity is through bioreductive activation and identifying reductase enzymes that are overexpressed in tumor cells when compared to normal cells.^{1,3–5} NAD(P)H:quinone oxidoreductase 1 (NQO1, DT-diaphorase, EC 1.6.99.2, DTD or QR1) is a widely distributed homodimeric flavoenzyme composed of two closely associated monomers of 273 residues, each containing one molecule of the noncovalently attached FAD cofactor molecule that is required for NQO1 catalytic activity.^{6–10} This obligate two-electron reductase is present in cytosol (>90%)¹¹ and nucleus¹² and catalyzes a nicotinamide nucleotide-dependent two-electron reduction^{13,14} and the bioactivation of quinone chemotherapeutic compounds such as mitomycins, indoloquinones, anthracyclines, and aziridinylbenzoquinones.^{15–19} Marked elevations in NQO1 activity and mRNA content in primary tumors from lung, liver, colon and breast,²⁰ and lung,²¹ liver,²² brain,²³ and colorectal²⁴

tumors suggest that antitumor compounds that are bioactivated by NQO1 may be selectively toxic to those tumors.

The crystal structure of the apo recombinant human NQO1 has been determined to a resolution of 1.7 Å.⁹ Each monomer of the physiological dimer of NQO1 is composed of two distinct domains such that residues 1–220 and 221–273 form a major catalytic and a small C-terminal domain, respectively.^{9,10,25,26} Two equivalent active sites are located at the dimer interface and are formed by portions of both subunits.^{6,9} The active site of the enzyme is a hydrophobic and plastic pocket with three potential hydrogen-bonding residues (Tyr-126 and -128 and His-161) that can bind and accommodate a broad range of structures including large quinone compounds.^{9,25} The substrate binding pocket (360 Å³) sequentially binds NAD(P)H and the quinone substrate and is formed by residues from both monomers.^{9,10,25}

NQO1 promotes an obligatory two-electron reduction called a ping-pong mechanism such that in the first half of the reaction a hydride ion from NAD(P)H is transferred to the N5 of the FAD followed by the release of NAD(P)⁺.^{10,27,28} The hydride donation from the FADH₂ N5 to the hydride-acceptor substrate (across a 4 Å distance²⁸) can then be done at either a carbonyl oxygen or ring carbon followed by hydroquinone release. The remaining proton can be provided by Tyr-126, -128, or His-161.^{10,27,28} Quinone substrates can bind to the NQO1 active site in more than one orientation, and homologous compounds with different substituents may bind to the NQO1 active site in different orientations.^{25,27}

* Corresponding authors for chemistry (M.B.) and biology (H.D.B.): M. Behforouz: Phone, 765-285-8070; Fax, 765-285-6505; E-mail, mbehforo@bsu.edu. H. D. Beall: Phone, 406-243-5112; Fax, 406-243-5228; E-mail, howard.beall@umontana.edu.

[‡] Department of Chemistry, Ball State University.

[†] Center for Environmental Health Sciences, The University of Montana.

[§] Molecular Computational Core Facility, The University of Montana.

Scheme 1



Lavendamycin (**1a**), a bacterially derived quinolinedione antibiotic, was isolated from the fermentation broth of *Streptomyces lavendulae* in 1981.²⁹ Lavendamycin is structurally^{29,30} and biosynthetically^{31–33} related to streptonigrin (SN) (**2**), another potent 7-aminoquinoline-



5,8-dione antitumor antibiotic. Earlier work has shown that the use of both of these antitumor agents as potential drugs has been precluded due to their high degree of toxicity.^{30,34,35} However, in contrast to the parent compound, we have found that a significant number of lavendamycin derivatives have low animal toxicity but show strong antitumor activity or are potent inhibitors of the HIV-reverse transcriptase.^{36–38} These studies have been possible only through our success in developing short and efficient syntheses for a variety of lavendamycin analogues possessing the full pentacyclic structure. For instance, compared to the previously reported syntheses of lavendamycin ester (**1b**) in overall yields of 0.5 to 2% and in 9 to 20 steps,^{39,40} we were able to synthesize **1b** in 5-step methods^{41,42} with overall yields of nearly 40%.

This study was conducted to clarify the role of NQO1 in the bioactivation of lavendamycin analogues. Specifically, the objectives were to analyze the effects of functional group changes on the reduction efficiency of lavendamycin analogues by NQO1, to verify whether activation by NQO1 resulted in selective cytotoxicity of these compounds and to correlate the metabolism and biological data of the compounds with predictions of their active site positioning, hydrogen bond formation, and hydride ion reception capability. For this study, we were in need of a large number of variously substituted lavendamycins possessing zero to four substituents on their pentacyclic system for which their syntheses are described below. Additionally, the synthesis of a number of quinolinediones is reported.

Results and Discussion

Synthetic Chemistry. A range of lavendamycin analogues was designed and synthesized to explore the effects of various substituents on the metabolism of

Table 1. Structures of Lavendamycin Analogues, Reaction Conditions and Yields

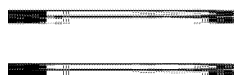
no.	R ¹	R ²	% yield	solvent	h (°C) ^a
14	CH ₃ CO	H	83	anisole	5 (reflux)
15	CH ₃ CO	CO ₂ CH ₃	67	anisole	4.5 (reflux)
16	CH ₃ CO	CO ₂ C ₄ H _{9-n}	63	xylene	4 (reflux)
17	CH ₃ CO	CO ₂ C ₅ H _{11-n}	44	xylene	4.5 (reflux)
18	CH ₃ CO	CO ₂ C ₅ H _{11-i}	50	xylene	9.5 (28–130)
19	CH ₃ CO	CO ₂ C ₆ H _{13-n}	54	xylene	5.5 (reflux)
20	CH ₃ CO	CO-piperidino	56	anisole	17 (reflux)
21	CH ₃ CO	CO-morpholino	57	anisole	18 (reflux)
22	CH ₃ CO	CH ₂ OH	48	anisole	4 (25–155)
23	ClCH ₂ CO	CO ₂ C ₅ H _{11-i}	57	xylene	5 (76)

^a Except for compounds **18**, **22** and **23** the reaction mixtures were slowly heated to reflux over a period of approximately 3 h and then refluxed for the designated times.

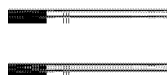
these analogues by recombinant human NQO1. Pictet–Spengler condensation (Scheme 1) of 7-*N*-acylamino-2-formylquinoline-5,8-diones **3** or **4** with tryptamine, or derivatives of tryptophan or β -methyltryptophan (**5–13**), yielded lavendamycin analogues **14–23**.

In a typical procedure, aldehydes **3** or **4** (0.1 mmol) were mixed with the corresponding tryptamine or tryptophan derivatives in dry anisole or xylene under argon, and while being magnetically stirred, the mixture was gradually heated to reflux over a period of 3 h.^{38,41,42} The resulting clear solution was refluxed until TLC showed the absence of the starting materials. The mixture was concentrated or evaporated to dryness. The products were either precipitated from the concentrated solutions or purified by washing with solvents. The structures of the resulting lavendamycins, the reaction conditions, and the yields are shown in Table 1. Table 2 presents the structures of a number of other novel lavendamycins as well as some of our previously synthesized derivatives. Table 3 lists the structures of quinolinediones. The lavendamycin analogues shown in the tables are the subject of the biological tests in this study.

Following Scheme 2, aldehydes **3** and **43** were prepared according to our reported syntheses.^{38,41,42} Aldehyde **4** was obtained by the reduction of **47**, then chloroacetylation of the resulting amino salt followed by two consecutive oxidations.

Table 2. Structures of Lavendamycin Analogues

no.	R ¹	R ²	R ³	R ⁴	refs
24	CH ₃ CONH	pyrrolidino	CO ₂ CH ₃	CH ₃	
25	CH ₃ CONH	aziridino	CONH ₂	H	
26	CH ₃ CONH	H	CO ₂ CH ₃	CH ₃	41, 42
27	CH ₃ CONH	H	CO ₂ C ₈ H _{17-n}	H	38
28	CH ₃ CONH	H	CO ₂ (CH ₂) ₂ OH	H	38
29	CH ₃ CONH	H	CO ₂ (CH ₂) ₂ OPO ₃ H ₂	H	38
30	CH ₃ CONH	H	CONH ₂	H	38
31	<i>n</i> -C ₃ H ₇ CONH	H	CONH ₂	H	38
32	NH ₂	Cl	CO ₂ CH ₃	CH ₃	
33	NH ₂	H	CO ₂ CH ₃	CH ₃	41, 42
34	Br	H	CO ₂ CH ₃	CH ₃	
35	NH ₂	H	CO ₂ C ₈ H _{17-n}	H	38
36	NH ₂	H	CONH ₂	H	38
37	NH ₂	H	CH ₂ OH	H	
38	NH ₂	H	H	H	
39	H	H	H	H	

Table 3. Structures of Quinoline-5,8-diones

no.	R ¹	R ²	R ³	refs
3	CH ₃ CONH	H	CHO	41, 42
4	ClCH ₂ CONH	H	CHO	
40	CH ₃ CONH	H	CH ₃	41, 42
41	ClCH ₂ CONH	H	CH ₃	
42	<i>n</i> -C ₃ H ₇ CONH	H	CHO	38
43	<i>n</i> -C ₃ H ₇ CONH	H	CHO	38
44	NH ₂	H	CH ₃	38
45	NH ₂	Cl	CH ₃	38
46	NH ₂	Cl	CHO	

Tryptamine (**5**) is commercially available and tryptophans **6**, **7** and **13** were obtained by the neutralization of the commercially available salts with ammonia (14%) and extraction with ethyl acetate. Tryptophan esters **8–10** were prepared by the Fischer esterification of the tryptophans with the corresponding alcohols. β -Methyltryptophan methyl ester necessary for the synthesis of **32** and **57**, the precursor of **34** was prepared according to our own reported procedure.⁴³

Chloroaldehyde **46** was obtained following the chemistry in Scheme 3.⁴⁴

The 6-substituted pyrrolidino and aziridino lavendamycins were synthesized by an efficient Michael addition of the amines to the corresponding lavendamycins in excellent yields according to Scheme 4.⁴⁵

Amino analogues **37** and **38** were prepared by the acid hydrolysis of acetyl derivatives **22** and **14** in high yields as shown in Scheme 5.

Bromo analogue **34** and unsubstituted lavendamycin **39** were synthesized following the reactions presented in Scheme 6. Quinoline aldehydes **55** and **56** were synthesized by the selenium dioxide oxidation of the commercially available **53** and **54** followed by the condensation with β -methyltryptophan methyl ester or

tryptamine to produce **57** and **58** which then oxidized by bis[(trifluoroacetoxy)iodo]benzene⁴⁶ to the products.

Scheme 7 presents the steps in the synthesis of the desired piperidine and morpholine amides of tryptophan. Tryptophans **11** and **12** were prepared in relatively good yields by a method similar to that of Tolstikov used for the synthesis of streptonigrin derivatives.⁴⁷

Electrochemistry. The aim of the electrochemical studies was to determine the relative ease of reduction of the lavendamycin analogues and to compare how the electrochemical behavior of these compounds correlates with their reduction rate by NQO1. Electrochemical studies of a number of lavendamycin analogues were carried out. In these studies, dried dimethyl sulfoxide (DMSO) and tetrabutylammonium hexafluorophosphate (Bu₄NPF₆) were used as solvent and the supporting electrolyte, respectively. Cathodic and anodic peak potentials, E_{pc} and E_{pa} , respectively, were measured and the midpoint of the peak potentials was used to determine $E_{1/2}$ values, $E_{1/2} = (E_{pc} + E_{pa})/2$. $E_{1/2}$ values were consistent for the potential sweep rates in the range of 50 to 500 mV/s. The $E_{1/2}$ values determined from the recorded voltammograms at the potential sweep rates of 50, 100, 200, 400, and 500 mV/s were averaged and reported with reference to ferrocene (Fc^{0/+}) $E_{1/2}$ value (Table 4).

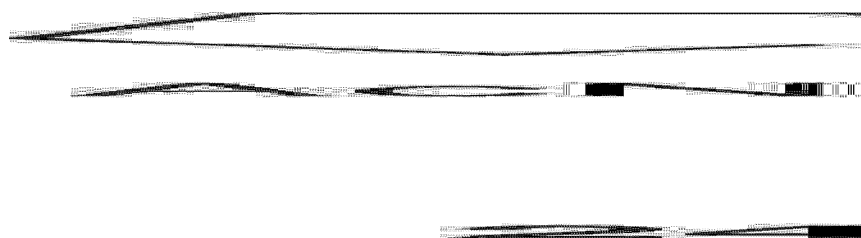
All of the lavendamycin analogues exhibited reversible electrochemistry. The analogues with electron-withdrawing groups at the R¹ position showed similar $E_{1/2}$ values, between -0.85 and -0.99 V, with the exception of compound **24** that exhibited a slightly more negative $E_{1/2}$ value which can be in part due to the presence of an electron-donating group at the R² position (Table 4). The lavendamycin analogues with electron-donating groups at the R¹ position showed slightly more negative $E_{1/2}$ values, between -1.01 and -1.09 V, compared to the former group (Table 4). In general, the lavendamycin analogues with electron-withdrawing groups at the R¹ position were easier to reduce compared to the ones with electron-donating groups at this position. Although all of the investigated lavendamycin analogues possessed similar $E_{1/2}$ values (-0.85 to -1.13 V) (Table 4), the rate of reduction of these compounds by NQO1 differed dramatically (Table 5). When the electrochemical reduction potential and rate of reduction of the lavendamycin analogues by NQO1 were compared, no direct correlation between the two factors was found (data not shown). This finding along with our molecular modeling studies suggest that other factors such as lavendamycins substituent size, steric influence, active site positioning, and hydrogen bond formation capability may be more important than the electrochemical reduction potential and electronic effects to determine the reduction efficiency of these compounds by NQO1. Electrochemical studies can be used to determine the ease of reduction of compounds, but there is often no overall or very small association between the rate of reduction by NQO1 and reduction potential for quinones such as indolequinones^{48–50} and quinolinequinones⁵¹ as previously reported. The lavendamycin analogues exhibited similar reduction potential values to the quinolinequinone compounds studied by Fryatt et al.⁵¹ Also, they were easier to reduce ($E_{1/2}$ values = -0.85 to -1.13 V) than the indolequinones previously

Scheme 2^a

^a Reagents and conditions: (a) Pd-C, 5%, H₂ (30 psi), HCl-H₂O, 15 h, rt; (b) (RCO)₂O, NaOAc, Na₂SO₃, 2.5 h, rt to 0 °C; (c) K₂Cr₂O₇, HOAc, 12 h, rt; (d) SeO₂, dioxane, H₂O, 9–29.5 h, reflux.

Scheme 3^a

^a Reagents and conditions: (a) HCl (gas), dry MeOH, 22 h, 60 °C; (b) SeO₂, dioxane, H₂O, 23 h, reflux; (c) β-methyltryptophan methyl ester, anisole, 3 h, rt to 130 °C, then 1 h, reflux.

Scheme 4^a

^a Reagents and conditions: (a) aziridine, CHCl₃, 48 h, rt; (b) pyrrolidine, CHCl₃, 2 h, rt.

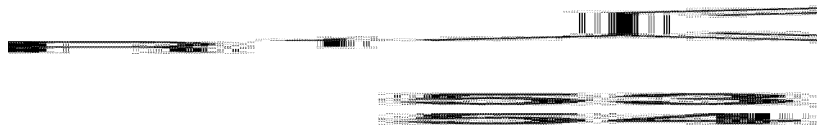
Scheme 5^a

^a Reagents and conditions: (a) H₂SO₄ (70%), 2–4 h, 60 °C.

studied by Beall et al. and Swann et al. ($E_{1/2}$ values = -1.19 to -1.61 V).^{49,50}

Biological Studies. Metabolism of the novel lavendamycin analogues by recombinant human NQO1 and cytotoxicity to human colon adenocarcinoma cells with either no detectable NQO1 activity (BE-WT) or with high NQO1 activity (BE-NQ) were examined. The effect of functional group changes on reduction efficiency and rate of reduction by NQO1 was studied using a spectrophotometric assay that employs cytochrome *c* as the terminal electron acceptor⁵² and gives initial rates of lavendamycin analogues reduction (Table 5). The initial reduction rates (μmol cytochrome *c* reduced/min/mg NQO1) were calculated from the linear portion (0–30 s) of the reaction graphs.

Large substituents at the quinolinedione-7-position (R^1) of the lavendamycin analogues were poorly tolerated and greatly reduced the metabolism rate of the analogues by NQO1 compared to smaller substituents (**31** vs **36**, **18** vs **23**, and **30** vs **31**) (Table 5). Large substituents such as NHCOC_3H_7 -*n* in **31** at the 7-position had the most negative impact on the rate of reduction by NQO1 whereas NH_2 followed by the NHCOCH_3 group were the best substituents for this position (Table 5). This could partly be due to steric hindrance between the quinolinedione moiety (5,8-dione ring enters the active site first) and NQO1 active site that results in unfavorable positioning of the lavendamycin analogues for hydride ion reception from FADH_2 and quinone reduction. Our molecular modeling studies also demonstrated that placing a small substituent at the R^1 position that is capable of hydrogen bonding with key residues of the active site could be a contributing factor to substrate specificity. Faig et al. determined that positions of **63** (RH1), 2,5-diaziridinyl-3-(hydroxymethyl)-6-methyl-1,4-benzoquinone,⁵³ that point to the inner part of the NQO1 active site could accommodate only small substituents.²⁵ Also, 1,4-naphthoquinones with small substituents such as an aziridine ring or CH_3 at C2 and no substituents at C3 were reported to be

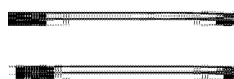
Scheme 6^a

^a Reagents and conditions: (a) SeO₂, wet dioxane, 2 h, rt to reflux, then 17–22 h, reflux; (b) tryptamine or β-methyltryptophan methyl ester, anisole, 3 h, rt to reflux, then 22–39 h, reflux, then Pd–C, 5%, 28 h, reflux; (c) Bis[(trifluoroacetoxy)iodo]benzene, CH₃CN–H₂O, 2 h, 0 °C.

Scheme 7^a

^a Reagents and conditions: (a) *N*-hydroxysuccinimide, DCC, 2 h, 12–20 °C, dioxane (b) amine, Et₃N, EtOH, CH₃Cl₃, rt, 1 h (c) dry ammonium formate, Pd–C, 10%, dry methanol, rt, 30 min.

Table 4. Electrochemical Reduction Potentials^a (DMSO) of Lavendamycin Analogues versus Ferrocene



no.	R ¹	R ²	R ³	R ⁴	<i>E</i> _{pc} (V)	<i>E</i> _{pa} (V)	<i>E</i> _{1/2} (V) vs Fc
14	CH ₃ CONH	H	H	H	-0.95	-0.95	-0.95
15	CH ₃ CONH	H	CO ₂ CH ₃	H	-0.92	-0.83	-0.88
24	CH ₃ CONH	pyrrolidino	CO ₂ CH ₃	CH ₃	-1.16	-1.10	-1.13
25	CH ₃ CONH	aziridino	CONH ₂	H	-0.99	-0.93	-0.96
26	CH ₃ CONH	H	CO ₂ CH ₃	CH ₃	-0.91	-0.85	-0.88
28	CH ₃ CONH	H	CO ₂ (CH ₂) ₂ OH	H	-1.02	-0.95	-0.99
30	CH ₃ CONH	H	CONH ₂	H	-0.88	-0.82	-0.85
31	<i>n</i> -C ₃ H ₇ CONH	H	CONH ₂	H	-0.92	-0.89	-0.91
32	NH ₂	Cl	CO ₂ CH ₃	CH ₃	-1.01	-1.01	-1.01
33	NH ₂	H	CO ₂ CH ₃	CH ₃	-1.10	-1.04	-1.07
36	NH ₂	H	CONH ₂	H	-1.09	-1.05	-1.07
37	NH ₂	H	CH ₂ OH	H	-1.11	-1.06	-1.09
38	NH ₂	H	H	H	-1.12	-1.06	-1.09
39	H	H	H	H	-0.88	-0.85	-0.87

^a *E*_{1/2} values (± 0.005 V) calculated as (*E*_{pc} + *E*_{pa})/2 are averages of the values determined from voltammograms recorded at potential sweep rates of 50, 100, 200, 300, 400 and 500 mV/s; *E*_{pc} = cathodic peak potential; *E*_{pa} = anodic peak potential.

good substrates for NQO1.⁵⁴ Dipyrroloimidazobenzimidazole compounds with both pyrrolo rings bearing bulky substituents were determined to be poor substrates for NQO1 due to steric interactions with residues of the NQO1 active site.⁵⁵

Comparison of analogues **32** vs **33** and **25** vs **30** determined that 6-unsubstituted (R²) lavendamycin analogues are far better substrates for NQO1 than the corresponding 6-substituted counterparts (Table 5). This is likely due to active site constraints and steric effects caused by substituents that hinder entrance or proper positioning of the 5,8-dione moiety of the analogues toward the key residues of the active site and the FAD isalloxazine ring for hydride ion reception and quin-

one reduction. This finding is consistent with other studies that previously showed that increased bulkiness of the substituents at C5 position on **64** (EO9), 3-hydroxy-5-aziridinyl-1-methyl-2-(1*H*-indole-4,7-dione)-propenol,⁵⁶ dramatically reduced rates of reduction by NQO1.^{25,52} Another study determined that indolequinones and mitosenes with bulky amine substituents at C5 and C7 positions, respectively, are not substrates for NQO1 due to steric effects.⁴⁹

A number of substituents at the 2'-position of the fused indolopyridine moiety (R³) were also investigated. Among the analogues that shared an NH₂ group at the R¹ position and had no substituent at R², 2'-CH₂OH derivative (**37**) was the best substrate followed by the

Table 5. Metabolism of Lavendamycin Analogues by Recombinant Human NQO1 Monitored by Spectrophotometric Cytochrome *c* Assay

no.	R ¹	R ²	R ³	R ⁴	metabolism by NQO1 ($\mu\text{mol}/\text{min}/\text{mg}$) (cytochrome <i>c</i> reduction)
14	CH ₃ CONH	H	H	H	2.7 ± 1.2
15	CH ₃ CONH	H	CO ₂ CH ₃	H	0.9 ± 0.2
16	CH ₃ CONH	H	CO ₂ C ₄ H ₉ - <i>n</i>	H	8.6 ± 2.6
17	CH ₃ CONH	H	CO ₂ C ₅ H ₁₁ - <i>n</i>	H	9.2 ± 6.6
18	CH ₃ CONH	H	CO ₂ C ₅ H ₁₁ - <i>i</i>	H	35.4 ± 6.9
19	CH ₃ CONH	H	CO ₂ C ₆ H ₁₃ - <i>n</i>	H	11.7 ± 5.3
20	CH ₃ CONH	H	CO-piperidino	H	15.2 ± 11.5
21	CH ₃ CONH	H	CO-morpholino	H	7.5 ± 1.5
23	ClCH ₂ CONH	H	CO ₂ C ₅ H ₁₁ - <i>i</i>	H	9.9 ± 5.6
24	CH ₃ CONH	pyrrolidino	CO ₂ CH ₃	CH ₃	1 ± 1
25	CH ₃ CONH	aziridino	CONH ₂	H	0.2 ± 0.2
26	CH ₃ CONH	H	CO ₂ CH ₃	CH ₃	1.9 ± 1.7
27	CH ₃ CONH	H	CO ₂ C ₈ H ₁₇ - <i>n</i>	H	1.5 ± 0.8
28	CH ₃ CONH	H	CO ₂ (CH ₂) ₂ OH	H	11.0 ± 2.5
29	CH ₃ CONH	H	CO ₂ (CH ₂) ₂ OPO ₃ H ₂	H	15.4 ± 0.9
30	CH ₃ CONH	H	CONH ₂	H	33 ± 12
31	<i>n</i> -C ₃ H ₇ CONH	H	CONH ₂	H	0.1 ± 0.1
32	NH ₂	Cl	CO ₂ CH ₃	CH ₃	0.9 ± 0.8
33	NH ₂	H	CO ₂ CH ₃	CH ₃	21 ± 12
34	Br	H	CO ₂ CH ₃	CH ₃	0.7 ± 0.3
35	NH ₂	H	CO ₂ C ₈ H ₁₇ - <i>n</i>	H	106 ± 15
36	NH ₂	H	CONH ₂	H	18.3 ± 13.6
37	NH ₂	H	CH ₂ OH	H	263 ± 30
38	NH ₂	H	H	H	24.0 ± 6.5
39	H	H	H	H	3.4 ± 1.2

2'-CO₂C₈H₁₇-*n* derivative (**35**) (Table 5). Molecular modeling demonstrated that the CH₂OH group at R³ was capable of hydrogen bond formation with the key residues of the NQO1 active site and therefore could be an important contributing factor to substrate specificity. A CH₂OH group at the C6 position of a series of substituted 1,4-naphthoquinones also contributed the most to substrate specificity for NQO1.⁵⁴ Phillips et al. determined that some of the good indolequinone substrates for NQO1 including **64** possessed a CH₂OH group at the analogous C3 position.⁵² Furthermore, **63**, which is an excellent substrate for NQO1, possesses a CH₂OH group at C3 position.^{7,53}

Addition of NH₂ and CH₂OH groups at R¹ and R³ positions, respectively, had the greatest positive impact on substrate specificity compared to other substituents at these positions. The best substrate was the 2'-CH₂-OH-7-NH₂ derivative (**37**) with a reduction rate of 263 ± 30 $\mu\text{mol}/\text{min}/\text{mg}$ NQO1 (Table 5). These findings enhance our understanding of the relationship between lavendamycin structure and rates of reduction by NQO1.

Cytotoxicity studies were also performed on representative lavendamycins with cell survival being determined by colorimetric MTT and clonogenic assays. We used the BE human colon adenocarcinoma cells stably transfected with human NQO1 cDNA.⁵³ The BE cells (BE-WT) had no measurable NQO1 activity whereas activity in the transfected cells (BE-NQ) was greater than 660 nmol/min/mg total cell protein using dichlorophenolindophenol as the standard electron acceptor.

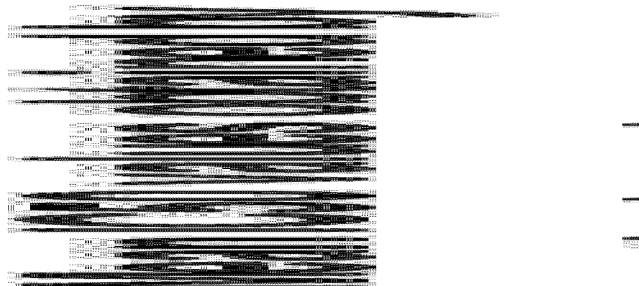
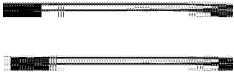


Figure 1. Correlation of mean IC₅₀ values obtained by the MTT and clonogenic assays. The mean IC₅₀ values obtained by the MTT assay were plotted along the horizontal axis and mean IC₅₀ values obtained by the clonogenic assay were plotted along the vertical axis. The correlation coefficient was 0.990 ($P = 0.0001$).

We also evaluated the correlation between the chemosensitivity results of clonogenic and MTT assays in both cell lines for three lavendamycin analogues, **31**, **33**, and **37**. There was an excellent positive linear correlation between the IC₅₀ values of the two assays for the three lavendamycins for BE-WT ($r = 0.999$, $P = 0.03$), BE-NQ ($r = 0.999$, $P = 0.025$) and both cell lines ($r = 0.990$, $P = 0.0001$) (Figure 1). In this study the cytotoxicity of representative lavendamycin analogues (Table 6) has been compared using these cell lines.

Table 6. Cytotoxicity of Lavendamycin Analogues toward BE-WT (NQO1-deficient) and BE-NQ (NQO1-rich) Human Colon Adenocarcinoma Cell Lines


no.	R ¹	R ²	R ³	R ⁴	cytotoxicity IC ₅₀ (μM)		selectivity ratio [IC ₅₀ (BE-WT)/IC ₅₀ (BE-NQ)]
					BE-NQ	BE-WT	
16	CH ₃ CONH	H	CO ₂ C ₄ H ₉ - <i>n</i>	H	20.5 ± 0.6	20.0 ± 2.3	1.0
26	CH ₃ CONH	H	CO ₂ CH ₃	CH ₃	13.2 ± 0.7	19.3 ± 4.3	1.5
27	CH ₃ CONH	H	CO ₂ C ₈ H ₁₇ - <i>n</i>	H	>50	>50	-
29	CH ₃ CONH	H	CO ₂ (CH ₂) ₂ OPO ₃ H ₂	H	6.8 ± 0.6	8.1 ± 0.5	1.2
30	CH ₃ CONH	H	CONH ₂	H	0.8 ± 0.0	3.5 ± 0.7	4.4
31	<i>n</i> -C ₃ H ₇ CONH	H	CONH ₂	H	21.4 ± 1.2	>50	2.3
33	NH ₂	H	CO ₂ CH ₃	CH ₃	0.5 ± 0.1	4.7 ± 0.7	9.4
34	Br	H	CO ₂ CH ₃	CH ₃	>50	>50	-
35	NH ₂	H	CO ₂ C ₈ H ₁₇ - <i>n</i>	H	3.4 ± 0.7	35.0 ± 3.4	10.3
36	NH ₂	H	CONH ₂	H	0.2 ± 0.0	1.8 ± 0.1	9.0
37	NH ₂	H	CH ₂ OH	H	0.4 ± 0.1	4.5 ± 0.2	11.3
38	NH ₂	H	H	H	8.0 ± 0.5	16.8 ± 1.0	2.1
39	H	H	H	H	12.4 ± 1.0	9.3 ± 1.2	0.8

Lavendamycin analogues such as **30**, **33**, **35**, **36**, and **37** that were good substrates for NQO1 (Table 5) were also more toxic to the NQO1-rich cell line (BE-NQ) than the NQO1-deficient cell line (BE-WT) (Table 6). Compound **37**, the best substrate for NQO1 (Table 5), had the greatest differential toxicity with a selectivity ratio of 11 (Table 6). Antitumor and antiproliferative activity of lavendamycin against implanted leukemia cells in BDF1 mice and three other cancer cell lines has been previously reported.^{30,57} A recent study investigating cytotoxic activities of a series of lavendamycin analogues against A549 human lung carcinoma cells indicated that compounds with an amide or amine substituent at the R³ position displayed the most potent colony formation inhibitory effects.³⁶ At a concentration of 10 nM, the most potent compound of this group, MB-97, reduced the colony outgrowth of A549 cells by 70%.³⁶ Since MB-97 also displayed promising cytotoxic and antitumor activities in the NCI's 60-cell line panel and in vivo hollow fiber tumorigenesis assay, it has been considered for in vivo testing against tumor xenografts in mice.³⁶ Our study also determined that compound **36** (MB-97) showed highly selective toxicity toward BE-NQ cells (selectivity ratio = 9). Lavendamycin analogues such as **26**, **27**, **31**, **34**, and **39** that were poor substrates for NQO1 demonstrated no selective toxicity toward BE-NQ cells or had no measurable cytotoxicity (IC₅₀ > 50 μM) (Table 6). Although compound **38** was a rather good substrate for NQO1, it displayed only minimal selective toxicity toward BE-NQ cells. This could be due to the less toxic nature of **38** (high IC₅₀ values for both cell lines) compared to other good substrates such as **30**, **33**, and **36** that have lower IC₅₀ values (Table 6). Overall, our results determined that the best lavendamycin substrates for NQO1 were also the most selectively toxic to the high NQO1 BE-NQ cell line.

Molecular Modeling. Computational and comparative molecular modeling studies were performed on two lavendamycin analogues, **31** and **37**, very poor and good substrates of NQO1, respectively. The molecular model-

Table 7. Number of Poses of Ligands **31** and **37** in Each Score Group of CSCORE Function

no.	31					37						
CSCORE	0	1	2	3	4	5	0	1	2	3	4	5
number of poses	18	8	-	-	4	-	3	3	1	4	15	4

ing was performed using SYBYL 6.9.1 software suite⁵⁸ (Tripos, Inc.; St. Louis, MO). Flexible docking was performed using the FlexX module of SYBYL that is capable of determining 30 possible conformations (poses) for each docked ligand.^{59,60} Compound **65** (ARH019), 3-(hydroxymethyl)-5-(2-methylaziridin-1-yl)-1-methyl-2-phenylindole-4,7-dione,⁴⁹ has been suggested as an appropriate model for molecular docking studies of other compounds such as streptonigrin (**2**).²⁵ Therefore, the coordinates of the crystal structure of the human NQO1 complex with bound FAD and **65**, obtained from the Protein Data Bank (PDB ID code: 1H69²⁵), were used as a composite reference structure for the docking experiments, wherein the coordinates of **65** served as the reference ligand of location. The docked conformations of ligands **31** and **37** were evaluated and ranked using FlexX and four scoring functions implemented in the CSCORE module in SYBYL. CSCORE is the consensus score computed from FlexX and ChemScore,⁶¹ D-Score,⁶² G-Score⁶³ and PMF-Score⁶⁴ scoring functions, in which docked poses are evaluated and ranked from 0 to 5; where 5 is the best fit to the model. Table 7 displays the number of conformations of ligands **31** and **37** in each score group of CSCORE function.

Ligand **37** possessed a higher number of poses with more optimal CSCORE values compared to **31** (Table 7). To minimize the number of false positives and/or negatives, visual screening of the binding orientations of the poses and geometric post-docking analyses were performed. The analyses included distance measurements, calculations, and pose geometries that determined (a) hydrogen-bonding interactions of the ligand poses with key residues of the NQO1 active site including Tyr-126, -128, and His-161, (b) hydride ion transfer

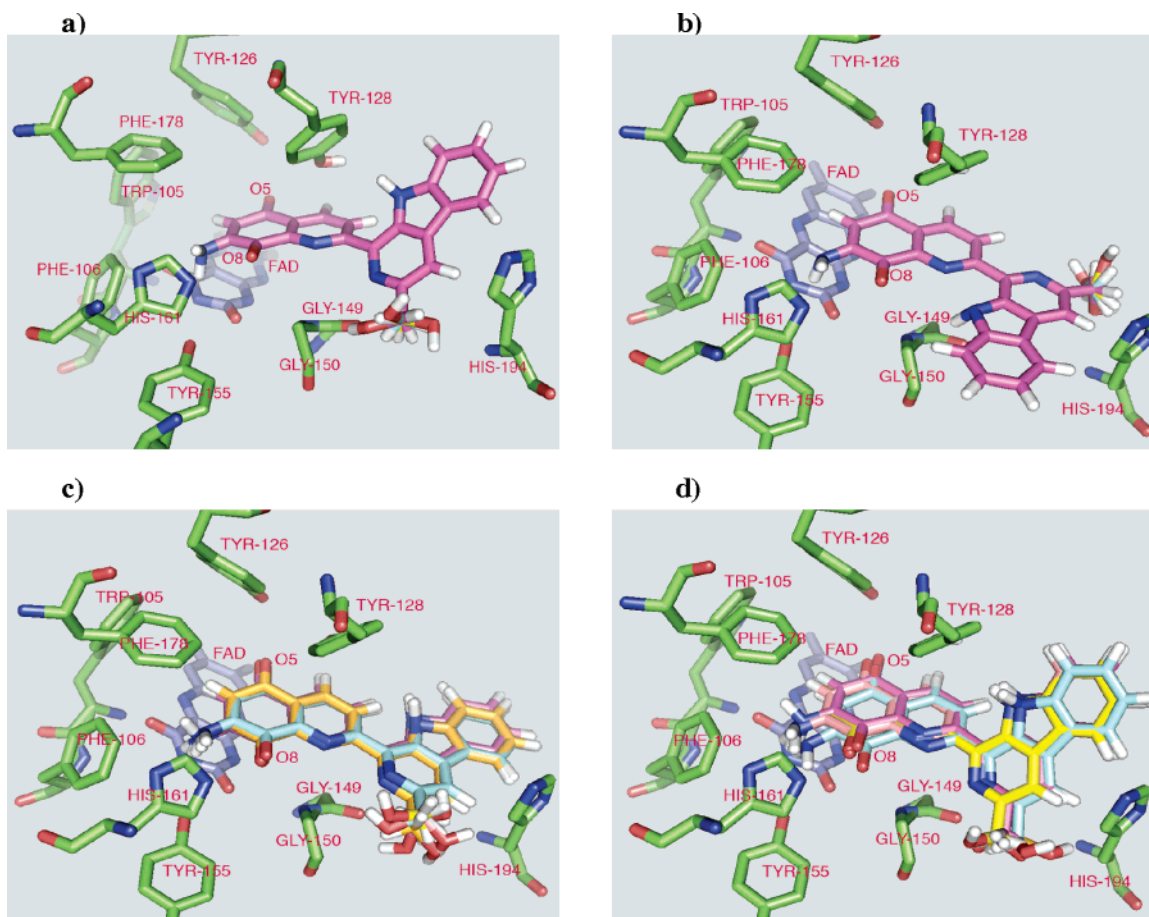


Figure 2. (a) View of the superposition of the docked poses 1,9 and 15 of **37** (magenta, cyan, and yellow) (CSCOREs = 5, 4, and 4) in NQO1 active site (RMSD = 0 Å). (b) View of the superposition of the docked poses 20, 24, and 27 of **37** (magenta, cyan, and yellow) (CSCOREs = 4) in NQO1 active site (RMSD = 0 Å). (c) View of the superposition of the docked poses 3, 4, 5, 6, 7, 11, and 12 of **37** (magenta, cyan, yellow, salmon, blue, orange and green) (CSCOREs = 4) in NQO1 active site (RMSD < 0.8 Å). (d) View of the superposition of the docked poses 8, 10, 18, 19, and 26 of **37** (yellow, salmon, magenta, cyan, and orange) (CSCOREs = 5, 5, 4, 4, and 4) in NQO1 active site (RMSD < 0.8 Å). Residues of the active site (lime), FAD (blue), and **37** represented as stick models. The atoms are colored: red, oxygen atoms; blue, nitrogen atoms; and white, hydrogen atoms.

from N5 of the FAD isoalloxazine ring to the ligands at either carbonyl oxygens (O5 or O8) or at a ring carbon, and (c) the angle between the quinone-moiety plane of the ligands and the FAD isoalloxazine ring (residue numbers in this paper are those used in the Protein Data Bank coordinates, PDB ID code: 1H69²⁵).

Of the 30 possible docked conformations of ligand **37**, 24 poses (CSCORE \geq 2) showed binding orientations similar to that of the reference ligand. Compound **65** has been shown to enter the active site by the 4,7-dione moiety where the plane of the indolequinone forms a partial aromatic-ring parallel stacking with the FAD isoalloxazine ring and the corresponding plane-to-plane angle is 16°. ²⁵ The binding orientation of **65** and ligands **31** and **37** in the NQO1 active site were similarly determined by the atomic positioning of quinone carbonyl oxygens and atoms toward the isoalloxazine ring atoms of the FAD and residues of the active site. Compound **65** carbonyl oxygen O4 in comparison to O7 is positioned closer to Tyr-126, -128 and N5 of the FAD. ²⁵ 19 poses of ligand **37** had CSCORE \geq 4 (Table 7). Poses with CSCORE \geq 4 fell into four clusters, where a cluster is defined as a group of poses that gives a root-mean-square (RMS) deviation less than 0.8 Å for the quinolinedione and indolopyridine moieties atoms. Poses 1, 9, and 15 (Figure 2a) and 20, 24, and 27 (Figure 2b)

fell into two clusters in which the RMS deviation of the poses equaled zero and the difference was in the binding orientation of the CH₂OH group in NQO1 active site (Figures 2a and 2b). Poses 3, 4, 5, 6, 7, 11, and 12 (Figure 2c) and 8, 10, 18, 19, and 26 (Figure 2d) were clustered into two groups that yielded RMS deviations of < 0.8 Å. All of the clustered poses of **37** entered the active site by the 5,8-dione moiety similar to **65**, where the departure of the planes of most of these poses from a complete aromatic-ring parallel stacking with the FAD isoalloxazine ring closely resembled that of **65** (Figure 2). Carbonyl oxygen O5 of the clustered poses compared to O8 was positioned closer to Tyr-126, -128, and the FAD N5 resembling compound **65** binding orientation, suggesting that this could be the preferred binding orientation for ligand **37** (Figure 2).

In the NQO1 active site, the hydroxyl groups of Tyr-126 and -128 and/or N or NH of His-161 can form hydrogen bonds with carbonyl oxygens and/or other atoms of quinone substrates. ^{10,25,27} One crucial determining factor of quinone substrates binding strength in the NQO1 active site is the quinone oxygens' capability of forming hydrogen-bonding interactions with Tyr-126 and -128. ²⁷ Good substrates for NQO1 such as **63** and **64** are capable of hydrogen-bonding interactions with the key residues of the NQO1 active site. ^{6,25} Among

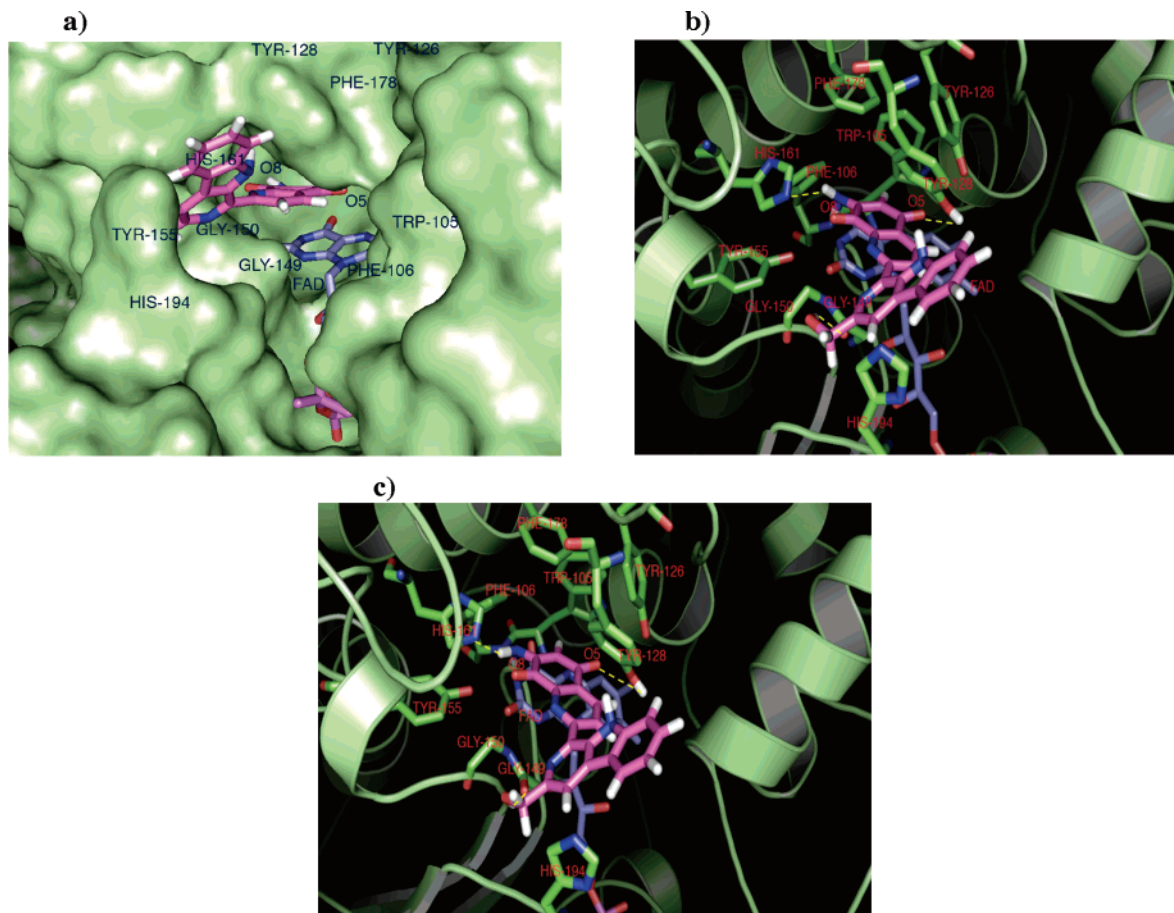


Figure 3. (a) Depiction of the molecular surface of NQO1 active site region. The surface of the pocket is colored lime with FAD (blue) and the docked pose 1 of **37** (magenta) (CSCORE = 5) represented as stick models. (b) Molecular model of the pose 1 of **37** docked into NQO1 active site. (c) Molecular model of the pose 2 of **37** (CSCORE = 5) docked into NQO1 active site. In b and c, residues of the active site (lime), FAD (blue), and **37** (magenta) represented as stick models and the rest of the structure as a secondary structure cartoon. The atoms are colored: red, oxygen atoms; blue, nitrogen atoms; and white, hydrogen atoms. Hydrogen bonds are represented as yellow dashed lines.

the poses of ligand **37**, poses 1 and 2 formed the highest number of efficient hydrogen bonds in the active site of the enzyme. The 5,8-dione moiety of pose 1 with CSCORE = 5 stacked over the isoalloxazine ring of the FAD and the NH₂ group at the quinolinedione 7-position was placed close to His 161 (Figures 3a and 3b). The fused three-ring indolopyridine moiety pointed toward the outside of the active site. The CH₂OH group at the indolopyridine 2'-position was placed close to Gly-149 (Figures 3a and 3b). Pose 2 (CSCORE = 5) also positioned in the NQO1 active site in a very similar way to pose 1 (Figure 3c). The carbonyl oxygen O5 of ligand **37** poses 1 and 2 formed a hydrogen bond with the Tyr-128 OH and one hydrogen atom of the NH₂ substituent formed a hydrogen bond with N of His 161. The CH₂-OH group of the indolopyridine moiety further stabilized the binding by making a hydrogen bond to the carbonyl oxygen of the Gly-149 (Figures 3b and 3c). Poses 1 and 2 of ligand **37** with high CSCOREs of 5 made the most efficient hydrogen-bonding interactions and had the most favorable binding orientation for efficient hydride ion reception and quinone reduction.

However, of the 30 possible docked conformations of ligand **31**, no conformation had a CSCORE = 5 (Table 7). None of the 30 poses had a binding orientation similar to that of the reference ligand, **65**. Pose 12 with CSCORE = 4 had a binding orientation opposite that

of the original reference (Figure 4a). Neither of the carbonyl oxygens O5 and O8 of pose 12 were capable of forming hydrogen bonds with the key residues of the active site unlike poses 1 and 2 of ligand **37** (Figure 4a). The other 3 poses (11, 26, and 28) of **31** with CSCORE = 4 entered the active site of NQO1 with the fused three-ring indolopyridine moiety where the quinolinedione moiety pointed toward the outside of the active site (Figures 4b and 4c). Compound **66** (ES1340), 5-methoxy-3-(phenyloxymethyl)-1,2-dimethylindole-4,7-dione,¹⁸ which is a poor substrate for NQO1⁵⁰ has been shown to position in the NQO1 active site such that the 4,7-dione moiety points to the outside of the active site.²⁶ The binding orientations of the poses of ligand **31** were not favorable for effective hydrogen-bonding interactions, hydride ion reception, or quinone reduction. The remaining 26 poses with CSCOREs of 0 and 1 did not merit further considerations.

The molecular modeling and docking studies demonstrated that ligand **37** possessed an increased number of possible poses with favorable binding orientations to promote efficient hydrogen bonding interactions, hydride ion reception and quinone reduction compared to **31**. Ligand **37** due to the small hydrogen bond forming substituents possessed structural characteristics for favorable positioning in the NQO1 active site for reduction. Conversely, the unfavorable structural character-

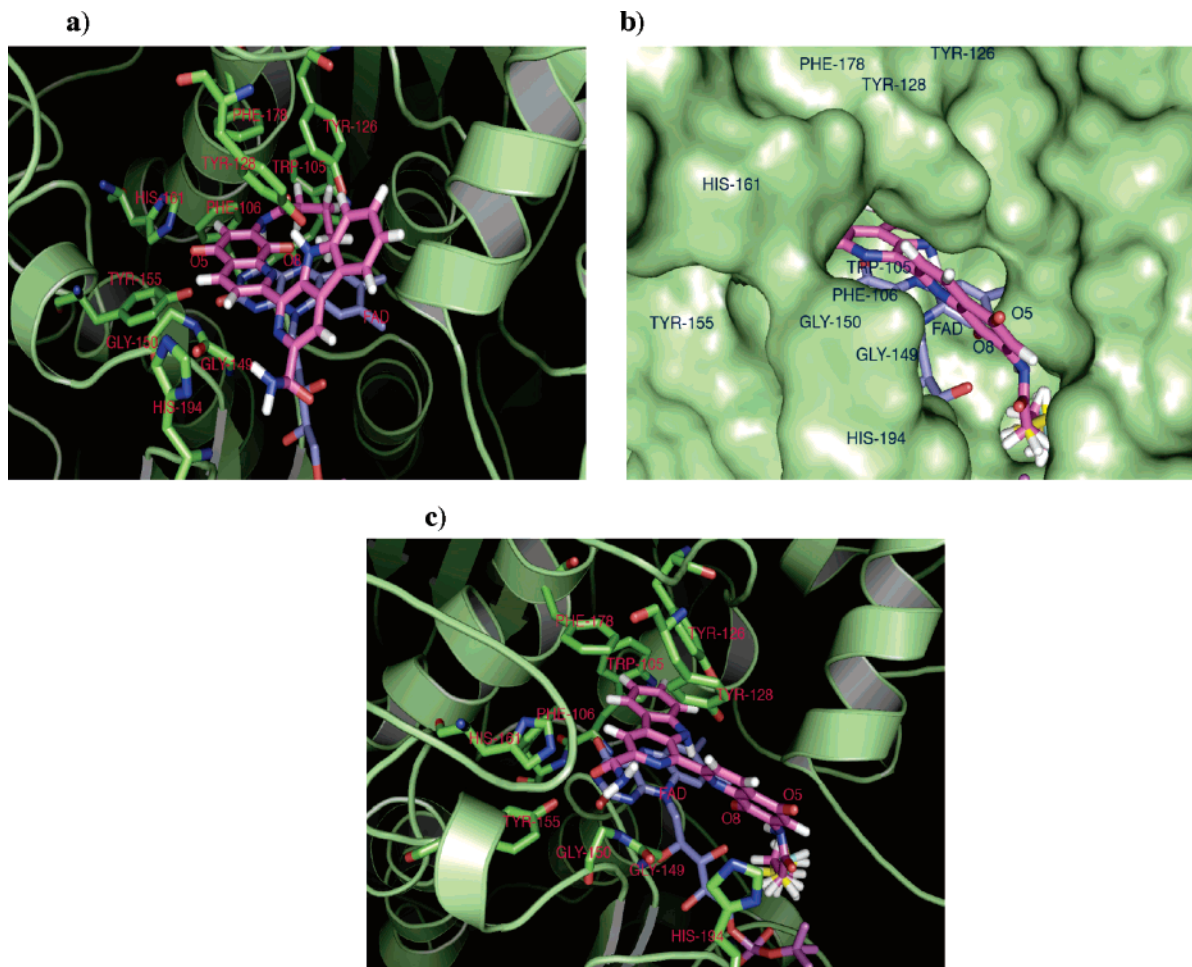


Figure 4. (a) Molecular model of the pose 12 of **31** (CSCORE = 4) docked into NQO1 active site. Residues of the active site (lime), FAD (blue), and **31** (magenta) represented as stick models and the rest of the structure as a secondary structure cartoon. (b) Depiction of the molecular surface of NQO1 active site region. The surface of the pocket is colored lime with FAD (blue) and the docked poses 11, 26, and 28 of **31** (magenta, yellow and cyan) (CSCOREs = 4) represented as stick models. (c) Molecular model of the poses 11, 26, and 28 of **31** docked into NQO1 active site. Residues of the active site (lime), FAD (blue), and **31** (magenta, yellow, and cyan) represented in stick models and the rest of the structure as a secondary structure cartoon. The atoms are colored: red, oxygen atoms; blue, nitrogen atoms; and white, hydrogen atoms.

istics of ligand **31** could exclude it from proper positioning in the NQO1 active site for reduction. These findings suggest that active site positioning contributes to the much greater substrate specificity observed for ligand **37** than ligand **31**.

Conclusions. A number of novel lavendamycin analogues were synthesized through short and practical methods. No direct correlation between the reduction potential and rate of reduction of the analogues by NQO1 were found suggesting the more important role of steric effects of these compounds in the NQO1 active site rather than electronic effects on the reduction efficiency by NQO1. Small substituents at R¹ and R³ positions on the quinonolinedione moiety of the lavendamycin analogues were well tolerated whereas absence of a substituent at R² was preferred. Addition of NH₂ and CH₂OH groups at R¹ and R³ positions, respectively, displayed the greatest positive impact on substrate specificity such that 2'-CH₂OH-7-NH₂ derivative (**37**) exhibited the highest reduction rate. The best lavendamycin substrates for NQO1 were also the most selectively toxic to the NQO1-rich BE-NQ cell line. The docking studies supported a model in which the good lavendamycin substrate **37** was capable of efficient

hydrogen-bonding interactions with the key residues of the NQO1 active site and hydride ion reception from FAD while the poor substrate **31** was not. The use of molecular modeling techniques can greatly contribute to future rational design of good NQO1 substrates for NQO1-directed lavendamycin antitumor agent development.

Experimental Section

Chemistry. General Methods. For General Methods see ref 38 (*J. Med. Chem.* **2003**, *46*, 5773–5780). Aziridine was prepared according to the procedure previously described by Allen et al.⁶⁵ and was kept in a refrigerator over KOH pellets.

Bis(chloroacetamido)-8-hydroxy-2-methylquinoline (50). In a 500 mL heavy-walled hydrogenation bottle, 5.25 g (0.21 mol) of finely ground 8-hydroxy-2-methyl-5,7-dinitroquinoline (**47**) and 1.75 g of palladium on charcoal were suspended in a mixture of 90 mL of water and 9 mL of concentrated hydrochloric acid.⁴¹ In a Parr Hydrogenator, this mixture was shaken under 30 psi of hydrogen for 20 h. The catalyst was filtered off, and the dark red solution containing the dihydrochloride salt of 5,7-diamino-8-hydroxy-2-methylquinoline was placed in a 250 mL round-bottomed flask with a magnetic bar. To this stirred solution was added in sequence as quickly as possible 12 g of sodium sulfite, 16 g of sodium acetate, and 65 g of chloroacetic anhydride. Heat was evolved with formation

of a light colored precipitate which was dissolved after 15 min. The solution gave a precipitate after stirring for 1 h. This mixture was poured into 100 mL of ice-water mixture and stirred for 5 min and then filtered. The product was washed with 10 mL of cold ethanol and filtered. The filtrate upon standing overnight gave more of the product. The total weight of the product was 3.61 g (50%). It was recrystallized from ethanol-water: mp 194–196 °C; $^1\text{H NMR}$ (DMSO- d_6) δ 2.71 (s, 3H), 4.37 (s, 2H), 4.44 (s, 2H), 7.43 (d, 1H, $J = 8.8$), 8.15 (d, 1H, $J = 8.8$), 8.16 (s, 1H), 9.89 (br s, 1H), 10.18 (br s, 1H); EIMS, m/z , 341/343 (M^+ 1.5/1, 52), 305 (60), 292 (base), 264 (28), 228 (60), 188 (70), 160 (17); HRMS calculated for $\text{C}_{14}\text{H}_{13}\text{Cl}_2\text{N}_3\text{O}_3$ 341.033397, found 341.033888; Elemental analysis: calculated for C, 49.14; H, 3.83; Cl, 20.72; N, 12.28, found C, 49.24; H, 3.89; Cl, 20.43; N, 12.6.

7-Chloroacetamido-2-methylquinoline-5,8-dione (41).

In a 500 mL round-bottomed flask, equipped with a magnetic bar, 5,7-bis(chloroacetamido)-8-hydroxy-2-methylquinoline (3.42 g, 0.01 mol) was suspended in 122 mL of glacial acetic acid. To this, a solution of potassium dichromate (8.8 g, 0.03 mol) in 115 mL of water was added and stirred overnight at room temperature. The solution was extracted with dichloromethane (12 \times 50 mL). The organic extracts were washed with 200 mL of sodium bicarbonate solution, dried with magnesium sulfate, and then evaporated under reduced pressure to give a bright yellow solid (1.56 g, 59%). Recrystallization from ethyl acetate gave the pure product: mp 196–200 °C (dec); $^1\text{H NMR}$ (CDCl_3) δ 2.76 (s, 3H), 4.23 (s, 2H), 7.56 (d, 1H, $J = 8.1$), 7.89 (s, 1H), 8.30 (d, 1H, $J = 8.1$), 9.48 (br s, 1H); EIMS, m/z , 264/266 (M^+ 2.9/1), 229 (62), 215 (74), 201 (43), 188 (86), 161 (base), 132 (21); HRMS calculated for $\text{C}_{14}\text{H}_9\text{ClN}_2\text{O}_3$ 264.03107 found 264.029824; Elemental analysis calculated for C, 54.19; H, 3.43; Cl, 13.40; N, 10.58, found C, 54.19; H, 3.37; Cl, 13.29; N, 10.36.

7-Chloroacetamido-2-formyl-5,8-quinolinedione (4).

In a 25 mL round-bottomed flask, equipped with a magnetic bar, water-cooled reflux condenser, and argon-filled balloon, dione **41** (0.529 g, 2 mmol), selenium dioxide (0.332 g, 3 mmol), 12 mL of dried distilled dioxane, and 0.25 mL of water were stirred and slowly heated to reflux over a 2 h period. To complete the reaction, the mixture was refluxed for 17 h (TLC). An additional 10 mL of dioxane was added and refluxed for 10 min and then filtered off hot. The filter cake was placed in a round-bottomed flask, and 10 mL of dichloromethane was added and refluxed for 10 min and then filtered. The filtrates were combined and then evaporated to dryness under reduced pressure. The solid residue was dissolved in 50 mL of dichloromethane, placed in a separatory funnel, and washed with 3% sodium bicarbonate solution. The aqueous layers were extracted with 3 \times 50 mL of dichloromethane and the combined organic layers were dried (MgSO_4) and evaporated to give 0.25 g (45%) of a yellow product: mp 190–192 °C; $^1\text{H NMR}$ (CDCl_3) δ 4.26 (s, 2H), 8.04 (s, 1H), 8.33 (d, 1H, $J = 8.1$), 8.62 (d, 1H, $J = 8.1$), 9.54 (br s, 1H), 10.28 (s, 1H); EIMS, m/z , 278/280 (M^+ 2.7/1, 95), 243 (33), 229 (33), 215 (55), 202 (base), 175 (61); HRMS calculated for $\text{C}_{14}\text{H}_9\text{ClN}_2\text{O}_3$ 278.009435, found 278.00876.

Tryptophan *n*-Pentyl Ester (8). This ester was prepared according to the method used for the preparation of **9** in 80% yield as a thick yellow oil. $^1\text{H NMR}$ (CDCl_3) δ 0.89 (t, 3H, $J = 6.6$), 1.1–1.3 (m, 2H), 1.4–1.7 (m, 4H), 2.9–3.7 (m, 2H), 3.70–3.80 (m, 1H), 4.02 (t, 2H, $J = 6.7$), 6.98 (s, 1H), 7.01–7.2 (m, 2H), 7.22 (d, 1H, $J = 7.6$), 7.56 (d, 1H, $J = 7.6$), 8.14 (br s, 1H); HRMS calculated for $\text{C}_{16}\text{H}_{22}\text{N}_2\text{O}_2$ (M^+) 274.1676, found 274.1678.

Tryptophan Isoamyl Ester (9). Isoamyl alcohol was dried over anhydrous cupric sulfate for 24 h and then distilled under argon. Tryptophan (1.43 g, 7 mmol) was placed in a 100 mL round-bottomed flask along with 60 mL of the dried isoamyl alcohol and 10 mL of HCl/ether solution. The solution was refluxed in an oil bath for 22 h. The mixture was then rotaevaporated to dryness. A portion of the resulting tryptophan isoamyl ester hydrochloride (723 mg, 2.84 mmol) was suspended in 36 mL of ethyl acetate. To this stirred suspen-

sion, a 14% solution of ammonium hydroxide (~3 mL) was added until the aqueous layer was at pH = 8. The aqueous layer was separated, and the organic layer was washed with a saturated sodium chloride solution (3 \times 2 mL) and water (2 mL) and dried over magnesium sulfate. The solution was filtered and rotaevaporated to dryness. The thick liquid was further dried under a vacuum pump at 50–60 °C for 2 days. The total weight of the product was 1.6 g (83%): mp 50 °C (Dec.); $^1\text{H NMR}$ (CDCl_3) δ 0.90 (d, 6H, $J = 6.3$), 1.60 (m, 4H), 2.99–3.22 (m, 2H), 3.81 (m, 1H), 4.10 (t, 2H, $J = 6.7$), 7.00 (s, 1H), 7.10 (m, 1H), 7.20 (m, 1H), 7.33 (d, 1H, $J = 7.6$), 7.59 (d, 1H, $J = 7.3$), 8.08 (br s, 1H); HRMS calculated. For $\text{C}_{16}\text{H}_{22}\text{N}_2\text{O}_2$ (M^+) 274.1676, found 274.1676.

Tryptophan *n*-Hexyl Ester (10). Ester **10** was prepared by a similar method as that for ester **9** in 87% yield as thick oil. $^1\text{H NMR}$ (CDCl_3) δ 0.89 (t, 3H, $J = 7.0$), 1.20–1.40 (m, 4H), 1.50–1.75 (m, 4H), 2.90–3.40 (m, 2H), 3.78–3.90 (m, 1H), 4.1 (t, 2H, $J = 7.0$), 7.09 (s, 1H), 7.16–7.25 (m, 2H), 7.37 (d, 1H, $J = 8.0$), 7.64 (d, 1H, $J = 6.6$), 8.12 (br s, 1H); HRMS calculated for $\text{C}_{17}\text{H}_{24}\text{N}_2\text{O}_2$ (M^+) 288.1832, found 288.1824.

N-Carbobenzyloxytryptophan Succinimide Ester (60).

In a 100 mL round-bottomed flask equipped with a magnetic bar and an argon-filled balloon, *N*-carbobenzyloxytryptophan (2.132 g, 6.3 mmol), *N*-hydroxysuccinimide (0.725 g, 6.3 mmol), and 50 mL dried, distilled dioxane were placed. The reaction mixture was stirred until a clear solution was obtained, the flask was kept in a cold-water bath at 12 °C (dioxane freezes at 11 °C), and *N*-dicyclohexylcarbodiimide (1.3 g, 6.3 mmol) was added. A white precipitate was immediately formed. The mixture was stirred at 15–20 °C for 2 h and then at room temperature for another 2 h. The mixture was allowed to stand in refrigerator overnight and then filtered. The solid was washed with dioxane (2 \times 3 mL). The filtrate was rotaevaporated to a thick liquid and then kept on a vacuum pump for 3 days to give a white solid. The total weight of the product was 3.19 g (>100%). Some dioxane (shown by NMR) was still present in the product that was taken into consideration when **59** was used in the following reactions. An analytical sample was obtained by silica gel plate chromatography using EtOAc–acetone–MeOH (1:1:0.5) as the eluant. The yield of the pure product was 89%; mp 64 °C; $^1\text{H NMR}$ (CDCl_3) δ 2.73 (s, 4H), 3.42–3.50 (m, 2H), 5.07–5.17 (m, 3H), 7.07 (dd, 1H, $J = 7.0$), 7.07–7.14 (m, 1H), 7.13 (dd, 1H, $J = 8.0$), 7.17 (s, 1H), 7.34 (s, 5H), 7.54 (d, 1H, $J = 7.4$), 8.27 (br s, 1H); HRMS calculated for $\text{C}_{23}\text{H}_{21}\text{N}_3\text{O}_6$ 435.1430, found 435.1428.

N-Carbobenzyloxytryptophan Piperidine Amide (61).

In a 50 mL round-bottomed two-necked flask equipped with a magnetic bar and an argon-filled balloon, ester **60** (0.435 g, 1 mmol), piperidine (0.085 g, 1 mmol), dried distilled triethylamine (0.14 mL, 1.4 mmol), absolute ethanol (13 mL), and distilled chloroform (12 mL) were placed. The reaction mixture was stirred for 1 h at room temperature. Thin-layer chromatography showed the reaction to be completed. The mixture was evaporated under reduced pressure to give a solid. The material was dissolved in 90 mL of ethyl acetate and then washed with 30 mL of water followed by 2 \times 30 mL of 10% citric acid. The solution was washed with 15 mL 1 N sodium bicarbonate, then 5 mL of water, dried (Na_2SO_4), and evaporated to give a white solid. The product was dried on a vacuum pump at 60 °C for 2 days yielding 0.32 g (80%) of the product **61**: mp 64–64.5 °C; $^1\text{H NMR}$ (CDCl_3) δ 0.76–1.40 (m, 6H), 2.85–3.39 (m, 4H), 3.38–3.40 (m, 2H), 4.99–5.05 (m, 1H), 5.11 (s, 2H), 5.88 (s, 1H), 6.98 (s, 1H), 7.13 (t, 1H, $J = 7.7$), 7.17 (t, 1H, $J = 6.7$), 7.18 (d, 1H, $J = 6.7$), 7.34 (s, 5H), 7.62 (d, 1H, $J = 7.7$), 8.22 (br s, 1H); HRMS calculated for $\text{C}_{24}\text{H}_{27}\text{N}_3\text{O}_3$ 405.2047, found 405.2048.

Tryptophan Piperidine Amide (11). In a 50 mL two-necked round-bottomed flask equipped with a magnetic bar and an argon-filled balloon, amide **61** (0.65 g, 1.6 mmol) was suspended in 30 mL of distilled methanol. To this mixture dry ammonium formate (0.298 g, 4.73 mmol) and 0.298 g of 10% Pd/C were added and stirred at room temperature. Thin-layer chromatography showed the completion of the reaction in 30 min. The mixture was filtered and Pd/C was rinsed with 10

mL of methanol. The filtrate was evaporated under reduced pressure until a thick liquid with consistency and color of honey was obtained. The thick liquid was dried on a vacuum pump at 50–60 °C for 2 days. The product weighed 0.224 g, (70%): mp 172–173 °C; ¹H NMR (CDCl₃) δ 0.77–1.37 (m, 6H), 2.88–3.37 (m, 4H), 4.12 (t, 1H, *J* = 6.6), 4.73 (br s, 2H), 6.98 (d, 1H, *J* = 8.0), 7.03 (dd, 1H, *J* = 8.7, 7.6), 7.16 (s, 1H), 7.33 (d, 1H, *J* = 8.0), 7.48 (d, 1H, *J* = 7.7); HRMS calculated for C₁₆H₂₂N₃O (M + H)⁺ 272.1762, found 272.1754.

***N*-Carbobenzyloxytryptophan Morpholine Amide (62).** The procedure for the preparation of **62** was the same as that for **61** yielding 0.37 g (90%) of the honey-colored product: mp 71.5–72 °C; ¹H NMR (CDCl₃) δ 2.37–2.83 (m, 2H), 3.08–3.54 (m, 8H), 4.95–5.01 (m, 1H), 5.12 (s, 2H), 5.82 (br s, 1H), 7.04 (s, 1H), 7.08–7.23 (m, 3H), 7.35 (s, 5H), 7.65 (d, 1H, *J* = 7.2), 8.10 (br s, 1H); HRMS calculated for C₂₃H₂₅N₃O₄ 407.1840, found 407.1846.

Tryptophan Morpholine Amide (12). The procedure for the preparation of **12** was the same as that for **11** to give the product in 88% yield: mp 99–101 °C; ¹H NMR (CDCl₃) δ 1.82 (br s, 2H), 2.68–3.49 (m, 2H), 2.98–3.44 (m, 8H), 4.08 (t, 1H, *J* = 7.2), 7.09 (s, 1H), 7.17–7.21 (m, 2H), 7.58 (d, 1H, *J* = 7.0), 8.13 (br s, 1H); HRMS calculated for C₁₅H₂₂N₃O₂ (M + H)⁺ 273.1477, found 273.1476.

General Procedure for the Synthesis of Lavendamy- cins. Unless otherwise stated, lavendamyacin derivatives **14**–**23** were synthesized by the procedure described for analogue **16**. For each compound, the corresponding starting materials (Scheme 1) were mixed in the desired solvent and heated for several hours (Table 1). The completion of each reaction was monitored by TLC. Using a similar setup to that of **16**, lavendamyacins **32**, **39**, **57**, and **58** were also synthesized as described in the text.

7-*N*-Acetyldecarboxydemethylavendamyacin (14). A mixture of aldehyde **3** (70 mg, 0.29 mmol) and tryptamine **5** (50 mg, 0.31 mmol) in 180 mL of dry anisole was heated to 105 °C over a period of 2 h and then 10% Pd/C (70 mg) was added and refluxed for 17 h. The reaction mixture was filtered while hot, and the solid was washed with chloroform and then acetone. Rotaevaporation of the filtrate gave **14** as a yellow solid (91.6 mg, 83%): mp > 280 °C; *R*_f = 0.42 (Al₂O₃, 0.03/100 MeOH/CH₂Cl₂); ¹H NMR (CDCl₃) δ 2.37 (s, 3H), 7.30–7.40 (m, 1H), 7.62–7.71 (m, 1H), 7.74 (d, 1H, *J* = 8.0), 7.99 (s, 1H), 8.13 (d, 1H, *J* = 4.8), 8.21, d, 1H, *J* = 8.0), 8.45 (br s, 1H), 8.54 (d, 1H, *J* = 8.0), 8.61 (d, 1H, *J* = 4.8), 9.10 (d, 1H, *J* = 8.0), 11.64 (br s, 1H); HRMS calculated for C₂₂H₁₄N₄O₃ (M⁺) 382.1066, found 382.1069.

7-*N*-Acetyldeethylavendamyacin Methyl Ester (15). Analogue **15** was prepared according to the method used for **16**. A mixture of 0.3 mmol of each of **3** and **6** in 180 mL of dry anisole was heated (see Table 1 for temperature and time). The reaction mixture was evaporated to give a light yellow solid. The solid was washed with acetone to give 64 mg of a pure yellow product. More product (34 mg) was obtained from the filtrate (total yield, 67%): mp > 280 °C; *R*_f = 0.41 (0.01/20 MeOH/CH₂Cl₂); ¹H NMR (CDCl₃) δ 2.38 (s, 3H), 4.12 (3, 3H), 7.40 (unresolved dd, 1H, *J* = 7.6), 7.76 (unresolved dd, 1H, *J* = 7.6), 8.03 (m, 1H), 8.27 (d, 1H, *J* = 8.2), 8.48 (br s, 1H), 8.62 (d, 1H, *J* = 8.2), 9.03 (s, 1H), 9.26 (d, 1H, *J* = 8.2), 11.82 (br s, 1H); HRMS calculated for C₂₄H₁₆N₄O₅ (M⁺) 440.1120, found 440.1119.

7-*N*-Acetyldeethylavendamyacin *n*-Butyl Ester (16). In a 500 mL three-necked round-bottomed flask equipped with a Dean–Stark trap, a magnetic bar, and under an argon flow, 7-acetamido-2-formylquinoline-5,8-dione (**3**, 133 mg, 0.51 mmol) and tryptophan butyl ester (**7**, 124 mg, 0.52 mmol) were dissolved in 162 mL of dry xylene and, while being stirred, heated to reflux over a 3-h period. The yellow lemon solution was refluxed for 5 h and evaporated in vacuo, and the residue was dissolved in chloroform. The small amount of the brownish solid was removed, and the solution was concentrated to near dryness. Acetone, 2 mL, was added and the resulting solid material was filtered, washed with a small portion of acetone, and dried under vacuum. The orange solid weighed 155 mg

(63%): mp 256–257 °C; *R*_f = 0.74 (1/100 MeOH/CH₂Cl₂); ¹H NMR (CDCl₃) δ 1.05 (t, 3H, *J* = 7.0), 1.5–1.62 (m, 2H), 1.84–1.94 (m, 2H), 2.36 (s, 3H), 4.51 (t, 2H, *J* = 7.0), 7.4 (unresolved dd, 1H, *J*, *J*' = 7.3, 1H), 7.64–7.70 (m, 1H), 7.72 (d, 1H, *J* = 8.1), 7.97 (s, 1H), 8.24 (d, 1H, *J* = 8.1), 8.4 (br s, 1H), 8.53 (d, 1H, *J* = 8.4), 8.94 (s, 1H), 9.17 (d, 1H, *J* = 8.4), 11.77 (br s, 1H); HRMS (FAB) calculated for C₂₇H₂₅N₄O₅ (M + 3H)⁺ 485.1825, found 485.1827.

7-*N*-Acetyldeethylavendamyacin *n*-Pentyl Ester (17). Analogue **17** was synthesized according to the procedure used for **16** in 44% yield as an orange solid: mp 232–233 °C; *R*_f = 0.68 (1/100 MeOH/CH₂Cl₂); ¹H NMR (CDCl₃) δ 0.99 (t, 3H, *J* = 6.9), 1.40–1.80 (m, 4H), 1.8–2.0 (m, 2H), 2.35 (s, 3H), 4.48 (t, 2H, *J* = 6.6), 7.30–7.40 (m, 1H), 7.50–7.65 (m, 2H), 7.86 (s, 1H), 8.17 (d, 1H, *J* = 8.0), 8.29 (br s, 1H), 8.36 (d, 1H, *J* = 8.4), 8.89 (s, 1H), 9.02 (d, 1H, *J* = 8.4), 11.56 (br s, 1H); HRMS (FAB) calculated for C₂₈H₂₇N₄O₅ (M + 3H)⁺ 499.1981, found 499.1980.

7-*N*-Acetyldeethylavendamyacin Isoamyl Ester (18). Compound **18** was prepared according to the method similar to that of **16**. A mixture of 0.5 mmol of each of the starting materials **3** and **9** in 160 mL of dry xylene was heated to 78 °C over a period of 4 h and then heated to 125 °C over 10 min and kept at 125–130 °C for 5.5 h. The reaction mixture was allowed to cool to room temperature, and the brown solid impurity was filtered. The filtrate containing the product was concentrated to near dryness and then washed with a small amount of acetone to give 84 mg of an orange yellow solid. More product was obtained from the concentration of the filtrate (total yield, 128 mg, 50%): mp 257.5–258 °C; *R*_f = 0.64 (1/100 MeOH/CH₂Cl₂); ¹H NMR (CDCl₃) δ 1.06 (d, 6H, *J* = 6.3), 1.8–1.9 (m, 3H), 2.38 (s, 3H), 4.54 (t, 2H, *J* = 6.8), 7.35–7.45 (m, 1H), 7.63–7.80 (m, 2H), 8.01 (s, 1H), 8.27 (d, 1H, *J* = 7.7), 8.45 (br s, 1H), 8.58 (d, 1H, *J* = 8.3), 8.97 (s, 1H), 9.22 (d, 1H, *J* = 8.3), 11.80 (br s, 1H); HRMS calculated for C₂₈H₂₄N₄O₅ (M⁺) 496.1760, found 496.1756.

7-*N*-Acetyldeethylavendamyacin *n*-Hexyl Ester (19). This compound was synthesized using the method for the preparation of **16**. The orange solid was obtained in 54% yield: mp 228–230 °C; *R*_f = 0.51 (1/100 MeOH/CH₂Cl₂); ¹H NMR (CDCl₃) δ 0.94 (t, 3H, *J* = 7.0), 1.36–1.50 (m, 4H), 1.50–1.60 (m, 2H), 1.80–2.0 (m, 2H), 4.48 (t, 2H, *J* = 6.8), 7.30–7.42 (m, 1H), 7.60–7.70 (m, 2H), 7.90 (s, 1H), 8.16 (d, 1H, *J* = 8.0), 8.33 (s, 1H), 8.60 (d, 1H, *J* = 8.4), 8.87 (s, 1H), 9.07 (d, 1h, *J* = 8.4), 11.64 (s, 1H); HRMS calculated for C₂₉H₂₆N₄O₅ (M + 3H)⁺ 513.2138, found 513.2139.

7-*N*-Acetyldeethylavendamyacin Piperidine Amide (20). In a method similar to that used for the preparation of **16**, a mixture of 0.55 mmol of aldehyde **3** in 300 mL of dry anisole was heated to 70 °C, and then in a dropping funnel, a solution of 0.55 mmol of tryptophan piperidine amide in 6 mL of dry pyridine was dropwise added and heated for the required amount time (Table 1). The reaction mixture was cooled to room temperature, and the solid was filtered, washed with 10 mL of dichloromethane followed by 25 mL of ethyl acetate, and then vacuum-dried to yield 120 mg of a brown product. The filtrate was evaporated, and from the solid residue more product (34 mg) was recovered through flash chromatography using chloroform as the eluting solvent (total yield, 56%): mp 250 °C (dec); *R*_f = 0.39 (0.01/5 MeOH/CH₂Cl₂); ¹H NMR (CDCl₃) δ 1.70–1.77 (m, 6H), 2.43 (s, 3 H), 3.71–3.89 (m, 4H), 7.28–7.32 (m, 1H), 7.59–7.61 (m, 2H), 7.99 (s, 1H), 8.09 (d, 1H, *J* = 8.4), 8.32 (d, 1H, *J* = 8.4), 8.41 (s, 1H), 8.92 (d, 1H, *J* = 8.4), 11.44 (br s, 1H); HRMS calculated for C₂₈H₂₄N₅O₄ (M + H)⁺ 494.1828, found 494.1834.

7-*N*-Acetyldeethylavendamyacin Morpholine Amide (21). In a method similar to that used for the synthesis of **16**, compound **21** was synthesized according to the method used for **20** as an orange solid in a total yield of 57%: mp > 300 °C; *R*_f = 0.38 (0.03/5 MeOH/CH₂Cl₂); ¹H NMR (CDCl₃) δ 2.40 (s, 3H), 3.79–3.96 (m, 8H), 7.38–7.41 (m, 1H), 7.65–7.8 (m, 2H), 8.03 (s, 1H), 8.20 (d, 1H, *J* = 8.1), 8.5–8.65 (m, 3H), 8.97 (d, 1H, *J* = 8.3), 11.67 (br s, 1H); HRMS calculated for C₂₇H₂₄N₅O₅ (M + 3H)⁺ 498.1777, found 498.1781.

7-N-Acetyldecarydemethyl-2'-(hydroxymethyl)-lavendamyacin (22). Compound **22** was prepared by the condensation of 0.15 mmol of **3** and 0.15 mmol of **13** in 60 mL of anisole. The mixture was heated to 155 °C over a period of 4 h and then allowed to cool to room temperature. The yellow solid product was filtered, washed with acetone, and dried under vacuum (29.4 mg, 48%): mp > 280 °C; $R_f = 0.39$ (EtOAc); $^1\text{H NMR}$ (CDCl_3) δ 2.31 (s, 3H), 4.88 (d, 1H, $J = 5.9$), 5.58 (t, 1H, $J = 5.9$), 7.33–7.38 (m, 1H), 7.63–7.71 (m, 2H), 7.82 (s, 1H), 8.41 (d, 1H, $J = 7.7$), 8.54 (d, 1H, $J = 8.0$), 8.96 (d, 1H, $J = 8.0$), 10.29 (br s, 1H), 11.67 (br s, 1H); HRMS calculated for $\text{C}_{23}\text{H}_{16}\text{N}_4\text{O}_4$ (M^+) 412.1171, found 412.1175.

7-N-Chloroacetyl demethyl lavendamyacin Isoamyl Ester (23). A mixture of 0.18 mmol of **4** and 0.18 mmol of **9** in 75 mL of dry xylene was heated slowly to 76 °C over 5 h. The mixture was filtered hot to remove the impurity, and the filtrate was concentrated under reduced pressure to about 10 mL. The solution was kept in a refrigerator overnight to give a dark orange-brown solid. The solid was filtered and washed with cold ethyl acetate yielding 25 mg of the product. Further concentration of the filtrate afforded more product (total 40.5 mg, 43%): mp 280–284 °C; $R_f = 0.40$ (0.008/5 MeOH/ CHCl_3); $^1\text{H NMR}$ (CDCl_3) δ 1.05 (d, 6H, $J = 6.3$), 1.76–1.95 (m, 3H), 4.29 (s, 2H), 4.52 (t, 2H, $J = 6.8$), 7.39 (unresolved dd, 1H, $J = 8.0$), 7.78 (d, 1H, $J = 8.0$), 7.95 (s, 1H), 8.23 (d, 1H, $J = 8.0$), 8.54 (d, 1H, $J = 8.3$), 8.93 (s, 1H), 9.18 (d, 1H, $J = 8.3$), 9.56 (s, 1H), 11.76 (br s, 1H); HRMS calculated for $\text{C}_{28}\text{H}_{23}\text{ClN}_4\text{O}_5$ 530.1357, found 530.1358.

7-N-Acetyl-6-pyrrolidinolavendamyacin Methyl Ester (24). To a stirred solution of 7-acetyl lavendamyacin methyl ester^{41,42} (**3**, 50 mg, 0.11 mmol) in dry chloroform (30 mL) was added pyrrolidine (0.2 mL, 170 mg, 2.4 mmol), and the resulting red-brown solution was allowed to stir at room temperature for 2 h. The reaction mixture was rotaevaporated to dryness. The solid was washed with ether (10 mL) and dried under vacuum pump to afford 51 mg (88%) of the product as a reddish brown powder: mp 210 °C (dec); $R_f = 0.13$ (Et OAc/ CH_2Cl_2 1/1); $^1\text{H NMR}$ ($\text{DMSO}-d_6$) δ 1.75–1.96 (br m, 4H), 2.11 (s, 3H), 3.11 (3H, s), 3.11 (s, 3H), 3.78–3.58 (br m, 4H), 3.98 (s, 3H), 7.48–7.41 (m, 1H), 7.70–7.76 (m, 1H), 7.82 (d, 1H, $J = 7.9$), 8.45 (d, 1H, $J = 7.9$), 8.50 (d, 1H, $J = 8.2$), 8.78 (d, 1H, $J = 8.2$), 9.33 (s, 1H), 12.36 (s, 1H); EAB–HRMS calculated for $\text{C}_{29}\text{H}_{25}\text{N}_5\text{O}_5\text{Na}$ ($\text{M} + \text{Na}$)⁺ 546.1753, found 546.1779.

7-N-Acetyl-6-aziridinodemethyl lavendamyacin Amide (25). To a stirred solution of 7-acetyl demethyl lavendamyacin amide³⁸ (**5**, 50 mg, 0.12 mmol) in dry chloroform (25 mL) and dry ethanol (25 mL) was added aziridine (0.7 mL, 58 mg, 13.5 mmol), and the resulting reddish brown solution was allowed to stir at room temperature for 48 h. Then the reaction mixture was rotaevaporated to dryness. The solid was washed with ether (10 mL) and further dried under a vacuum pump to afford 52 mg (93%) of the product as a reddish brown powder: mp > 260 °C; $R_f = 0.88$ (MeOH/ CH_2Cl_2 1/10); $^1\text{H NMR}$ ($\text{DMSO}-d_6$) δ 2.17 (s, 3H), 2.39 (s, 4H), 7.38–7.44 (m, 1H), 7.68 (s, 1H), 7.69–7.74 (m, 1H), 7.83 (d, 1H, $J = 8.2$), 8.49–8.55 (m, 2H), 8.62 (s, 1H), 9.07 (s, 1H), 9.45 (d, 1H, $J = 8.2$), 9.57 (s, 1H), 12.05 (s, 1H); HRMS calculated for $\text{C}_{25}\text{H}_{19}\text{N}_6\text{O}_4$ ($\text{M} + \text{H}$)⁺ 467.1468, found 467.1480.

7-Amino-6-chloro-2-formylquinoline-5,8-dione (46). In a dry 100 mL round-bottomed two-necked flask, equipped with a magnetic bar and water-cooled reflux condenser under argon, 7-amino-6-chloro-2-methylquinoline-5,8-dione⁴⁴ (**30**, 133.8 mg, 0.6 mmol), selenium dioxide (106.6 mg), 20 mL of dried and distilled 1,4-dioxane, and 0.09 mL of water were stirred at reflux in an oil bath for 23 h. The reaction was monitored by TLC. The mixture was hot filtered, and the solid was washed with hot chloroform. The filtrate was rotaevaporated to dryness. The dried material was dissolved in 480 mL of chloroform and washed with saturated sodium chloride solution (4 × 60 mL). The solution was dried over magnesium sulfate and rotaevaporated to dryness and then further dried under a vacuum pump. The product weighed 105.2 mg (74%): mp 220 °C (dec); $^1\text{H NMR}$ (CDCl_3) δ 5.6 (br s, 2H), 8.28 (d, 1H, $J =$

8.1), 8.67 (d, 1H, $J = 8.1$), 10.30 (s, 1H); HRMS calculated for $\text{C}_{10}\text{H}_6\text{ClN}_2\text{O}_3$ ($\text{M} + \text{H}$)⁺ 237.0061, found 237.0068.

6-Chlorolavendamyacin Methyl Ester (32). In a setup similar to that used for the synthesis of **16**, 7-amino-6-chloro-2-formylquinoline-5,8-dione (**31**, 118.5 mg, 0.5 mmol) was placed with β -methyltryptophan methyl ester⁴³ (115 mg, 0.5 mmol) in 300 mL of dry anisole. The solution was stirred and heated slowly to 130 °C over 3 h. The reaction mixture was refluxed for 1 h. The mixture was then cooled to room temperature under argon. The solvent was rotaevaporated to dryness, and then the solid was washed with acetone (20 mL). The resulting solid was vacuum filtered and dried under a vacuum pump. The product weighed 131.9 mg (59%): mp > 270 °C, $R_f = 0.09$ (CHCl_3 , twice developed); $^1\text{H NMR}$ (CDCl_3) δ 3.22 (s, 3H), 4.08 (s, 3H), 5.70 (br s, 2H), 7.38–7.45 (m, 1H), 7.65–7.71 (m, 1H), 7.80 (d, 1H, $J = 8.0$), 8.38 (d, 1H, $J = 7.7$), 8.61 (d, 1H, $J = 8.4$), 9.10 (d, H, $J = 8.4$), 11.89 (br s, 1H), CIMS *m/e* (relative intensity) 446.1 (M^+ , 100), 416.0 (10.3), 386.0 (64.4), 351.1 (22.0), 113.0 (9.0); HRMS calculated for $\text{C}_{23}\text{H}_{15}\text{N}_4\text{O}_4\text{Cl}$ 446.0849, found 446.0781.

5,7-Dibromo-8-hydroxy-2-methylquinoline (55). The procedure for the preparation of **55** was similar to that of **56**, except that after the evaporation of the combined filtrates the dry residue was dissolved in 100 mL of chloroform, filtered, and then concentrated to small volume. The solution was kept in the refrigerator for a day to give a yellow product (455, mg, 29%): mp 234–235 °C; $^1\text{H NMR}$ ($\text{DMSO}-d_6$) δ 8.14 (d, 1H, $J = 8.8$), 8.25 (s, 1H), 8.63 (d, 1H, $J = 8.8$), 10.19 (s, 1H), 11.31 (br s, 1H); HRMS calculated for $\text{C}_{10}\text{H}_5\text{Br}_2\text{NO}_2$ 328.8667, found 328.8667.

3-Carbomethoxy-1-(5,7-Dibromo-8-hydroxyquinoline-2-yl)-4-methyl- β -carboline (57). In a setup similar to that used for **16**, 5,7-dibromo-2-formyl-8-hydroxyquinoline (165.5 mg, 0.5 mmol) and β -methyltryptophan methyl ester (115.5 mg, 0.5 mmol) in 70 mL of dry anisole were mixed. Heat was introduced, and the temperature was raised to reflux over a 3-h period and then refluxed for 39 more h. The reaction mixture was evaporated under reduced pressure, and the solid was dried under vacuum. The crude yellow solid weighed 217 mg, (80%). An analytical sample was obtained as follows: The material was stirred in a small volume of dichloromethane giving an orange solid. The filtrate was allowed to stand at room temperature to produce more of the pure **57**: mp 248 °C (dec); $R_f = 0.62$ (0.3/5 pet. ether/EtOAc); $^1\text{H NMR}$ (CDCl_3) δ 3.13 (s, 3H), 3.99 (s, 3H), 7.43 (dd, 1H, $J = 8.1, 7.0$), 7.72 (dd, 1H, $J = 8.1, 7.0$), 7.91 (d, 1H, $J = 8.1$), 8.17 (s, 1H), 8.44 (d, 1H, $J = 8.1$), 8.68 (d, 1H, $J = 8.8$), 8.95 (d, 1H, $J = 8.8$), 12.23 (br s, 1H); HRMS calculated for $\text{C}_{23}\text{H}_{15}\text{Br}_2\text{N}_3\text{O}_3$ 540.9454, found 540.9459.

7-Bromodeaminolavendamyacin Methyl Ester (34). In a 500 mL round-bottomed flask equipped with a condenser, a dropping funnel, a magnetic bar, and an argon-filled balloon, a mixture of 63.5 mg (0.117 mmol) of the crude **57** in 200 mL of acetonitrile–water (2/1, v/v) was dropwise added to a cold solution of 110.7 mg (0.257 mmol) of bis(trifluoroacetoxy)-iodobenzene in 33 mL of acetone–water (2/1, V/V) at 0 °C over 2 h and 40 min. The reaction mixture was stirred at this temperature for 6 more h. The mixture was evaporated under reduced pressure to remove acetonitrile and then extracted with chloroform (3 × 40 mL). The combined extracts were dried (MgSO_4) and evaporated to give an impure orange product. Flash chromatography ($\text{CHCl}_3/\text{EtOAc}$ 250/3) gave 25.75 mg (46%) of the orange product **34**: mp 209 °C (dec); $R_f = 0.62$ (0.4/5 EtOAc/ CH_2Cl_2); $^1\text{H NMR}$ (CDCl_3) δ 3.21 (s, 3H), 4.08 (s, 3H), 7.35–7.45 (m, 1H), 7.60 (s, 1H), 7.65–7.7 (m, 1H), 7.81 (d, 1H, $J = 8.0$), 8.35 (d, 1H, $J = 8.0$), 8.50 (d, 1H, $J = 8.2$), 9.09 (d, 1H, $J = 8.4$), 11.90 (br s, 1H); HRMS calculated for $\text{C}_{23}\text{H}_{14}\text{BrN}_3\text{O}_4$ 475.0162, found 475.0143.

Decarboxy-2'-(hydroxymethyl)-demethyl lavendamyacin (37). In a dry 5 mL round-bottomed flask equipped with a condenser, a magnetic bar, and an argon-filled balloon, a mixture of acetamido compound **22** (24 mg, 0.0582 mmol) in 1 mL of 70% sulfuric acid solution ($\text{H}_2\text{SO}_4/\text{H}_2\text{O}$ 70/30, v/v) was heated in an oil bath at 60 °C for 2 h. The reaction mixture

was treated with a saturated solution of sodium carbonate to pH of 9 and then extracted with EtOAc (5 × 20 mL). The combined organic layers were washed with brine (2 × 10 mL), dried (MgSO₄), and evaporated under reduced pressure to give 19 mg (88%) of a red solid: mp 255–260 °C (dec); $R_f = 0.59$ (0.4/5 MeOH/CH₂Cl₂); ¹H NMR (DMSO-*d*₆) δ 4.85 (d, 2H), 5.54 (br s, 1H), 5.93 (br s, 2H), 7.33 (dd, 1H, $J = 7.2$), 7.64 (dd, 1H, $J = 7.2$), 7.69 (d, 1H, $J = 8.0$), 8.36–8.38 (m, 2H), 8.46 (d, 1H, $J = 8.0$), 8.88 (d, 1H, $J = 8.0$), 11.64 (br s, 1H); HRMS calculated for C₂₁H₁₄N₄O₃ 370.1066, found 370.1072.

Decarboxydemethylavendamyacin (38). In a method similar to that of **37**, 20 mg (0.052 mmol) of compound **14** in 2.4 mL of 70% H₂SO₄ was heated at 60 °C for 4 h to give **38** as a red solid (15 mg, 85%): mp > 270 °C; $R_f = 0.47$ (0.2/5 MeOH/CH₂Cl₂); ¹H NMR (DMSO-*d*₆) δ 5.94 (br s, 2H), 7.3–7.4 (m, 1H), 7.65–7.8 (m, 2H), 8.36–8.38 (m, 2H), 8.48 (d, 1H, $J = 8.0$), 8.59 (d, 1H, $J = 8.4$), 8.91 (d, 1H, $J = 8.4$), 11.77 (br s, 1H); HRMS calculated for C₂₀H₁₂N₄O₂ 340.0960, found 340.0597.

2-Formyl-8-hydroxyquinoline (56). In a 500 mL round-bottomed flask equipped with a magnetic bar, an argon-filled balloon, and a water-cooled condenser, 8-hydroxy-2-methylquinoline (**54**, 2 g, 12.4 mmol), selenium dioxide (1.74 g, 15.8 mmol), 300 mL of dried and distilled 1,4-dioxane, and 1.5 mL of water were mixed. The reaction mixture was heated, and the temperature was raised to reflux over a 2.5 h period. The mixture was refluxed for 21.5 h when thin-layer chromatography showed the completion of the reaction. The reaction mixture was filtered off, and the selenium metal was washed with 160 mL of dichloromethane. The combined filtrates were evaporated under reduced pressure to dryness. The residue was sublimed (at 81 °C, 0.15 mm/Hg) to give a pure yellow solid (1.337 g, 61%): mp 95–96 °C; ¹H NMR (CDCl₃) δ 7.27 (d, 1H, $J = 7.9$), 7.42 (d, 1H, $J = 8.3$), 7.62 (t, 1H, $J = 7.8$), 8.03 (s, 1H), 8.1 (d, 1H, $J = 12.7$), 8.31 (d, 1H, $J = 8.2$), 10.21 (s, 1H); MS m/z 174 (M+H)⁺, 173 and 172; Analysis for C₁₀H₇NO₂ calculated C, 69.36; H, 4.07; N, 8.09, found C, 69.34; H, 4.2; N, 8.06.

1-(8-Hydroxyquinoline-2-yl)-β-carboline (58). In a 100 mL three-necked round-bottomed flask equipped with a condenser, a magnetic bar, and flowing argon, 2-formyl-8-hydroxyquinoline (**56**, 35.5 mg, 0.2 mmol), tryptamine (32.6 mg, 0.2 mmol) and 20 mL of dried distilled anisole were mixed together. The mixture was heated, and the temperature was raised to reflux over the course of 4 h and then refluxed for 22 h. To the mixture was added 10 mg of 5% Pd/C, and after 7 more hours of reflux another 5 mg of Pd/C was added and then refluxed for 20 more hours. The mixture was filtered and rotaevaporated to dryness. The material was recrystallized from acetone giving 48 mg (76%) of a yellow solid: mp 276–279 °C; $R_f = 0.12$ (0.4/5 MeOH/CH₂Cl₂); ¹H NMR (DMSO-*d*₆) δ 7.28 (m, 1H), 7.34 (dd, 1H, $J = 7.6$), 7.52 (d, 1H, $J = 5.0$), 7.65 (dd, 1H, $J = 8.0$, 7.8), 7.77 (d, 1H, $J = 8.0$), 8.32 (d, 1H, $J = 5.0$), 8.36 (d, 1H, $J = 8.0$), 8.51 (d, 1H, $J = 8.8$), 8.59 (d, 1H, $J = 5.0$), 8.82 (d, 1H, $J = 8.8$), 10.35 (s, 1H), 12.16 (br s, 1H); HRMS calculated for C₂₀H₁₃N₃O 311.1058, found 311.1045.

Deaminodecarboxydemethylavendamyacin (39). Compound **39** was obtained in a procedure similar to that of **34** except that the reaction was performed in a 250 mL flask. A solution of 3-carbomethoxy-1-(8-hydroxyquinoline-2-yl)-β-carboline (**58**, 15 mg, 0.048 mmol) in 120 mL of acetonitrile–water (2/1, v/v) was dropwise added to a solution of bis(trifluoroacetoxy)iodobenzene (41.5 mg, 0.096 mmol) in 7.5 mL of acetonitrile–water at 0 °C over a 2 h period. The mixture was allowed to stir at this temperature for another 2 h and then evaporated in vacua to remove acetonitrile. The residue was extracted with dichloromethane (3 × 25 mL), dried (MgSO₄), and evaporated to give 12 mg (77%) of the orange product **39**: mp 227–229 °C (dec); $R_f = 0.33$ (0.003/5 MeOH/CH₂Cl₂); ¹H NMR (CDCl₃) δ 7.07 (dd, 1H, $J = 10.4$), 7.16 (dd, 1H, $J = 10.4$), 7.31 (dd, 1H, $J = 7.2$), 7.62 (dd, 1H, $J = 7.2$), 7.75 (d, 1H, $J = 8.0$), 8.10 (d, 1H, $J = 5.0$), 8.17 (d, 1H, $J = 7.8$), 8.50 (d, 1H, $J = 8.4$), 8.58 (d, 1H, $J = 5.0$), 9.02 (d, 1H, $J = 8.4$), 11.69 (br s, 1H); HRMS calculated for C₂₀H₁₁N₃O₂ 325.0851, found 325.0862.

Electrochemistry. Cyclic voltammetry (CV) for 14 lavendamyacin analogues was conducted using a BAS CV-50W electrochemical analyzer equipped with a standard three-electrode cell. This cell was designed to allow the tip of the reference electrode to approach closely to the working electrode. Voltammetric experiments were performed using Ag/AgCl as the reference electrode, a glossy carbon (GC) rod as the working electrode, and a platinum (Pt) wire as the auxiliary electrode. Potential data are referred to the Ferrocene (0/+) couple, which is oxidized in DMSO at +0.52 V vs Ag/AgCl. Positive-feedback iR compensation was routinely applied. The working electrode was regularly polished using alumina. Typically, a solution containing 1 mM of the lavendamyacin analogues and 0.1 M supporting electrolyte (tetrabutylammonium hexafluorophosphate, Bu₄NPF₆) was prepared using dried dimethyl sulfoxide (DMSO). All samples were purged with argon prior to use and kept under a continuous flow of argon during the course of the experiments. All CV data were recorded at a potential range between 0.00 and –2.00 V and at potential sweep rates of 50 to 500 mV/s. All measurements were performed at 22 ± 1 °C.

Biological Studies. Cell Culture. BE-WT and BE-NQ cells were a gift from Dr. David Ross (University of Colorado Health Sciences Center, Denver, CO). Cells were grown in minimum essential medium (MEM) with Earle's salts, nonessential amino acids, L-glutamine and penicillin/streptomycin and supplemented with 10% fetal bovine serum (FBS), sodium bicarbonate and HEPES. Cell culture medium and supplements were obtained from Gibco, Invitrogen Co., Grand Island, NY. The cells were incubated at 37 °C under a humidified atmosphere containing 5% CO₂.

Cytochrome *c* Assay. Lavendamyacin analogues reduction was monitored using a spectrophotometric assay in which the rate of reduction of cytochrome *c* was quantified at 550 nm. Briefly, the assay mixture contained cytochrome *c* (70 μM), NADH (1 mM), human recombinant NQO1 (0.1–3 μg) (gift from Dr. David Ross, University of Colorado Health Sciences Center, Denver, CO), and lavendamyacin (25 μM) in a final volume of 1 mL of Tris-HCl (25 mM, pH 7.4) containing 0.7 mg/mL BSA and 0.1% Tween-20. Reactions were carried out at room temperature and started by the addition of NADH. Rates of reduction were calculated from the initial linear part of the reaction curve (0–30 s), and results were expressed in terms of μmol of cytochrome *c* reduced/min/mg of NQO1 using a molar extinction coefficient of 21.1 mM⁻¹ cm⁻¹ for cytochrome *c*. All reactions were carried out in triplicate.

MTT Assay. Growth inhibition was determined using the MTT colorimetric assay. Cells were plated in 96-well plates at a density of 10000 cells/mL and allowed to attach overnight (16 h). Lavendamyacin analogues solutions were applied in medium for 2 h. Lavendamyacin analogues solutions were removed and replaced with fresh medium and 96-well plates were incubated at 37 °C under a humidified atmosphere containing 5% CO₂ for 4–5 days. MTT (50 μg) was added, and the cells were incubated for another 4 h. Medium/MTT solutions were removed carefully by aspiration, the MTT formazan crystals were dissolved in 100 μL of DMSO, and absorbance was determined on a plate reader at 560 nm. IC₅₀ values (concentration at which cell survival equals 50% of control) were determined from semilog plots of percent of control vs concentration. Selectivity ratios were defined as the IC₅₀ value for the BE-WT cell line divided by the IC₅₀ value for the BE-NQ cell line.

Clonogenic Assay. Cells were harvested from logarithmic-phase growing cultures and plated at densities of 1000 cells per 100-mm dish to yield a readily quantifiable number of colonies at the end of the experiment. After 24 h, cells were treated with lavendamyacin analogues, 2% DMSO (drug vehicle), or no treatment (control) for 2 h at 37 °C. After 2 h, drug-containing medium was replaced with fresh drug-free medium. Cells were incubated at 37 °C under a humidified atmosphere containing 5% CO₂ for 12 days. Then, the medium was removed, and colonies were washed twice with PBS, fixed and stained with 0.1% (w/v) Coomassie Blue dye in 30%

methanol and 10% acetic acid for 1–2 min. Surviving colonies (>50 cells) were counted and the surviving fraction determined by dividing the number of colonies in a treatment dish by the number of colonies in the control dish. IC₅₀ values (concentration at which cell survival equals 50% of control) were determined from semilog plots of percent of control vs concentration. Selectivity ratios were defined as the IC₅₀ value for the BE-WT cell line divided by the IC₅₀ value for the BE-NQ cell line.

Molecular Modeling. Coordinates Preparation. The coordinates of the crystal structure of human NQO1 complex with bound FAD and **65**, obtained from the Protein Data Bank (PDB ID code: 1H69²⁵), were used as a reference structure for the docking experiments, and compound **65** served as the original reference ligand. The physiological dimer in the crystal unit was used for docking purposes. The coordinates were locally minimized. The coordinates were subjected to energy minimization with minimal iterations (100) by Powell minimization standard method using Minimize Subset option. This option automatically selected 24 seed amino acid residues surrounding the superposed ligand **37** (refer to the Docking section below) to perform the local minimization. Default parameters and values within the minimization dialogue were used except where otherwise mentioned. This procedure yielded a weighted root-mean-square distance of 0.26 Å between the 24 corresponding nonminimized and minimized residues in the structures. Docking calculations were performed using one of the two identical active sites.

Ligand Preparation. The structures of ligands were sketched and prepared as MOL2 files employing the Sketch Molecule module of SYBYL 6.9.1 software suite⁵⁸ (Tripos, Inc.; St. Louis, MO). Initially sketched ligands were subjected to energy minimization (10000 iterations) by Powell minimization standard method. Initial Optimization and Termination parameters were set to None and Energy Change options, respectively. Default parameters and values within the minimization dialogue (Minimize Details) were used except where otherwise mentioned. The final ligand conformational coordinates were stored as MOL2 files within the database.

Docking. Flexible docking was performed using the FlexX module of SYBYL 6.9.1 software suite.⁵⁸ FlexX is an automatic docking program for conformationally flexible ligands, employs the three-dimensional structure of the target protein in PDB format, and is capable of determining 30 possible conformations for each docked ligand. The final ranking order of conformations is based on the free binding energy. This program automatically selects the base fragment of a ligand (the ligand core). The base fragment is then placed into the active site of the target protein using the algorithmic approach called pose clustering that is based upon a pattern recognition paradigm. Subsequent incremental reconstruction of the complete ligand molecule is then performed by linking the remaining components.^{59,60} In this study, to define the active site, the energy-minimized ligand **37** was superpositioned to the coordinates of the original reference ligand **65** such that overlap was optimal. Ligand **37** was again energy minimized in the context of the active site, and therefore the position of the ligand within the pocket was optimized. The active site was then defined as all the amino acid residues confined within 6.5 Å radius sphere centered on the superposed ligand **37**. FAD was introduced to the active site as a heteroatom file in MOL2 format.

Scoring Functions. The docked conformations of ligands were evaluated and ranked using FlexX and four scoring functions implemented in the CSCORE module in SYBYL. CSCORE is a consensus scoring program that integrates multiple well-known scoring functions such as FlexX and ChemScore,⁶¹ D-Score,⁶² G-Score,⁶³ and PMF-Score⁶⁴ to evaluate docked conformations. Individual scoring functions are used to predict the affinity of the ligand binding to a target protein. CSCORE creates columns in a molecular spreadsheet that contain raw scores for each individual scoring function. The consensus column contains integers that range from 0 to 5; where 5 is the best fit to the model. Docked conformations

whose scores exceed the threshold for a particular function contribute one to the value of the consensus, whereas those with scores below the threshold add a zero.

Molecular Graphics System. The molecular graphics images and surface representations were prepared by PyMOL molecular graphics system version PyMOLX11Hybrid 0.97⁶⁶ (Delano Scientific, San Carlos, CA). The data of the coordinates of the NQO1 complex with bound FAD and docked conformations of ligands were prepared in PDB format as PyMOL input files. PyMOL session files of the NQO1 active site with docked conformations of ligands and the superimposition of clustered conformations were created. The images were then stored as graphic files.

Acknowledgment. We acknowledge financial support from the American Cancer Society and the National Institutes of Health (NIH grants: R15 CA78232, H.D.B.; NCRP P20 RR15583, J.M.G.; and CA74245, M.B.). We thank Professor David Williams, his graduate student Andrew Donnell, and the staff at the Mass Spectroscopy Laboratory of Indiana University for their assistance in obtaining mass spectral data. We also thank Professor Edward Rosenberg and his graduate student Dalia Rokhsana at the Department of Chemistry of the University of Montana for their assistance with the electrochemistry. The expert assistance of Rohn Wood in the Molecular Computational Core Facility of the University of Montana is greatly appreciated.

Supporting Information Available: NMR spectra for compounds **4**, **14–25**, **32**, **34**, **37–39**, **41**, and **46**, analytical data for compounds **14–25**, **32**, **34**, **37–39**, and geometric post-docking analyses of the poses of compounds **31** and **37** are available free of charge via the Internet at <http://pubs.acs.org>.

References

- (1) Workman, P. Keynote address: Bioreductive mechanisms. *Int. J. Radiat. Oncol. Biol. Phys.* **1992**, *22*, 631–637.
- (2) Rooseboom, M.; Commandeur, J. N.; Vermeulen, N. P. Enzyme-catalyzed activation of anticancer prodrugs. *Pharmacol. Rev.* **2004**, *56*, 53–102.
- (3) Beall, H. D.; Winski, S. I. Mechanisms of action of quinone-containing alkylating agents. I: NQO1-directed drug development. *Front. Biosci.* **2000**, *5*, 639–648.
- (4) Phillips, R. M. Prospects for bioreductive drug development. *Exp. Opin. Invest. Drugs* **1998**, *7*, 905–928.
- (5) Workman, P. Enzyme-directed bioreductive drug development revisited: A commentary on recent progress and future prospects with emphasis on quinone anticancer agents and quinone metabolizing enzymes, particularly DT-diaphorase. *Oncol. Res.* **1994**, *6*, 461–475.
- (6) Skelly, J. V.; Sanderson, M. R.; Suter, D. A.; Baumann, U.; Read, M. A.; Gregory, D. S.; Bennett, M.; Hobbs, S. M.; Neidle, S. Crystal structure of human DT-diaphorase: A model for interaction with the cytotoxic prodrug 5-(aziridin-1-yl)-2,4-dinitrobenzamide (CB1954). *J. Med. Chem.* **1999**, *42*, 4325–4330.
- (7) Danson, S.; Ward, T. H.; Butler, J.; Ranson, M. DT-diaphorase: A target for new anticancer drugs. *Cancer Treat. Rev.* **2004**, *30*, 437–449.
- (8) Lind, C.; Cadenas, E.; Hochstein, P.; Ernster, L. DT-diaphorase: Purification, properties, and function. *Methods Enzymol.* **1990**, *186*, 287–301.
- (9) Faig, M.; Bianchet, M. A.; Talalay, P.; Chen, S.; Winski, S.; Ross, D.; Amzel, L. M. Structures of recombinant human and mouse NAD(P)H: quinone oxidoreductases: Species comparison and structural changes with substrate binding and release. *Proc. Natl. Acad. Sci. U.S.A.* **2000**, *97*, 3177–3182.
- (10) Li, R.; Bianchet, M. A.; Talalay, P.; Amzel, L. M. The three-dimensional structure of NAD(P)H: quinone reductase, a flavoprotein involved in cancer chemoprotection and chemotherapy: Mechanism of the two-electron reduction. *Proc. Natl. Acad. Sci. U.S.A.* **1995**, *92*, 8846–8850.
- (11) Eliasson, M.; Bostrom, M.; DePierre, J. W. Levels and subcellular distributions of detoxifying enzymes in the ovarian corpus luteum of the pregnant and non-pregnant pig. *Biochem. Pharmacol.* **1999**, *58*, 1287–1292.
- (12) Winski, S. L.; Koutalos, Y.; Bentley, D. L.; Ross, D. Subcellular localization of NAD(P)H:quinone oxidoreductase 1 in human cancer cells. *Cancer Res.* **2002**, *62*, 1420–1424.

- (13) Ernster, L. DT Diaphorase. *Methods Enzymol.* **1967**, *10*, 309–317.
- (14) Ernster, L. DT Diaphorase: A historical review. *Chem. Scripta* **1987**, *27A*, 1–13.
- (15) Siegel, D.; Gibson, N. W.; Preusch, P. C.; Ross, D. Metabolism of mitomycin C by DT-diaphorase: Role in mitomycin C-induced DNA damage and cytotoxicity in human colon carcinoma cells. *Cancer Res.* **1990**, *50*, 7483–7489.
- (16) Walton, M. I.; Smith, P. J.; Workman, P. The role of NAD(P)H: quinone reductase (EC 1.6.99.2, DT-diaphorase) in the reductive bioactivation of the novel indolequinone antitumor agent EO9. *Cancer Commun.* **1991**, *3*, 199–206.
- (17) Siegel, D.; Beall, H. D.; Senekowitsch, C.; Kasai, M.; Arai, H.; Gibson, N. W.; Ross, D. Bioreductive activation of mitomycin C by DT-diaphorase. *Biochemistry* **1992**, *31*, 7879–7885.
- (18) Naylor, M. A.; Swann, E.; Everett, S. A.; Jaffar, M.; Nolan, J.; Robertson, N.; Lockyer, S. D.; Patel, K. B.; Dennis, M. F.; Stratford, M. R.; Wardman, P.; Adams, G. E.; Moody, C. J.; Stratford, I. J. Indolequinone antitumor agents: Reductive activation and elimination from (5-methoxy-1-methyl-4,7-dioxindol-3-yl)methyl derivatives and hypoxia-selective cytotoxicity in vitro. *J. Med. Chem.* **1998**, *41*, 2720–2731.
- (19) Siegel, D.; Gibson, N. W.; Preusch, P. C.; Ross, D. Metabolism of diaziquone by NAD(P)H:(quinone acceptor) oxidoreductase (DT-diaphorase): Role in diaziquone-induced DNA damage and cytotoxicity in human colon carcinoma cells. *Cancer Res.* **1990**, *50*, 7293–7300.
- (20) Schlager, J. J.; Powis, G. Cytosolic NAD(P)H:(quinone-acceptor)-oxidoreductase in human normal and tumor tissue: Effects of cigarette smoking and alcohol. *Int. J. Cancer* **1990**, *45*, 403–409.
- (21) Malkinson, A. M.; Siegel, D.; Forrest, G. L.; Gazdar, A. F.; Oie, H. K.; Chan, D. C.; Bunn, P. A.; Mabry, M.; Dykes, D. J.; Harrison, S. D.; Ross, D. Elevated DT-diaphorase activity and messenger RNA content in human non small cell lung carcinoma: Relationship to the response of lung tumor xenografts to mitomycin C. *Cancer Res.* **1992**, *52*, 4752–4757.
- (22) Cresteil, T.; Jaiswal, A. K. High levels of expression of the NAD-(P)H: quinone oxidoreductase (NQO1) gene in tumor cells compared to normal cells of the same origin. *Biochem. Pharmacol.* **1991**, *42*, 1021–1027.
- (23) Rampling, R.; Cruickshank, G.; Lewis, A. D.; Fitzsimmons, S. A.; Workman, P. Direct measurement of pO₂ distribution and bioreductive enzymes in human malignant brain tumors. *Int. J. Radiat. Oncol. Biol. Phys.* **1994**, *29*, 427–431.
- (24) Mikami, K.; Naito, M.; Ishiguro, T.; Yano, H.; Tomida, A.; Yamada, T.; Tanaka, N.; Shirakusa, T.; Tsuruo, T. Immunological quantitation of DT-diaphorase in carcinoma cell lines and clinical colon cancers: Advanced tumors express greater levels of DT-diaphorase. *Jpn. J. Cancer Res.* **1998**, *89*, 910–915.
- (25) Faig, M.; Bianchet, M. A.; Winski, S.; Hargreaves, R.; Moody, C. J.; Hudnott, A. R.; Ross, D.; Amzel, L. M. Structure-based development of anticancer drugs: Complexes of NAD(P)H: quinone oxidoreductase 1 with chemotherapeutic quinones. *Structure* **2001**, *9*, 659–667.
- (26) Winski, S. L.; Faig, M.; Bianchet, M. A.; Siegel, D.; Swann, E.; Fung, K.; Duncan, M. W.; Moody, C. J.; Amzel, L. M.; Ross, D. Characterization of a mechanism-based inhibitor of NAD(P)H: quinone oxidoreductase 1 by biochemical, X-ray crystallographic, and mass spectrometric approaches. *Biochemistry* **2001**, *40*, 15135–15142.
- (27) Zhou, Z.; Fisher, D.; Spidel, J.; Greenfield, J.; Patson, B.; Fazal, A.; Wigal, C.; Moe, O. A.; Madura, J. D. Kinetic and docking studies of the interaction of quinones with the quinone reductase active site. *Biochemistry* **2003**, *42*, 1985–1994.
- (28) Cavelier, G.; Amzel, L. M. Mechanism of NAD(P)H: quinone reductase: Ab initio studies of reduced flavin. *Proteins: Struct. Funct. Genet.* **2001**, *43*, 420–432.
- (29) Doyle, T. W.; Balitz, D. M.; Grulich, R. E.; Nettleton, D. E.; Gould, S. J.; Tann, C.; Moews, A. E. Structure determination of lavendamycin, a new antitumor antibiotic from *Streptomyces lavendulae*. *Tetrahedron Lett.* **1981**, *22*, 4595–4598.
- (30) Balitz, D. M.; Bush, J. A.; Bradner, W. T.; Doyle, T. W.; O'Herron, F. A.; Nettleton, D. E. Isolation of lavendamycin, a new antibiotic from *Streptomyces lavendulae*. *J. Antibiot. (Tokyo)* **1982**, *35*, 259–265.
- (31) Erickson, W. R.; Gould, S. J. Streptonigrin biosynthesis. 7. Incorporation of oxygen from ¹⁸O₂: Evidence for an oxidative β-carboline cleavage. *J. Am. Chem. Soc.* **1985**, *107*, 5831–5832.
- (32) Erickson, W. R.; Gould, S. J. Streptonigrin Biosynthesis. 8. Evidence for the involvement of a new Shikimate pathway product and a new route to quinolines. *J. Am. Chem. Soc.* **1987**, *109*, 620–621.
- (33) Rao, K. V.; Biemann, K.; Woodward, R. B. The structure of streptonigrin. *J. Am. Chem. Soc.* **1963**, *85*, 2532–2533.
- (34) Boger, D. L.; Yasuda, M.; Mitscher, L. A.; Drake, S. D.; Kitos, P. A.; Thompson, S. C. Streptonigrin and lavendamycin partial structures. Probes for the minimum, potent pharmacophore of streptonigrin, lavendamycin, and synthetic quinoline-5,8-diones. *J. Med. Chem.* **1987**, *30*, 1918–1928.
- (35) Hackethal, C. A.; Golbey, R. B.; Tan, C. T.; Karnofsky, D. A.; Burchenal, J. H. Clinical observations on the effects of streptonigrin in patients with neoplastic disease. *Antibiot. Chemother.* **1961**, *11*, 178–183.
- (36) Fang, Y.; Linardic, C. M.; Richardson, D. A.; Cai, W.; Behforouz, M.; Abraham, R. T. Characterization of the cytotoxic activities of novel analogues of the antitumor agent, lavendamycin. *Mol. Cancer Ther.* **2003**, *2*, 517–526.
- (37) Behforouz, M.; Merriman, R. L. Lavendamycin analogues and methods of making and using them. U.S. Patent 5525611, 1996.
- (38) Behforouz, M.; Cai, W.; Stocksdale, M. G.; Lucas, J. S.; Jung, J. Y.; Briere, D.; Wang, A.; Katzen, K. S.; Behforouz, N. C. Novel lavendamycin analogues as potent HIV-reverse transcriptase inhibitors: Synthesis and evaluation of anti-reverse transcriptase activity of amide and ester analogues of lavendamycin. *J. Med. Chem.* **2003**, *46*, 5773–5780.
- (39) Kende, A. S.; Ebetino, F. H. The regioselective total synthesis of lavendamycin methyl ester. *Tetrahedron Lett.* **1984**, *25*, 923–926.
- (40) Boger, D. L.; Duff, S. R.; Panek, J. S.; Yasuda, M. Total synthesis of lavendamycin methyl ester. *J. Org. Chem.* **1985**, *50*, 5790–5795.
- (41) Behforouz, M.; Gu, Z.; Cai, W.; Horn, M. A.; Ahmadian, M. A highly concise synthesis of lavendamycin methyl ester. *J. Org. Chem.* **1993**, *58*, 7089–7091.
- (42) Behforouz, M.; Haddad, J.; Cai, W.; Arnold, M. B.; Mohammadi, F.; Sousa, A. C.; Horn, M. A. Highly efficient and practical syntheses of lavendamycin methyl ester and related novel quinolindiones. *J. Org. Chem.* **1996**, *61*, 6552–6555.
- (43) Behforouz, M.; Zarrinmayeh, H.; Ogle, M. E.; Riehle, T. J.; Bell, F. W. β-Carbolines derived from β-methyltryptophan and a stereoselective synthesis of (2RS,3SR)-β-methyltryptophan methyl ester. *J. Heterocycl. Chem.* **1988**, *25*, 1627–1632.
- (44) Behforouz, M.; Haddad, J.; Cai, W.; Gu, Z. Chemistry of quinoline-5,8-diones. *J. Org. Chem.* **1998**, *63*, 343–346.
- (45) Seradij, H.; Cai, W.; Erasga, N. O.; Chenault, D. V.; Knuckles, K. A.; Ragains, J. R.; Behforouz, M. Total synthesis of novel 6-substituted lavendamycin antitumor agents. *Org. Lett.* **2004**, *6*, 473–476.
- (46) Barret, R.; Daudon, M. Oxidation of phenols to quinones by bis-(trifluoroacetoxy)iodobenzene. *Tetrahedron Lett.* **1990**, *31*, 4871–4872.
- (47) Tolstikov, V. V.; Holpne Kozlova, N. V.; Oreshkina, T. D.; Osipova, T. V.; Preobrazhenskaya, M. N.; Sztaricskai, F.; Balzarini, J.; De Clercq, E. Amides of antibiotic streptonigrin and amino dicarboxylic acids or aminosugars. Synthesis and biological evaluation. *J. Antibiot. (Tokyo)* **1992**, *45*, 1020–1025.
- (48) Cotterill, A. S.; Moody, C. J.; Mortimer, R. J.; Norton, C. L.; O'Sullivan, N.; Stephens, M. A.; Stradiotto, N. R.; Swann, E.; Stratford, I. J. Cyclopropamitosenes, novel bioreductive anticancer agents. Synthesis, electrochemistry, and biological activity of 7-substituted cyclopropamitosenes and related indolequinones. *J. Med. Chem.* **1994**, *37*, 3834–3843.
- (49) Beall, H. D.; Winski, S.; Swann, E.; Hudnott, A. R.; Cotterill, A. S.; O'Sullivan, N.; Green, S. J.; Bien, R.; Siegel, D.; Ross, D.; Moody, C. J. Indolequinone antitumor agents: Correlation between quinone structure, rate of metabolism by recombinant human NAD(P)H: quinone oxidoreductase, and in vitro cytotoxicity. *J. Med. Chem.* **1998**, *41*, 4755–4766.
- (50) Swann, E.; Barraja, P.; Oberlander, A. M.; Gardipee, W. T.; Hudnott, A. R.; Beall, H. D.; Moody, C. J. Indolequinone antitumor agents: Correlation between quinone structure and rate of metabolism by recombinant human NAD(P)H: quinone oxidoreductase. Part 2. *J. Med. Chem.* **2001**, *44*, 3311–3319.
- (51) Fryatt, T.; Pettersson, H. I.; Gardipee, W. T.; Bray, K. C.; Green, S. J.; Slawin, A. M.; Beall, H. D.; Moody, C. J. Novel quinoline-quinone antitumor agents: Structure-metabolism studies with NAD(P)H: quinone oxidoreductase (NQO1). *Bioorg. Med. Chem.* **2004**, *12*, 1667–1687.
- (52) Phillips, R. M.; Naylor, M. A.; Jaffar, M.; Doughty, S. W.; Everett, S. A.; Breen, A. G.; Choudry, G. A.; Stratford, I. J. Bioreductive activation of a series of indolequinones by human DT-diaphorase: Structure-activity relationships. *J. Med. Chem.* **1999**, *42*, 4071–4080.
- (53) Winski, S. L.; Hargreaves, R. H.; Butler, J.; Ross, D. A new screening system for NAD(P)H:quinone oxidoreductase (NQO1)-directed antitumor quinones: Identification of a new aziridinyl-hfbenzoquinone, RH1, as a NQO1-directed antitumor agent. *Clin. Cancer Res.* **1998**, *4*, 3083–3088.

- (54) Phillips, R. M.; Jaffar, M.; Maitland, D. J.; Loadman, P. M.; Shnyder, S. D.; Steans, G.; Cooper, P. A.; Race, A.; Patterson, A. V.; Stratford, I. J. Pharmacological and biological evaluation of a series of substituted 1,4-naphthoquinone bioreductive drugs. *Biochem. Pharmacol.* **2004**, *68*, 2107–2116.
- (55) Suleman, A.; Skibo, E. B. A comprehensive study of the active site residues of DT-diaphorase: Rational design of benzimidazole derivatives as DT-diaphorase substrates. *J. Med. Chem.* **2002**, *45*, 1211–1220.
- (56) Hendriks, H. R.; Pizao, P. E.; Berger, D. P.; Kooistra, K. L.; Bibby, M. C.; Boven, E.; Dreef-van der Meulen, H. C.; Henrar, R. E. C.; Fiebig, H. H.; Double, J. A.; Hornstra, H. W.; Pinedo, H. M.; Workman, P.; Schwartzmann, G. EO9: A novel bioreductive alkylating indoloquinone with preferential solid tumour activity and lack of bone marrow toxicity in preclinical models. *Eur. J. Cancer* **1993**, *29A*, 897–906.
- (57) Abe, N.; Nakakita, Y.; Nakamura, T.; Enoki, N.; Uchida, H.; Takeo, S.; Munekata, M. Novel cytotoxic compounds, oxopropalines from *Streptomyces* sp. G324 producing lavendamycin. I. Taxonomy of the producing organism, fermentation, isolation and biological activities. *J. Antibiot. (Tokyo)* **1993**, *46*, 1672–1677.
- (58) SYBYL molecular modeling software; SYBYL 6.9.1 ed.; Tripos Inc.: St. Louis, MO.
- (59) Lemmen, C.; Lengauer, T. Time-efficient flexible superposition of medium-sized molecules. *J. Comput.-Aided Mol. Des.* **1997**, *11*, 357–368.
- (60) Rarey, M.; Kramer, B.; Lengauer, T.; Klebe, G. A fast flexible docking method using an incremental construction algorithm. *J. Mol. Biol.* **1996**, *261*, 470–489.
- (61) Eldridge, M. D.; Murray, C. W.; Auton, T. R.; Paolini, G. V.; Mee, R. P. Empirical scoring functions: I. The development of a fast empirical scoring function to estimate the binding affinity of ligands in receptor complexes. *J. Comput.-Aided Mol. Des.* **1997**, *11*, 425–445.
- (62) Kuntz, I. D.; Blaney, J. M.; Oatley, S. J.; Langridge, R.; Ferrin, T. E. A geometric approach to macromolecule-ligand interactions. *J. Mol. Biol.* **1982**, *161*, 269–288.
- (63) Jones, G.; Willett, P.; Glen, R. C.; Leach, A. R.; Taylor, R. Development and validation of a genetic algorithm for flexible docking. *J. Mol. Biol.* **1997**, *267*, 727–748.
- (64) Muegge, I.; Martin, Y. C. A general and fast scoring function for protein–ligand interactions: A simplified potential approach. *J. Med. Chem.* **1999**, *42*, 791–804.
- (65) Allen, C. F. H.; Spangler, F. W.; Webster, E. R. Ethylenimine. *Org. Synth.* **1963**, *Coll. Vol. IV*, 433–435.
- (66) DeLano, W. L. *The PyMOL molecular graphics system*; PyMOLX11Hybrid ed.; DeLano Scientific: San Carlos, CA.

JM050758Z

Introduction: Unexpected behavior arising from the quaternary structure of glutamate transporters.

G.P. Leary, D.C. Holley, E.F. Stone, B.R. Lyda, C.S. Esslinger, L.V. Kalachev, and M.P. Kavanaugh

β -2-fluorenyl-aspartylamide (2-FAA) is an aspartate analogue and a recently described competitive inhibitor of the EAATs with selectivity for EAAT3 (Bridges et al., 2008). In this manuscript we show that the subtype selectivity is derived not from binding affinity but instead from a slower dissociation rate. We used EAAT3 homology models based on the 3-bromo-DL-*threo*- β -benzyloxyaspartate (3-Br-TBOA)-bound Glt_{Ph} crystal structure (Boudker et al., 2007) as a scaffold for computational docking of 2-FAA to determine a mechanism for the dissociation rate. Our docking study shows that high-ranked docked poses of 2-FAA interact with a conserved hydrophobic pocket in EAAT3 (figure 1). Though 2-FAA is structurally similar to 3-Br-TBOA (figure B), the docking profile presented in this manuscript suggests an alternative to the binding orientation presented in the 3-Br-TBOA-bound crystal structure. Specifically, our results show two possible orientations for 2-FAA with higher ranking poses assuming an ‘upward’ orientation with 2-FAA’s fluorene head group interacting with the conserved hydrophobic pocket in EAAT3 and lower ranking poses oriented in a ‘downward’ pose more similar to that of 3-Br-TBOA in the Glt_{Ph} crystal structure (figure 1b, for simplification 3-Br-TBOA is depicted as TBOA in figure 1b).

	<u>ChemScore</u>	<u>ΔG</u>	<u>orientation</u>
2-FAA	22.39	-29.88	up
2-FAA	18.94	-24.23	down
TBOA	18.07	-22.14	up
TBOA	-	-	down
3-Br-TBOA	20.19	-23.09	up
3-Br-TBOA	18.04	-23.90	down

Table a. Docking of 2-FAA, TBOA, and 3-Br-TBOA into an EAAT3 homology model show two possible binding orientations.

Though not included in this manuscript, we also found that DL-*threo*- β -benzyloxyaspartate (TBOA, a competitive inhibitor from which 3-Br-TBOA was derived) assumed only upward orientations. Conversely, docked poses of 3-Br-TBOA ranked slightly higher in the downward orientation (table A), suggesting that the 3-Br-TBOA-bound Glt_{Ph}

crystal structure could be inadequate as a comprehensive model for structure-based inhibitor design.

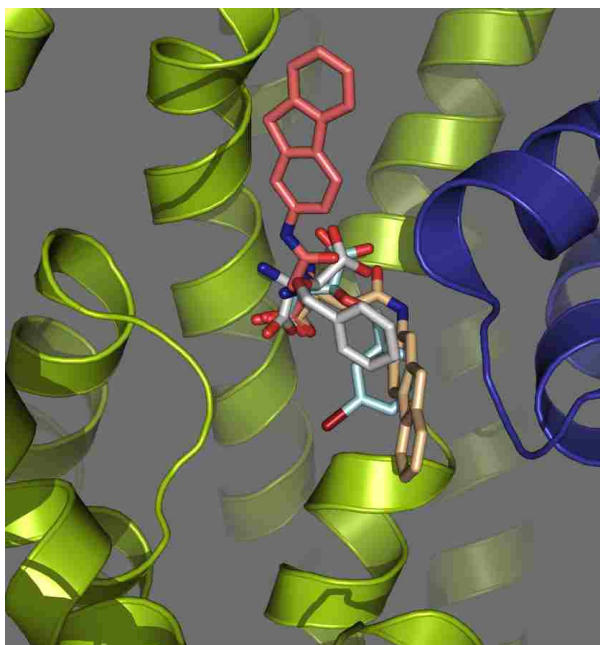


Figure b. Stick representations of inhibitors docked into an EAAT3 homology model. 2-FAA poised in the 'upward' orientation is colored salmon while the 'downward' oriented pose is colored wheat. 3-Br-TBOA is colored light blue and shown only in the downward orientation. TBOA (light grey) from the Glt_{Ph} crystal structure (2NWX) was imported as a reference.

For brevity and simplicity, I have included only the portions of the manuscript that specifically relate to my research.

References

- Boudker O, Ryan RM, Yernool D, Shimamoto K, Gouaux E (2007) Coupling substrate and ion binding to extracellular gate of a sodium-dependent aspartate transporter. *Nature* 445:387-393.
- Bridges RJ, Rhoderick J, Barany A, Lyda B, Ye R, Esslinger CS and Gerdes J (2008) Selective inhibition of the excitatory amino acid transporter EAAT3 by 7-halo- fluorenyl- aspartylamides., in Society for Neuroscience's 38th annual meeting, Washington D. C.

Unexpected behavior arising from the quaternary structure of glutamate transporters

G.P. Leary¹, D.C. Holley¹, E.F. Stone², B.R. Lyda¹, C.S. Esslinger¹, L.V. Kalachev², and M.P. Kavanaugh^{1*}

Center for Structural and Functional Neuroscience, Departments of ¹Biomedical and Pharmaceutical Sciences and ²Mathematics, University of Montana, Missoula, MT;

Abstract

β -2-fluorenyl-aspartylamide (2-FAA) is a structurally novel inhibitor of excitatory amino acid transporters (EAATs) that exhibits nanomolar potencies for blocking glutamate uptake and approximately ten-fold selectivity for the neuronal transporter EAAT3. We recorded currents in voltage-clamped *Xenopus* oocytes expressing human EAATs and used concentration jumps to measure binding and unbinding rates of 2-FAA in the presence or absence of glutamate by monitoring steady state glutamate transport currents or pre-steady state Na⁺-dependent charge movements, respectively. The binding rates of the drug were not significantly different for EAAT1, EAAT2, or EAAT3 but were approximately one order of magnitude slower than that of glutamate. The selectivity of 2-FAA for EAAT3 resulted from an approximately ten-fold slower dissociation rate of the drug. Unexpectedly, the rate of recovery from block in the absence of glutamate was about 8 times slower than the rate measured in the presence of saturating glutamate. This result is inconsistent with pseudo first-order unbinding kinetics previously assumed for glutamate transporter block and suggests a significant probability of drug rebinding in neighboring subunits. In agreement with this, co-expressing wild-type subunits with an excess of mutant subunits (R447C) that do not bind glutamate or drug increased the unblocking rate similar to the effects of glutamate. We propose a model in which electrostatic and steric factors arising from the EAAT quaternary structure restrict diffusion near the three ligand binding sites, resulting in an apparent dissociation rate that is significantly slower than the true first-order subunit unbinding rate. Fitting this model to the 2-FAA block data reveals the quaternary structure increases the probability, by a factor of three, that a molecule will bind to the transporter opposed to being lost to diffusion.

Introduction

The human excitatory amino acid transporters (EAAT1-5) are secondary active transporters that terminate excitatory synaptic transmission within the central nervous system by removing glutamate from the extracellular space. EAATs move glutamate across the membrane against its concentration gradient by stoichiometrically coupling transport to the sodium, potassium, and proton electrochemical gradients, with cotransport of 3Na⁺, 1H⁺, and 1 glutamate and countertransport of 1 K⁺ (Levy et al., 1998; Zerangue and Kavanaugh, 1996). A crystal structure for a homologous archaeal transporter from *Pyrococcus horikoshii* revealed the transporter to be a homotrimer with individual binding sites located within each subunit. Individual glutamate transporter subunits in a trimer function independently, both in terms

glutamate flux and an ancillary chloride conductance (Grewer et al., 2005; Koch et al., 2007; Leary et al., 2007). This has led to a teleological question concerning the reason for a trimeric structure. One notable feature integral to the trimer structure is the central cavity or bowl formed by the junction of the three wedged-shaped subunits. Because the surface of this water-filled cavity is predominately hydrophilic and it dips far into the plane of the membrane, one possibility is that it serves to lower the energy barrier for glutamate and co-transported ions to cross the membrane (Gouaux and Mackinnon, 2005). Further clues about the mechanistic role of the quaternary structure have come from the recent structural determination of the inward-facing form of Glt_{Ph} , which reveals that relatively static inter-subunit contacts may be involved in facilitating the relative motion of the central core of each subunit to deliver the binding site to the internal face while the outer helices remain relatively fixed (Reyes et al., 2009).

Several years ago a structurally novel aspartic acid amide, β -2-fluorenyl-aspartylamide ((S)-4-(9H-fluoren-2-ylamino)-2-amino-4-oxobutanoic acid; 2-FAA) was reported to be a glutamate transporter blocker (IC_{50} 25-90 nM) with ten-fold selectivity for EAAT3 over EAAT1 and EAAT2 (Bridges et al., 2008). The molecule is an aspartamide with a fluorenyl ring extended from the amino group of the side chain (figure 1b).

Measuring microscopic rate constants of glutamate transporters has been technically challenging due to the requirements for use of techniques involving glutamate photo-uncaging or piezo-element driven fast application of glutamate or inhibitors to membrane patches containing transporters (Wadiche and Kavanaugh, 1998; Otis and Kavanaugh, 2000). In this work we take advantage of the high affinity of 2-FAA for glutamate transporters to use a slightly modified two-microelectrode voltage clamp chamber in which we can apply concentration jumps to oocytes in conditions where measurement of drug kinetics are not limited by solution exchange times. We conclude that 2-FAA is selective for EAAT3 solely because of a slower unbinding rate compared to EAAT2 and EAAT1. Further, we provide evidence that the effective macroscopic rate of recovery from drug block is up to eight-fold slower than the unbinding rate from an individual subunit, and we propose that the quaternary structure of the transporter plays a previously unknown role in restricting diffusion and enhancing the efficiency of ligand capture by the transporter.

Experimental Methods

Computational modeling. Human EAAT3 sequence (obtained from GenBank, <http://www.ncbi.nlm.nih.gov>) was aligned with the Protein Data Bank (PDB) sequences for an archaeal homologue (Glt_{Ph}, 2NWW.pdb) according to Yernool, et al. (Boudker et al., 2007, Yernool et al., 2004). The EAAT3 homology model was constructed by threading the aligned sequence along 2NWW coordinates using the SwissProt server (<http://swissmodel.expasy.org/SWISS-MODEL.html>). The resulting model was optimized through local energy minimizations of regions with high steric and electrostatic interference using the AMBER7 force field in the Tripos SYBYL8.0 platform. Representations of 2-FAA, and TBOA were docked using GOLD v. 3.0.1 (<http://www.ccdc.cam.ac.uk/>) into the EAAT3 model and evaluated using the ChemScore scoring function. Each of the top thirty poses for each of three separate docking runs were evaluated for their capacity to hydrogen bond with EAAT3 R447 and D444 residues. ΔG values were extracted from ChemScore output to quantify relative K_d values. Poses with the lowest estimated ΔG values determined by ChemScore were incorporated into the homology model and visualized using PyMol1.0

Results

Computational docking of 2-FAA to EAAT3

We docked 2FAA into EAAT3 homology models using the GOLD docking program to determine possible mechanisms responsible for 2-FAA's nanomolar affinity. Our results indicate structural positioning of the inhibitors that differ from the pose of TBOA in the 2NWW Glt_{Ph} crystal structure (Boudker et al., 2007). Specifically, the highest ranking docked poses position 2-FAA's fluorene head group with a grouping of non-polar residues in TM7, TM8 and the HP2 loop (figure 1A, 1B), while the benzene ring of the crystal structure TBOA is oriented toward the solvent accessible tip of the HP2 loop (figure 1b). We found only lower-ranking poses of 2-FAA adopt orientations similar to TBOA in the Glt_{Ph} crystal structure with binding affinities approximately one order of magnitude lower than the higher ranked poses described above (the ranked score determined by ChemScore of the highest ranked pose shown in figure 1B is 22.4 with a ΔG of -29.9 and a K_d of 5.8 μ M while the lower ranked poses score 18.9 with a ΔG of -24.2 and a K_d of 57 μ M).

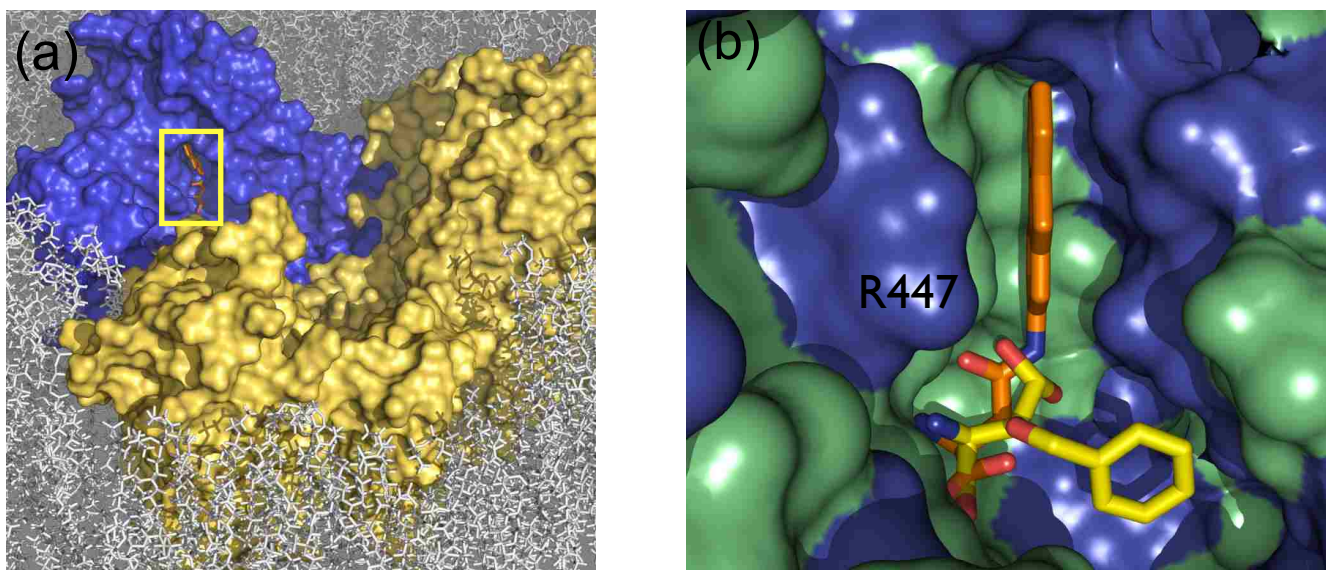


Figure 1: a. A surface rendering of a EAAT3 homology model threaded through GlTph (2NWW.pdb) using the SWISS-MODEL homology modeling server. 2-FAA is oriented in the binding site based on computational docking experiments using the GOLD docking program (v.3.0.1) with the ChemScore scoring function. The structure was visualized using PyMol version 1.0. b. The EAAT3 docking study revealed an alternative binding pocket from that of TBOA in the 2NWW GIT_{Ph} crystal structure. The fluorene group of docked 2-FAA (orange) is shown interacting with polar (green) and non-polar (dark-blue) residues in TM7, TM8 and in the HP2 loop. TBOA (yellow) determined in the GIT_{Ph} crystal structure overlays docked 2-FAA to show the alternative orientation described by Boudker et al., 2007.

	ChemScore	ΔG	Kd(μM)	orientation
2-FAA	22.39	-29.88	5.8	up
2-FAA	18.94	-24.23	57	down

Table 1. ChemScore evaluation of 2-FAA docked poses shows an increased affinity of EAAT3 homology model for the 'upward' orientation.

Discussion

Experimentally, the K_i for an inhibitor is most commonly estimated using the Schild Analysis or derivation from the IC_{50} using the Cheng-Prusoff equation. Our attempts at a Schild analysis for 2-FAA were unsuccessful and inaccurate due to experimental challenges associated with long and repeated drug application. The Cheng-Prusoff conversion of the IC_{50} from the steady state currents gave comparable estimates of the K_i ; however, with this method, it is critical to take into account the time for the drug to reach a steady state block. For a potent drug like 2-FAA, not being at steady state in a 5 min radiolabeled uptake experiment would result in a drastic underestimate of the IC_{50} and thus K_i . Because of the high affinity/slow off-rate of the 2-FAA, it was possible to study its microscopic kinetics with high resolution in oocytes expressing EAATs using a moderately fast-flow chamber designed for this

purpose. Blocking and unblocking rates measured using varying concentrations of 2-FAA at EAAT1-3 are consistent with the differences in measured affinities for EAAT1-3. This technique offered us the advantage of distinguishing the binding event from the unbinding, suggesting that unbinding from EAAT3 was 7-8-fold slower than EAAT1 or 2, accounting solely for the difference in K_i .

Computational docking studies with 2-FAA are also in agreement with a significantly increased affinity relative to TBOA as well as a different binding orientation than determined for TBOA though x-ray crystallography (Boudker et al., 2007). This new orientation of the molecule falls in a hydrophobic pocket of the binding site which helps to explain why there is a general increase in potency of molecules for all EAATs with an increase in the lipophilic nature of the side chain. This agrees with current research that shows no affinity change for TBOA in EAATs expressing mutations of a methionine described by Boudker et al (2007) as interacting with the benzyl ring of TBOA (Rosental & Kanner, 2010). Though we could not use the Schild analysis to determine if 2-FAA was a competitive inhibitor, this unique but local docking of 2-FAA within the known binding site supports the interpretation of it as a competitive inhibitor, as well as the fact that saturating concentrations of glutamate could still recover the I_{max} following block by 2-FAA, if performed within the same hour.

References

- Bendahan A, Armon A, Madani N, Kavanaugh MP, Kanner BI (2000) Arginine 447 plays a pivotal role in substrate interactions in a neuronal glutamate transporter. *J of Biological Chemistry* 275(48):37436-37442.
- Benveniste M, Mienville JM, Sernagor E and Mayer ML (1990) Concentration-jump experiments with NMDA antagonists in mouse cultured hippocampal neurons. *J Neurophysiol* 63(6):1373-1384.
- Bergles DE, Tzingounis AV and Jahr CE (2002) Comparison of coupled and uncoupled currents during glutamate uptake by GLT-1 transporters. *J Neurosci* 22(23):10153-10162.
- Boudker O, Ryan RM, Yernool D, Shimamoto K, and Gouaux E (2008) Coupling substrate and ion binding to extracellular gate of a sodium-dependent aspartate transporter. *Nature* 445(7126):387-93.
- Bridges RJ, Kavanaugh MP and Chamberlin AR (1999) A pharmacological review of competitive inhibitors and substrates of high-affinity, sodium-dependent glutamate transport in the central nervous system. *Curr Pharm Des* 5(5):363-379.
- Bridges RJ, Rhoderick J, Barany A, Lyda B, Ye R, Esslinger CS and Gerdes J (2008) Selective inhibition of the excitatory amino acid transporter EAAT3 by 7-halo- fluorenyl-aspartylamides., in Society for Neuroscience's 38th annual meeting, Washington D. C.

- Diamond JS and Jahr CE (1997) Transporters buffer synaptically released glutamate on a submillisecond time scale. *J Neurosci* 17(12):4672-4687.
- Dunlop J (2006) Glutamate-based therapeutic approaches: targeting the glutamate transport system. *Curr Opin Pharmacol* 6(1):103-107.
- Dunlop J and Butera JA (2006) Ligands targeting the excitatory amino acid transporters (EAATs). *Curr Top Med Chem* 6(17):1897-1906.
- Gouaux E and Mackinnon R (2005) Principles of selective ion transport in channels and pumps. *Science* 310(5753):1461-1465.
- Grewer C, Balani P, Weidenfeller C, Bartusel T, Tao Z and Rauen T (2005) Individual subunits of the glutamate transporter EAAC1 homotrimer function independently of each other. *Biochemistry* 44(35):11913-11923.
- Jones MV, Sahara Y, Dzuby JA and Westbrook GL (1998) Defining affinity with the GABAA receptor. *J Neurosci* 18(21):8590-8604.
- Kavanaugh MP (2004) Accessing a transporter structure. *Nature* 431(7010):752-753.
- Koch HP, Brown RL, and Larsson HP (2007) The Glutamate-activated anion conductance in excitatory amino acid transporters is gated independently by the individual subunits. *J Neurosci* 27(11):2943-2947.
- Larsson HP, Tzingounis AV, Koch HP and Kavanaugh MP (2004) Fluorometric measurements of conformational changes in glutamate transporters. *Proc Natl Acad Sci U S A* 101(11):3951-3956.
- Leary GP, Stone EF, Holley DC and Kavanaugh MP (2007) The glutamate and chloride permeation pathways are colocalized in individual neuronal glutamate transporter subunits. *J Neurosci* 27(11):2938-2942.
- Levy LM, Warr O and Attwell D (1998) Stoichiometry of the glial glutamate transporter GLT-1 expressed inducibly in a Chinese hamster ovary cell line selected for low endogenous Na⁺-dependent glutamate uptake. *J Neurosci* 18(23):9620-9628.
- Mayer ML, Westbrook GL and Vyklicky L, Jr. (1988) Sites of antagonist action on N-methyl-D-aspartic acid receptors studied using fluctuation analysis and a rapid perfusion technique. *J Neurophysiol* 60(2):645-663.
- Otis TS and Kavanaugh MP (2000) Isolation of current components and partial reaction cycles in the glial glutamate transporter EAAT2. *J Neurosci* 20(8):2749-2757.
- Vasil'eva, Butuzov, and Kalachev, *The Boundary Function Method for Singular Perturbation Problems*, SIAM, Philadelphia, 1995.
- Wadiche JI, Arriza JL, Amara SG and Kavanaugh MP (1995) Kinetics of a human glutamate transporter. *Neuron* 14(5):1019-1027.
- Wadiche JI and Kavanaugh MP (1998) Macroscopic and microscopic properties of a cloned glutamate transporter/chloride channel. *J Neurosci* 18(19):7650-7661.
- Watzke N, Bamberg E and Grewer C (2001) Early intermediates in the transport cycle of the neuronal excitatory amino acid carrier EAAC1. *J Gen Physiol* 117(6):547-562.
- Yernool D, Boudker O, Jin Y and Gouaux E (2004) Structure of a glutamate transporter homologue from *Pyrococcus horikoshii*. *Nature* 431(7010):811-818.
- Zerangue N and Kavanaugh MP (1996) Flux coupling in a neuronal glutamate transporter. *Nature* 383(6601):634-637.

Chapter 5: Discussion and future directions

The multiple published crystal structures of the Gl_{TPh} archaeal EAAT homologue have provided abundant opportunity to supplement, augment, and contextualize decades of research into EAAT structure and function. Much of the work presented here focused on cation and substrate interactions with EAAT3, ultimately resulting in development of an incomplete but consistent model for sequential binding and unbinding of cations and glutamate during transport (chapter 3, figure 11). Specifically, we describe previously uncharacterized Na⁺ and K⁺ coordination sites and attempted to deconstruct the sequence of events that lead to transport of sodium and glutamate and subsequent countertransport of K⁺. Our research, however, is merely the start of possible computational work that could lead to truly unraveling the mechanisms behind EAAT transport. In the following paragraphs I will explore two methods for future computational experiments that would potentially expand our initial findings.

B-factors

Most crystal structures are published with isotropic (non-directional) temperature factors, or B-factors. B-factors are a measure of how much an atom vibrates around the coordinates of the atom specified in an X-ray crystal structure and relate to the resolution of each atom in a structure by the equation

$$B = 8\pi^2 * u^2$$

where u is the root mean square deviation from an atom's position (Mair and Wilkins, 1975). Thus, under ideal conditions B-factors suggest mobility of an atom relative to other atoms within the same structure (elements that can confound interpretation of movement using B-factors include localized artifacts such as unit cell packing constraints and the symmetry of unit cells [Carugo and Argos, 1997; Rapp and Pollack, 2005]). A mean B-factor for high-resolution structures is usually around 60\AA^2 which indicates that the resolution of an average atom is smeared around a radius of 0.87\AA s.

The Gl_{TPh} structures are of moderate resolutions, ranging from approximately 3.2\AA s to 3.5\AA s and two of the published structures are sufficiently resolved to reveal TI⁺ and Na⁺ densities. The mean B-factor for the inward facing structure and highest resolved outward-facing structure (3KBC.pdb and 2NWX.pdb respectively) are both approximately 100\AA^2 ranging from more stable atoms with B-factors of approximately 94\AA^2 to atoms with more

thermal activity with B-factors of approximately 106\AA^2 (Boudker et al., 2007; Reyes et al., 2009). Figure 1 depicts single trimer subunits colored to show B-factors for the protein backbone of the outward-facing, thallium- and aspartate-bound structure (figure 1a) and the inward-facing, sodium- and aspartate-bound structure (figure 1b). The variable thickness of the cartoon in figure 1 was calculated from B-factors using the above equation to show the root mean square deviation of protein backbone atoms. The cartoon thickness therefore approximates the range of movement of the protein backbone, showing limited vibrational variation throughout the protein. Relative B-factor variations, though, can be informative and suggest regions with higher mobility. The C-terminal region of HP2 in the inward facing structure (indicated by the arrow in figure 1b), for example, is an area with higher B-factors, suggesting potential mobility, which, due to its proximity to the substrate binding site could indicate involvement in substrate and cation release. A statistical analysis of regions with high B-factors that correlate to regions showing electrostatic potential could be informative.

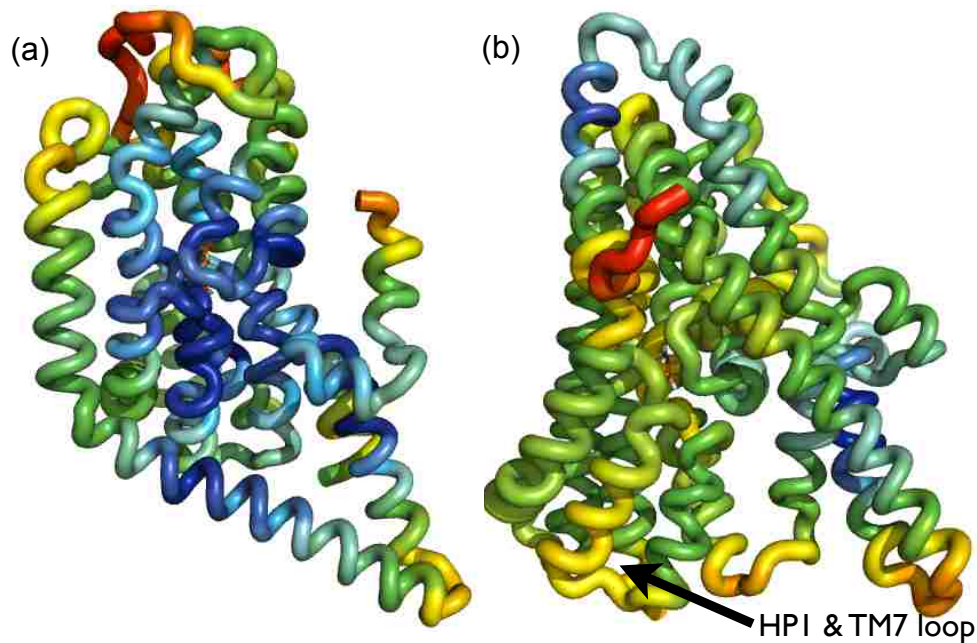


Figure 1. Cartoon depictions of outward-facing (a) and inward-facing (b) Glt_{PH} subunits colored by B-factors, with regions of higher B-factors colored more red and regions with lower B-factors colored blue. Thickness of the cartoon was calculated to depict possible range of movement. The arrow indicates a possible region of interest showing higher B-factors near the amino acid binding site.

Coarse-grain molecular dynamics

Glutamate transport is a fairly rapid process taking only milliseconds to complete each transport cycle (Grewer et al., 2000). Though physiologically rapid, this timeframe poses a problem for molecular dynamics simulations. Currently, using a system that approximates close-range interactions of each atom through force fields derived from classical molecular mechanics (i.e. assuming Newtonian interactions prevail in a system allowing for the exclusion of computationally expensive quantum calculations), only very short simulations are possible. For example, we are using graphical processing units to accelerate our molecular dynamics simulations. Even with accelerated processing, we can only achieve two nanoseconds of simulation per day for systems with 120,000 explicit atoms. This of course prohibits micro-, let alone millisecond timeframes (at two nanoseconds per day we would require 5500 years for a one millisecond simulation). One possible method that would alleviate some of the more computationally expensive calculations is coarse-grain molecular dynamics. As the name suggests, the resolution of certain atomic interactions would be reduced. Explicit representations of atoms within methylene groups in lipid bi-layers, for example, could be united to pseudo-atom approximations. In our system with nearly 400 lipid molecules, we would enjoy approximately 1/3 fewer calculations per time-step without sacrificing accurate involvements relevant to transport.

Concluding remarks

The continued development of databases in genomics, proteomics, protein structure, systems biology, and epidemiology has yielded unprecedented amounts of information. The ability to manipulate or to otherwise interpret or reinterpret data to find trends, create predictive models, or simulate systems will become increasingly valuable as databases expand. While investigations into EAAT structure and function constituted the bulk of this dissertation, the greater goal was to begin interpreting the functional implications hidden within protein structures using computational biology. Peace out.

References

- Boudker O, Ryan RM, Yernool D, Shimamoto K, Gouaux E (2007) Coupling substrate and ion binding to extracellular gate of a sodium-dependent aspartate transporter. *Nature* 445:387-393.
- Carugo O, Argos P (1997) Protein-protein crystal-packing contacts. *Protein Sci* 6:2261-2263.
- Grewer C, Watzke N, Wiessner M, Rauen T (2000) Glutamate translocation of the neuronal glutamate transporter EAAC1 occurs within milliseconds. *Proceedings of the National Academy of Sciences of the United States of America* 97:9706-9711.
- Mair S, Wilkins S (1976) Anharmonic Debye-Waller factors using quantum statistics. *J. Phys. C: Solid State Phys.* 9:1145-1158.
- Rapp CS, Pollack RM (2005) Crystal packing effects on protein loops. *Proteins* 60:103-109.
- Reyes N, Ginter C, Boudker O (2009) Transport mechanism of a bacterial homologue of glutamate transporters. *Nature* 462:880-885.